Nuclear structure studies of odd-odd and odd-A nuclei in the shape transition region around N = 60

Inaugural-Dissertation
zur
Erlangung des Doktorgrades
der Mathematisch-Naturwissenschaftlichen Fakultät
der Universität zu Köln

vorgelegt von
Matthias Rudigier
aus Titisee-Neustadt
Köln 2013

Gutachter: Prof. Dr. Jan Jolie
Prof. Dr. Peter Reiter

Tag der mündlichen Prüfung: 16.01.2014

Zusammenfassung

Die Lebensdauer angeregter Kernzustände ist eine wichtige Observable in der Kernstrukturphysik. Sie liefert Informationen über die zugrundeliegende Struktur der angeregten Zustände und ist in Kombination mit Zerfallsverzweigungsverhältnissen und Multipolmischungsverhältnissen eine notwendige Information, um Übergangsmatrixelemente zu bestimmen. Letztere erlauben Rückschlüsse auf die Wellenfunktionen des Sytems und ihre Vorhersage ist ein essentieller Test für Kernstrukturmodelle.

Isomere Zustände zeichnen sich durch eine außergewöhnlich lange Lebensdauer aus, die eine Folge ihrer Kernstruktur ist. Die Untersuchung von Isomeren und ihrem Zerfall liefert einen wichtigen Beitrag zu einem tieferen Verständnis der mikroskopischen Strukturen innerhalb einer Massenregion.

Die Messung von Lebensdauern in exotischen Kernen stellt eine große experimentelle Herausforderung dar. Dieser wird durch aktuelle Entwicklungen in der Anwendung von inverser Coulomb-Anregung und Plunger-Messungen mit radioaktiven Strahlen begegnet. Eine weitere Methode, anwendbar für Lebensdauern bis hinab zu 5 ps, ist die Verzögerte Koinzidenz-Methode mit sehr schnellen LaBr$_3$(Ce)-Detektoren. Diese Technik wurde in dieser Arbeit zum ersten Mal angewendet um Lebensdauern in sehr neutronenreichen Kernen zu bestimmen.

Die durchgeführten Experimente an neutronenreichen Kernen mit Neutronenanzahl N=60 und deren Ergebnisse werden diskutiert. Ein neues μs-Isomer mit einem 76.5 keV E1-Zerfall wurde eindeutig dem N=60-Kern ^{97}Rb zugeordnet. Ein neuer Zerfallszweig des deformierten $K = 9/2^+$ [404] Isomers in ^{97}Sr wird vorgestellt. Lebensdauermessungen von Rotationszuständen in ^{99}Y und von Zuständen mit bislang ungewisser Struktur in ^{100}Nb wurden erfolgreich durchgeführt. Lebensdauermessungen im β-Untergrund bestätigen frühere gemessene Werte. Diese Experimente unter Anwendung der Verzögerten Koinzidenz-Methode demonstrieren überzeugend die Machbarkeit von Präzisions-$\gamma - \gamma$-Fast-Timing-Messungen von angeregten Zuständen in exotischen Kernen, die ein niedriges Signal-zu-Untergrund-Verhältnis und einen ausgedehnten Strahlfleck mit sich bringen. Messergebnisse einer umfassenden Isomer-Spektroskopie-Kampagne am Lohengrin-Massenseparator am Institut Laue-Langevin, Grenoble, werden vorgestellt. Diese Messungen lieferten präzisere Lebensdauern von μs-Isomeren in leichten Spaltungsfragmenten. Des Weiteren war es möglich, Isomerbevölkerungsverhältnisse für viele der beobachteten Isomere zu bestimmen. Diese Ergebnisse sind wertvolle Vergleichsdaten für Modellvorhersagen und essentielle Informationen für das Verständnis des komplexen Spaltungsprozesses. Abschließend werden die experimentellen Ergebnisse diskutiert und mit Vorhersagen aus Kernmodellrechnungen verglichen. Dem neu entdeckten Zustand mit dem 76.5 keV Zerfall in ^{97}Rb konnte ein Spin von $(1/2, 3/2, 5/2)^-$ zugeordnet werden. Der Vergleich zu Rechnungen von Simpson und Daugas weist auf einen möglichen oblaten Charakter dieses tiefliegenden isomeren Zustands hin. Der neue Zerfallszweig, der in ^{97}Sr beobachtet wurde, führt zu der Identifikation des 522 keV Zustands als ersten angeregten $5/2^+$ Zustand. Rech-

nungen innerhalb des IBFM deuten auf einen Ein-Quasi-Teilchen-Charakter dieser Anregung. Mit der Lebensdauermessung in ^{99}Y ist ein weiteres Anzeichen für die reguläre Rotationsstruktur der Grundzustandsbande gewonnen. Eine Rechnung mittels des Quasi-Teilchen-Rotor-Modells mit der Annahme einer axial-symmetrischen Deformation zeigen gute Übereinstimmung für die Grundzustandsbande in diesem Isotop. Die Lebensdauermessungen für die Zerfallskaskade des μs-Isomers in ^{100}Nb deuten auf den nicht-kollektiven Charakter dieser Anregung hin.

Abstract

Lifetimes of nuclear excited states are a very important observable in nuclear physics. They deliver information on the structure of excited states, and, in combination with branching ratios and multipole mixing ratios, are necessary to deduce transition matrix elements. These are directly linked to the wave functions of the system and their prediction poses an important test for nuclear structure models. Isomers are a special kind of excited state. Their unusually long lifetime is an embodiment of their unique structure. A study of isomers and their decay often yields a better understanding of evolution of the microscopic structure within a mass region.

The measurement of lifetimes in exotic nuclei poses a great experimental challenge. This challenge is met by the recent developments in application of inverse Coulomb excitation and Plunger measurements with radioactive ion beams. Another method which is applicable for the measurement of lifetimes down to 5 ps is the delayed coincidence method with very fast $LaBr_3(Ce)$ detectors. This technique was successfully applied in combination with a fission fragment separator for the first time in this work to measure lifetimes in very neutron-rich nuclei.

Experiments on neutron-rich nuclei with neutron number N = 59 and N = 60, performed within the scope of this thesis, are discussed and the results are presented. A new μs isomer with a 76.5 keV E1 decay transition was unambiguously assigned to the N = 60 nucleus ^{97}Rb. Data on a new decay branch of the K=9/2+[404] deformed isomer in ^{97}Sr are presented. Lifetime measurements of rotational states in ^{99}Y and states with previously unknown structure in ^{100}Nb were performed successfully. Lifetime measurements in the β background reproduced literature values. These experiments, employing the delayed coincidence technique, convincingly demonstrate the feasibility of precision $\gamma\ \gamma$ fast timing measurements of excited states in exotic nuclei, which involve low peak-to-background ratio and an extended beam spot.

The data of a large isomer spectroscopy campaign at Lohengrin at the Institute Laue-Langevin, Grenoble, are presented. These measurements yielded more precise μs isomer lifetimes in light fission fragments. Furthermore, it was possible to deduce isomer population ratios for many of the observed isomers. These results are important data for comparison with model predictions of mean spin population after fission, and essential information for understanding the very complex fission process.

Finally, the experimental results are discussed and compared to nuclear model calculations. For ^{97}Rb a spin assignment of (1/2, 3/2, 5/2)- can be made for the state with the 76.5 keV transition. Comparison to calculations, made by Simpson and Daugas, shows hints at a possible oblate character of the low-lying isomeric state. The new decay branch in ^{97}Sr allows a spin assignment of $5/2^+$ to the state at 522 keV. Calculations within the IBFM indicate a simple one-quasi-particle structure of this state. The lifetime measurements in ^{99}Y give further evidence for the regular rotational structure of the ground-state band in this nucleus. A calculation applying the quasi particle rotor model, assuming axially symmetric deformation, yields good agreement for the

ground-state band. The lifetime measurements in the decay cascade of the μs isomer in ^{100}Nb clearly indicate non-collective nature of these excitations.

Contents

Introduction

The nuclei in the shape transition region at neutron number N = 60 have been a focus of nuclear structure studies for many years. With new and improved experimental techniques the neutron-rich nuclei in this region, with proton numbers below Z = 40, became more accessible, enabling a study of the influence of occupation of the proton orbitals on the shell structure of this region. In this thesis, new data on four nuclei in this mass region are presented. The very exotic character makes a study of these nuclei a real challenge for the experimentalist. For the nucleus ^{97}Rb - the most exotic one studied in this work - only the features of the ground state were known before the measurement presented here. Many nuclear structure studies focus on even-even nuclei. Due to the strong influence of the residual pairing force, these nuclei exhibit a much more simple structure than odd-A nuclei. The influence of the one odd particle in the nucleonic system is large. Not only do single particle excitations appear at low energies but also the collective structure is influenced dramatically due to the more complex intrinsic configuration. These influences can be understood only on a microscopic basis. And herein lies the importance of studying odd nuclei for the field of nuclear structure. To understand the evolution of nuclear structure, the appearance of collectivity and phenomena like shape coexistence, it is crucial to know the evolution of single particle energies. The assignment of Nilsson configurations to excited states in odd-A nuclei is one way to learn more about the microscopic structure. Isomers always play a major role in this context. The K=9/2$^+$ isomers in nuclei with neutron number N = 59, e.g., have been studied recently to investigate the role of the up-sloping 9/2[404] orbital in the sudden shape change.

One often reads in introductions that the mass region around A = 100 exhibits a rich variety of nuclear structure phenomena. Low-energy excitations in these nuclei have a very complicated structure would be another way of putting it. It is clear that in order to at least have the hope to get accurate results, theoretical calculations have to be very sophisticated, taking into account sharp changes of ground-state properties, an extended model space due to inclusion of intruding orbitals and pn-interaction and of course multi-configuration mixing. As many effects play a role in this region, it can be risky to simplify, especially for the very exotic nuclei beyond neutron number N=59, where data are scarce and models cannot be firmly tested. This is also the reason why new information is crucial for our understanding of this region.

The measurements of lifetimes of excited states in this region are very important because these can deliver information on the structure of the states. Lifetime measurements in exotic nuclei meet several challenges. The fast timing technique experiences a renaissance for several years. The implementation of fast $\mathrm{LaBr_3(Ce)}$ scintillation detectors allows for γ-γ delayed coincidence measurements of lifetimes down to several pico seconds. In one experiment, performed within the scope of this thesis, this technique was combined for the first time with a fission fragment separator to study very neutron-rich nuclei. Recently, the first (n, fission) experiment with a large LaBr array was conducted with very promising first results.

Chapter 1

Theoretical concepts

This chapter reviews some theoretical concepts of nuclear structure physics. A special emphasis is placed on deformed odd-A nuclei far from closed shells. The overview includes an introduction to nuclear structure models which are important for the understanding of the mass region studied within the scope of this thesis, namely the nuclear shell model, the Nilsson model, the quasi-particle rotor model (QPRM) and the interacting boson fermion model (IBFM). Furthermore, a recapitulation of the present understanding and interpretation of the sudden onset of deformation at N = 60 in the mass region around A = 100 is presented in Section 1.6. This section also serves as a general motivation for experiments in this mass region, as they were performed within the scope of this thesis.

1.1 Lifetimes of nuclear excited states

For completeness, the basic concepts and relations concerning nuclear excited states and their decay are briefly pointed out in this first section. If a nucleus is in an excited state, it will decay to a state lower in energy. The probability for this to happen is constant in time and characteristic of the nuclear state. The exact time when a nuclear state will decay is random. However, for a number N of nuclei, the rate of decay is

$$\frac{\mathrm{d}N(t)}{\mathrm{d}t} = -\lambda N(t)$$

with the decay constant λ. The solution of this differential equation is the well known radioactive decay law

$$N(t) = N_0\ e^{-\lambda t} \tag{1.1}$$

which governs many naturally occurring representations of decay. The inverse of the decay constant λ is the mean lifetime τ (often just called lifetime). Throughout this work, τ and λ will be used when discussing transition probabilities. However, measuring values will be given as the halflife $T_{1/2} = ln(2)\tau$, like it is customary in nuclear physics literature and data bases.

The decay constant is a fundamental property of any excited state and an important observable for nuclear structure physics. It is directly related to the wave function of the initial and final state. Its calculation is a textbook example for the application of time-dependent perturbation theory. The result is called *Fermi's Golden Rule*

$$\lambda = \frac{2\pi}{\hbar}|m_{fi}|^2\rho(E) \tag{1.2}$$

with the density of final states $\rho(E)$ and the transition matrix element

$$m_{fi} = \langle\Psi_f|m|\Psi_i\rangle \tag{1.3}$$

of the initial and final (approximately) stationary wave functions of the system. For electromagnetic transitions with character σL (σ =E,M) the magnitude of λ strongly depends on spin and parity J^π of the initial and final state and their energy difference E_{trans}. When comparing measured lifetimes to transition probabilities calculated with a theoretical model, usually the reduced transition probability $B(\sigma L; J_1 \to J_2)$ is used instead of λ. It results from summation over the magnetic substates $-J \leq M \leq J$ and $-L \leq \mu \leq L$ (see e.g. [1]).

$$B(\sigma L; J_1 \to J_2) = \Sigma_{\mu M_2}|\langle J_2 M_2|m(\sigma L,\mu)|J_1 M_1\rangle|^2 = (2J_1+1)^{-1}|\langle J_2\|m(\sigma L)\|J_1\rangle|^2 \ . \tag{1.4}$$

The reduced transition matrix element $\langle J_2\|m(\sigma L)\|J_1\rangle$ is related to m_{fi} through the Clebsch-Gordan coefficients $(J_1 L M_1 \mu|J_2 M_2)$:

$$\langle J_2 M_2|m(\sigma L,\mu)|J_1 M_1\rangle = \frac{1}{\sqrt{2J_1+1}}(J_1 L M_1 \mu|J_2 M_2)\langle J_2\|m(\sigma L)\|J_1\rangle \tag{1.5}$$

If an excited nuclear state has more than one possible decay branch, like for example γ transitions to different lower lying states, then the decay constant is a sum

$$\lambda = \lambda_{\gamma_1} + \lambda_{\gamma_2} + \ldots$$

of the single decay constants. Sometimes partial lifetimes are addressed in the literature:

$$\frac{1}{\tau} = \frac{1}{\tau_1} + \frac{1}{\tau_2} + \ldots$$

For a given state only the total mean lifetime can be directly observed experimentally. The measurement of branching ratios λ_1/λ_1, which is in most cases a smaller experimental challenge than the determination of λ, can already reveal vital nuclear structure information. The Alaga rules, for example, are used to identify intraband and interband transitions in deformed nuclei (see for example [2]).

The relation between the mean lifetime $\tau_\gamma = \frac{1}{\lambda_\gamma}$ of an electromagnetic transition and the reduced transition strength for some low L multipolarities is given below [3]:

$$B(E1) = 0.63 \times 10^{-15} E^{-3}\ \lambda_\gamma(E1) \tag{1.6}$$
$$B(M2) = 0,74 \times 10^{-7} E^{-5}\ \lambda_\gamma(M2) \tag{1.7}$$

$$B(M1) = 0.57 \times 10^{-13} E^{-3}\ \lambda_\gamma(M1) \tag{1.8}$$
$$B(E2) = 1.57 \times 10^{-9} E^{-5}\ \lambda_\gamma(E2) \tag{1.9}$$

$$B(E3) = 0,18 \times 10^{-2} E^{-7}\ \lambda_\gamma(E3) \tag{1.10}$$

with $E = E_{\mathrm{trans}} \approx E_\gamma$ in units of MeV and λ_γ in 1/s. Note that internal conversion is not included here (see below). The reduced matrix elements for $\sigma = E, M$ have units $e^2(\mathrm{fm})^{2L}$ and $(e\hbar/2Mc)^2(\mathrm{fm})^{2L-2}$ respectively. Another frequently encountered unit for reduced transition rates is the Weisskopf unit (W.u.) [4], based on single particle transition strength. They allow for the comparison of transition strengths in different nuclei. A transition rate with a value in W.u. much larger than unity points to a collective transition.

Angular momentum coupling, expressing itself through the Clebsch-Gordan coefficients in 1.5, determines the following selection rules for electromagnetic transitions by emission of a γ quantum:

$$|J_i - J_f| \leq \Delta L \leq J_i + J_f \quad \text{and} \quad \Delta L > 0 \tag{1.11}$$

$$\Delta\pi = \begin{cases} (-1)^L & \text{if} \quad \sigma = \mathrm{E} \\ (-1)^{L+1} & \text{if} \quad \sigma = \mathrm{M}\ . \end{cases} \tag{1.12}$$

Besides γ ray emission, internal conversion is another mechanism by which an excited nuclear state can decay. So the decay constant is given by

$$\lambda = \lambda_\gamma + \lambda_{\mathrm{ic}}\ .$$

The energy is transferred to an electron in the atomic shell, which is then emitted with an energy $E_e = E_{\mathrm{trans}} - E_{\mathrm{bind}}$. The binding energy E_{bind} depends on the atomic shell in which the electron was situated at the time of interaction, which leads to an emission spectrum of several discrete lines, corresponding to the different shells and sub shells (see Figure 2.11). The total decay constant for internal conversion is the sum $\lambda_{\mathrm{ic}} = \lambda_{\mathrm{K}} + \lambda_{\mathrm{L}} + \lambda_{\mathrm{M}} + ...$ of the values for the electronic sub shells. The internal conversion coefficient is defined as $\alpha = \frac{\lambda_\gamma}{\lambda_{\mathrm{ic}}}$. The total transition probability can then be written as

$$\lambda = \lambda_\gamma + \lambda_{\mathrm{ic}} = \lambda_\gamma(1 + \alpha)\ .$$

The ratio α can become very large under certain circumstances. Conditions which favour internal conversion over γ ray emission are high atomic number Z, low transition energy and high multipolarity L of the transition. Because internal conversion is, like γ emission, based on electromagnetic interaction, the selection rules from Equation (1.11) and Equation (1.12) apply as well. However, contrary to γ emission, internal conversion transitions with $\Delta L = 0$ are allowed. In this case, α is not defined. A good estimate for the value of α, albeit done with several coarse assumptions, is given by the following equations (see e.g. [5]):

$$\alpha(EL) = \frac{Z^3}{n^3}\left(\frac{L}{L+1}\right)\left(\frac{e^2}{4\pi\epsilon_0\hbar c}\right)^4\left(\frac{2m_ec^2}{E}\right)^{L+5/2}, \tag{1.13}$$

$$\alpha(ML) = \frac{Z^3}{n^3}\left(\frac{e^2}{4\pi\epsilon_0\hbar c}\right)^4\left(\frac{2m_ec^2}{E}\right)^{L+3/2} \tag{1.14}$$

The ratio α depends very little on the nuclear structure part of the transition matrix elements, because these are the same for γ emission and internal conversion. The remaining part is governed by electrodynamics. It can be calculated quite accurately from first principles in self consistent relativistic Dirac Fock calculations of the atomic shell [6]. The result can then, in turn, be used to retrieve information on the nuclear transition. The internal conversion coefficient α, as well as the sub shell coefficients (α_{K}, α_{L},...), are very sensitive to the transition multipolarity σL, as can be seen from the estimates in Equation (1.13). The same is true for the ratios $\alpha_{\mathrm{K}}/\alpha_{\mathrm{L}}$, $\alpha_{\mathrm{K}}/\alpha_{\mathrm{M}}$, etc. That means by measuring total or relative conversion coefficients, and comparing them with calculations, the determination of multipolarities is possible.

1.2 The shell model, the Nilsson model, and deformation driving mechanisms

The nuclear shell model is a theoretical model to describe the atomic nucleus. It was introduced by M. Goeppert-Mayer and J. Jensen in 1949 and is studied and improved since then (cf. [3, 7]). The atomic nucleus is a many-body problem and should in principle be treated in terms of the nucleon-nucleon interaction, based on the strong force between quarks. As protons and neutrons are not elementary particles, the force between two nucleons is a residual interaction with complex features. The dimension of this problem, even if only two-nucleon interactions are taken into account, is too large to be calculated even with modern day means. The shell model makes the assumption that the complicated interactions can be approximated by a spherical mean potential for one particle $H_0(i)$, generated by all nuclei, and separable residual interactions V_{res}, which make up for effects like pairing:

$$H = \sum_i H_0(i) + V_{\mathrm{res}}.$$

The model was very successful since its early days, as it was able to describe many phenomena like, e.g., magic numbers, the 0^+ ground state spin of even even nuclei and nuclear masses, based on a single frame work for all nuclei [2]. The nuclear shell model is called microscopic, opposed to macroscopic models like the geometric models which describe nuclear excitations as collective excitations like vibrations or rotations. In principle, the shell model takes into account all the nucleons which make up a particular nucleus, but this model space often has to be truncated to the valence nuclei outside closed shells for calculation of the residual matrix elements. The space of possible single particle states is again truncated. these truncations are necessary because calculations quickly become very complex with increasing number of nucleons, to a degree where they cannot be handled in a reasonable amount of time by contemporary computers. On the other hand, the fact that the truncated model space still yields reasonable descriptions of many nuclei can be considered a result itself. The concept of valence nucleons is very important and can be considered one of the main contributions of the nuclear shell model to nuclear structure theory.

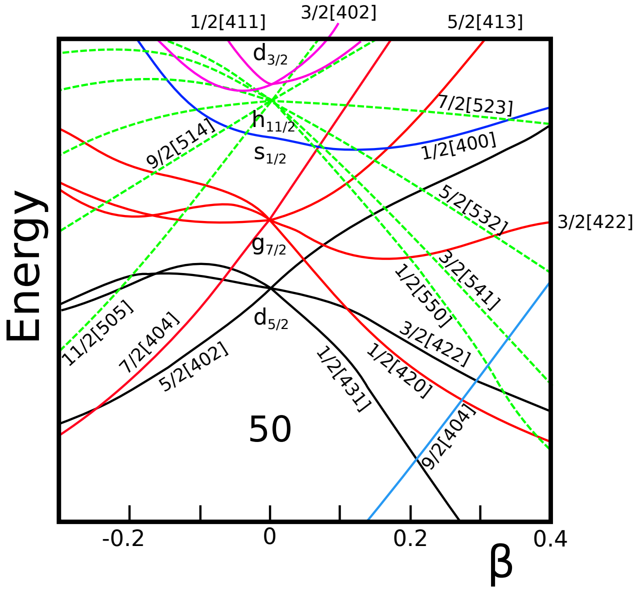

Figure 1.1: Nilsson diagram for protons above the closed shell at Z=50. Positive parity states are drawn as full lines, negative parity states as dashed lines. The figure is reproduced schematically from [8].

An interesting feature of nuclear structure is deformation. It has been known for a long time, that heavy nuclei with many valence particles of both kinds tend to take on a static prolate axially symmetric quadrupole deformation in their ground state [2]. Regular rotational excitation bands are beautiful evidence of this fact. Excitations and behaviour of deformed even-even nuclei can be very successfully described using collective models (cf., e.g., [1, 2]), but matters become more difficult for odd-A nuclei, because single particle excitations of the odd particle play a role already at low excitation energies.

A model that can describe such nuclei is the Nilsson model. An enlightening introduction can be found in [2]. In this model the nuclear mean field is no longer fixed to be spherical, like in the nuclear shell model, but can be deformed. In the deformed field the single particle orbitals for a given total spin j and angular momentum l of a shell model state split up in energy, depending on the magnetic quantum number, as shown in Figure 1.1 for protons outside the $Z = 50$ shell. As spherical symmetry is spontaneously broken in the intrinsic frame, angular momentum is no longer a good quantum number. Instead the projection Ω of the total single particle spin j on the symmetry axis, is a good quantum number, and used to label the states. These projections correspond to the magnetic substates of the original shell model states. For prolate deformation ($\beta > 0$) the low Ω states decrease in energy, forming down-sloping lines in the Nilsson diagram shown in Figure 1.1, while high Ω states go up. Each of these Nilsson states is two fold degenerate. Negative and positive values of Ω, i.e., clockwise and counterclockwise rotation, have the same energy.

In our discussion until now only the single particle value j was considered. The deformed core can also carry spin, and angular momentum coupling leads to a total spin J. This is done, e.g., in the particle rotor model, discussed in Section 1.3. The

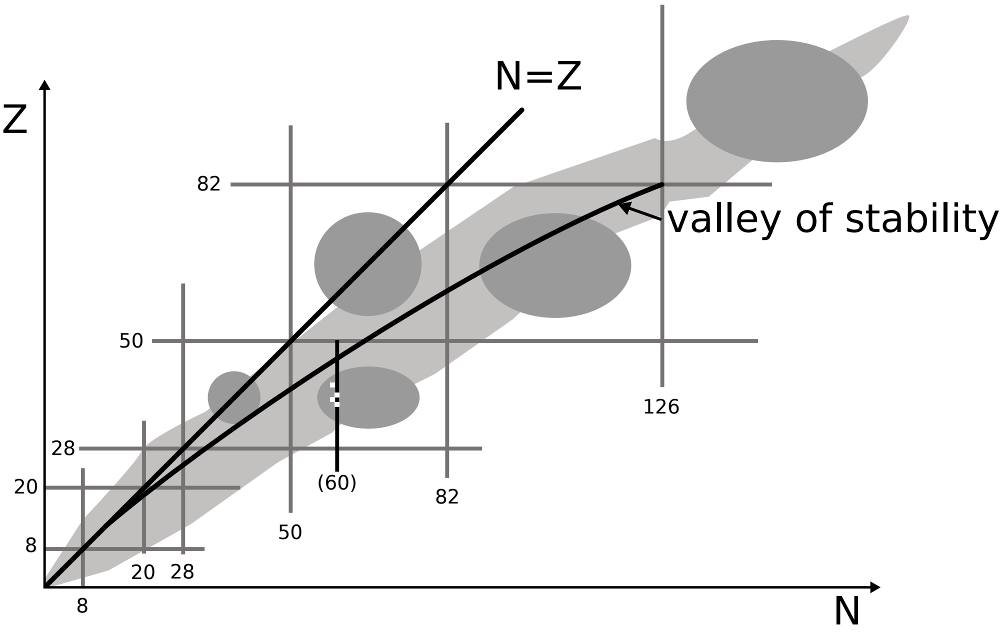

Figure 1.2: The chart of nuclei. The light grey area indicates known nuclei (approximate). Regions where nuclear deformation is expected are shown in dark grey. Apart from the magic numbers, the N = 60 isotone line is also shown. Nuclei studied within the scope of this thesis are marked as white squares.

projection of the total spin J is called K. For axially symmetric nuclei, the collective rotation is perpendicular to the symmetry axis, and thus contributes nothing to the projection, so $\Omega = K$ in this case. As mentioned before, l is no longer a good quantum number, and thus mixing will happen if two states with the same K quantum number and parity come close. This makes the unique parity orbitals, like $h_{11/2}$ between the magic numbers 50 and 80, special, because they are very pure, even at large deformations. Including mixing of the wave functions in the oscillator basis, the new order of single particle states at a given deformation can be calculated. The resulting eigenfunctions, the Nilsson states, are labelled $K^\pi[Nn_z\Lambda]$. The numbers in brackets are the major oscillator shell quantum number N, the number of nodes along the symmetry axis n_z and the projection of l along this axis, Λ. K is the only good quantum number of the system, but at large deformation, N, n_z and Λ are asymptotically conserved. With this approach the ground state spin of most deformed odd-A nuclei can be deduced by finding the Fermi surface, if the deformation of the nucleus is experimentally known. Note, that in this simple case deformation is an input parameter to the model and is not predicted.

The model can, however, be used to identify deformation driving mechanisms, i.e., circumstances under which deformation will occur. Inspection of a Nilsson diagram makes clear that doubly closed shell nuclei have spherical ground states, because for any magic number of nucleons, the spherical configuration is the lowest energy state. In both directions, prolate or oblate, there only lie up-sloping orbitals - with high K or low K respectively. As all orbitals are fully occupied, all magnetic substates are fully occupied as well. The resulting mean spacial distribution is therefore spherical.

At mid-shell, however, orbitals are only partially filled. Any interaction that favours certain magnetic substates can now lead to a deformed ground state. Such a scenario is exactly encountered in the Nilsson diagram shown in Figure 1.1. On the prolate side, the energies of low K states slope down. At a certain point the single particle states close to the Fermi surface are all formed by states with low K. These states also mix, which pushes the low orbitals down even more. The more valence nucleons are present, the more pronounced this effect gets and finally the deformed configuration is the ground state of the system. A major role in this context is also played by the proton-neutron interaction and intruder states from the next major shell [2]. Protons and neutrons in shell model orbitals with equal l and $\Delta j = 1$, the so called spin orbit partners, attract each other particularly strong. This p-n interaction phenomenon, can reduce the energy difference of the involved single particle orbits and in this way can even obliterate shell gaps. The ensuing increase of valence particles then again favours deformation. Regions where static nuclear ground state deformation is expected are shown in Figure 1.2.

In Figure 1.1 it can be seen, that the evolution of single particle energies for negative and positive values of β is not symmetrical. Indeed, the fact that most deformed nuclei take on a prolate, rather than an oblate, shape can also be understood in terms of the Nilsson model, as pointed out in [2].

An implementation of the deformed shell model, or Nilsson model, is the computer code *gampn* [9]. It calculates the single particle states based on a modified oscillator potential for a given deformation. This code was used for the calculation of excited states in ^{99}Y in Section 5.3.

1.3 The quasi-particle rotor model

The Nilsson model, briefly discussed in the previous section, gives a description of the single particle energies of nucleons in a deformed potential. To make predictions for real nuclei, like with the shell model, the model space can be truncated to the valence nucleons, i.e. in this case, the single particle states close to the Fermi surface. As a next step we can assume the core, responsible for the deformed potential, to be itself excited by rotating. This phenomenon is very well known for nuclei with a deformed ground state. In these nuclei, collective rotations based on the ground state appear among the lowest lying modes of excitation. In even-even nuclei the lowest excitation is almost always a 2^+ state, which is the lowest allowed rotational state for a 0^+ ground state. The structure of rotational excitations in nuclei is usually described in terms of the collective geometrical model, often called Bohr-Mottelson-model [1]. The mean shape of the nucleus is given by deformation parameters $\beta_2, \beta_3, \beta_4, ...$ This model has been extensively studied since the beginning of nuclear structure physics. Many refinements, e.g. variable moment of inertia in a rotational band, have been introduced and were successfully applied to describe nuclear structure phenomena. Within the scope of this thesis the discussion will be restricted to axially symmetric quadrupole deformation ($\beta_3 = \beta_4 = \cdots = 0$). Among the general predictions of this model, the most well known one is probably that the ratio of $R_{4/2} = E_{4_1^+}/E_{2_1^+}$ in rotational even even nuclei takes the value $R_{4/2} = 3\frac{1}{3}$. This is experimentally confirmed for many nuclei which exhibit rotational like spectra. As Casten remarks in [2], a value of $R_{4/2}$ close to 3.3 indicates a static deformation, but not how large this deformation is. $R_{4/2} < 3.3$ means a non static, unstable deformation, rather than a small one.

Generally this model also applies for collective excitations in nuclei that are not even even. However, these collective patterns in odd-odd and odd-A nuclei are not as obvious as in even-even nuclei, because low energy excitations of one or few nucleons are possible which couple to the collective excitations and form new band heads. This makes the low energy spectrum of nuclei which are not even-even notoriously more complex.

One model to describe this kind of situation is the quasi-particle rotor model. It is applicable to both, odd-A and odd-odd nuclei. The description here will be limited to the odd-A case. This model is quite powerful, because it extends the microscopic aspects of the nuclear shell model to regions where this model, due to computational limitations, is no longer feasible, namely deformed nuclei with a lot of valence particles. The inert core used in shell model calculations is treated macroscopically in the collective model and then coupled to a quasi-particle occupying the single particle Nilsson orbitals close to the Fermi surface. A quasi-particle is used, instead of a single nucleon, because the residual pairing interaction allows scattering of nucleon pairs to close lying orbitals [2]. This pairing effect is usually treated in a BCS coupling scheme [10] with the pairing gap Δ and the Fermi energy λ. In the resulting eigenfunctions, the intrinsic character is given by the quantum numbers of the quasi-particle, which are the same as in the Nilsson model. However, there can be substantial mixing in these states, and it can generally not be expected to label a band with one single Nilsson configuration. The coupling to the collective rotation is also far from trivial. For a given state, precession like features lead to complex rotations, stemming from the coupling of the odd particle to the rotor core. Rotational spectra of odd-A nuclei show much more complex phenomena than those of even-even nuclei.

An implementation of this model are the computer codes *gampn*, *asyrmo*, and *probamo* [9]. The single particle states close to the Fermi surface are coupled to the rotor core in the strong coupling basis. This means the projection on the symmetry axis of the coupled single particle and collective spins and angular momenta is a preserved quantity. The calculations of excited states and transition strengths in ^{99}Y, presented in Section 5.3, were done using these codes.

1.4 The interacting boson fermion model

A model which has led to very interesting developments since its proposition by Arima and Iachello [11] is the interacting boson model (IBM) for even even nuclei. In this model the nucleus is described as being consisted not of fermions but of bosons. Because of the very strong pairing force between nucleons this approximation is valid for low energy excitations in even-even nuclei with several valence nucleons. One feature which makes this model so attractive for theoretical studies is, that it can be analytically solved for certain symmetry cases. These are called the limits of the IBM and they appear by demanding certain dynamical symmetries of the Hamiltonian, namely U(5), O(6) and SU(3) [2]. Even more interesting is the fact, that the spectra - and, to a certain degree, transitions rates - predicted by these limits, correspond to the collective geometric models of vibration, γ-unstable rotor and rigid rotor respectively[1]. Each limit predicts selection rules for transitions between excited states. In the U(5) limit for example, all E0 transitions are forbidden. In the SU(3) limit, transitions between the ground state band and the β or γ band are forbidden. Only few nuclei display very closely the characteristics of one particular limit. The limits themselves are still useful for nuclear structure considerations because they provide a new language and new symmetry categories for nuclear structure phenomena. A very interesting application is that the IBM enables the study of phase transitions between the limits, which is possible because the model is able to describe vibrational and rotational collective structure in a single framework.

The simplest version of the IBM is the sd-IBM1. In this model, protons and neutrons are not distinguished. Furthermore, only fermion pairs with total spin $j = 0$ (s bosons) and $j = 2$ (d bosons) are considered. The Hamiltonian of the sd-IBM1 in a multipole-like expansion takes the form [12]

$$H_{\mathrm{IBM}} = \epsilon_d \hat{n}_d + \mathrm{PAIR}(P \cdot P) + \frac{1}{2}\mathrm{ELL}(L \cdot L) + \frac{1}{2}\mathrm{QQ}(\hat{Q}^\chi \cdot \hat{Q}^\chi), \tag{1.15}$$

where the octupole and hexadecapole terms are omitted (OCT = HEX = 0). To avoid confusion, the notation for the parameters ϵ_d, PAIR, ELL, QQ, and χ and the operators $\hat{n}_d$, P, L, and Q^χ is the same as in the computer program *phint*, which was used for the calculation in Section 5.2. $\hat{n}_d$ is the d boson number operator $(d^\dagger \tilde{d})$, the other terms have the form

$$P \cdot P = \frac{1}{2}\left[\{(s^\dagger s^\dagger)^{(0)} - \sqrt{5}(d^\dagger d^\dagger)^{(0)}\} \cdot \{(ss)^{(0)} - \sqrt{5}(\tilde{d}\tilde{d})^{(0)}\}\right]$$

$$L \cdot L = -10\sqrt{3}\left[\{(d^\dagger \tilde{d})^{(1)} + (d^\dagger \tilde{d})^{(1)}\}\right]$$

$$Q^\chi = \sqrt{5}\left[\{(s^\dagger \tilde{d} + d^\dagger s)^{(2)} + \frac{\chi}{\sqrt{5}}(d^\dagger \tilde{d})^{(2)}\} \cdot \{(s^\dagger \tilde{d} + d^\dagger s)^{(2)} + \frac{\chi}{\sqrt{5}}(d^\dagger \tilde{d})^{(2)}\}\right]$$

The extension of the model to odd-A nuclei is called the interacting boson fermion model (IBFM) [13]. It introduces an additional fermion to be coupled to the bosons. The possible states of this single fermion are determined by the corresponding shell model single particle states.

The IBM Hamiltonian H_{IBM} is extended for a fermion part H_F and a boson-fermion interaction V_{BF}

$$H_{\mathrm{IBFM}} = H_{\mathrm{IBM}} + H_F + V_{BF}. \tag{1.16}$$

Like in the quasi-particle rotor model, the odd nucleon in the model is considered as a quasi particle which occupies quasi-particle states with energies ϵ_k. The Hamiltonian is

$$H_F = \sum_k \epsilon_k \hat{n}_k,$$

---

[1] This is only exactly the case in the limit of an infinite number of bosons.

where k labels the quasi-particle states and $\hat{n}_k$ is the quasi-particle number operator for the state k.

The boson-fermion interaction V_{BF} is the crucial part of the model. It will not be discussed in more detail here, and the reader is referred to [13]. Basically, the interaction is governed by a monopole and a quadrupole term (containing the paramete χ from equation (1.15)) and a term that is called exchange interaction. The parameters are usually called A_0, Γ_0, and Λ_0 respectively [13].

The sd-IBM1 parameters are fitted to the even-even core and not changed afterwards. The IBFM model has the three free parameters Λ_0, Γ_0, and A_0 to fit the data of the odd-mass nucleus. Single particle energies can also be adjusted, which is physically justified in certain cases. This is the case in the neutron $d_{5/2}$, $g_{7/2}$, $s_{1/2}$, $h_{11/2}$, $d_{3/2}$ shell, where the $g_{7/2}$ single particle energy shifts as much as 2 MeV between proton number Z=36 and Z=50 [14].

1.5 Isomeric excited states in nuclei

In nuclear physics, isomers are nuclear excited states with a long lifetime. But at which point exactly is a lifetime “long enough” for the state to be considered an isomer? A clear answer to this question is not easy since the term is more of a practical classification than a stringent physics definition. The first definition I heard as a student was: “An isomer is an excited state in a nucleus which lives so long, that its halflife can be measured”, with the immediate relativisation: “This definition is not very handy nowadays”. Several experimental methods have been established during the past decades, which allow for the measurement of lifetimes in the femtosecond region and below[2]. That means, following the definition above, pretty much every known state is an isomer, thus making the category *isomer* superfluous. A possible definition is that an isomer is an excited state in a nucleus that undergoes β or α decay into a different nucleus. This definition is more restrictive than the first one, and still holds in it the historic significance of isomers in the first studies of radioactive decay[3].

Nowadays, in nuclear physics, generally those states are called isomers which have halflifes several orders of magnitude larger than those ordinarily found or expected. When referring to an isotope using the notation with chemical symbols, an m is appended to the mass number A, e.g. ^{88m}Br. The m indicates a meta stable state in the nucleus that is not the ground state. Isomers are sometimes referred to including the order of magnitude of their halflife, e.g., ms isomer or μs isomer.

From a nuclear structure point of view, isomers are very interesting. Transition rates are observables very sensitive to the nuclear structure of the states involved (see Section 1.1). Most nuclear excited states encountered have lifetimes of several picoseconds or far below. But if structure or selection rules do not allow fast transitions to lower-lying

---

[2] See [15] for review of lifetime measurement techniques.

[3] The first to observe isomerism in a nucleus was O. Hahn, when he found a new β transition of a decay product of ^{234}Th [16]. What he observed was the β decay of the ^{234}Pa ground state, that of the short lived isomer was already known. Only several years later an interpretation of isomers as meta stable states was proposed by Weizsäcker [17].

states, much longer lifetimes can occur. Thus, prediction of isomers is a good test for nuclear structure models and their selection rules. In particular validation tests of selection rules increase our understanding of nuclear structure, because these rules are closely linked to symmetries of the system or them being broken (some selection rules are discussed in the Sections 1.1-1.4).

Isomeric states often have influence on experimental procedures, which makes it useful to have a special name for them. For example, isomers complicate γ-γ correlation measurements. If a state with a lifetime much larger than the coincidence window is heavily populated during the deexcitation cascade, no prompt correlation is possible between those transitions above and below the isomer. If the isomer is not known, this will lead to a wrong or incomplete level scheme. Isomers can also pose a problem for in-beam γ γ angular correlation measurements, because nuclear spin orientation alignment will decrease or vanish completely during the mean lifetime of an isomer. For experiments with radioactive beams, isomers become important because the exotic nuclei are produced far from the place where their decay is studied. The relative population of ground state and isomeric states at the point of measurement can be important - to desired or undesired effect - in certain experiments. Depending on the scenario, lifetimes down to about one nanosecond are considered isomeric. On the other hand excited states are known, which live longer than the ground state of the respective nucleus, like, e.g., the 9^- spin isomer in ^{180m}Ta (see below).

With this in mind it becomes clear that isomers - and a precise knowledge of their halflife - play an important role in understanding experimental data, in building decay schemes and in the development and improvement of nuclear structure theories.

There are several mechanisms which lead to isomerism. The most prominent categories of isomers will be briefly discussed in the following.

Spin isomers

A spin isomer is an excited nuclear state with a total angular momentum J^π which is very different to any state that it could decay to. Some authors call such a state a spin trap [18]. Following equation (1.9), electromagnetic transition rates strongly decrease with increasing angular momentum L carried away by the emitted radiation. For a transition between two states, angular momentum selection rules demand $L \geq \Delta J$. The lowest possible multipole mode dominates the transition (for electric and magnetic transitions respectively). The same is the case for internal conversion (see equation (1.13)). From equation (1.9) it can also be seen, that a low transition energy E_{trans} results in a slow transition. For an EL transition, the halflife is proportional to E_{trans}^{2L+1}. In this way, very long lived isomers can form.

An example for a spin isomer in the mass region investigated within the scope of this thesis is the $(27/2^-)$ state at 3523 keV in ^{97}Y, which decays mainly via an E3 transition [19]. Due to the rapid decrease of transition probability with increasing L, this multipole order can only be observed if all lower multipole transitions are forbidden. Another prominent example, found in the rare earth region, is $^{180\mathrm{m}}$Ta. This isotope exists naturally, even though its 1^+ ground state has a halflife of only 8.15 h [20]. There is, however, a 9^- isomer at 77 keV with a measured lower halflife limit of

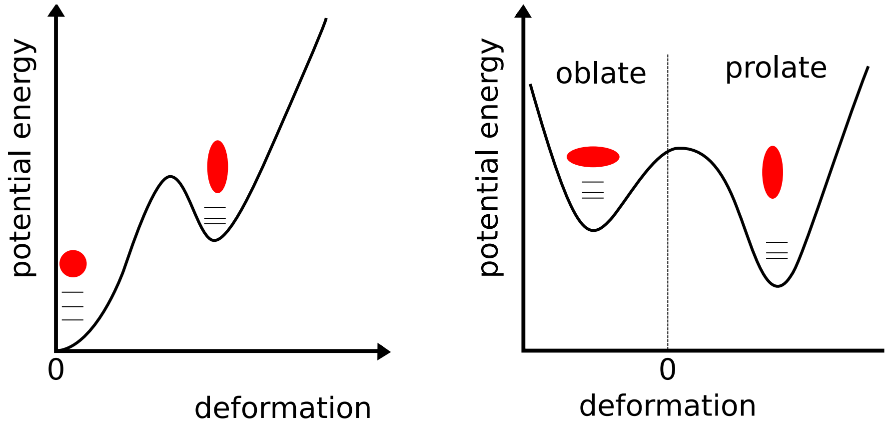

Figure 1.3: Schematic depiction of shape isomers. A second local minimum in the potential energy surface gives rise to excited states with a different deformation than the ground state.

$T_{1/2} > 1.2\times10^{15}$ a. For this state, the possible decays having the lowest multipole order are an M8/E9 to the ground state, and an E7/M8 to the first excited state, which has a spin of 2^{+}. None of the two was ever observed, neither by emission of a γ ray nor a conversion electron. β- or α decay is not observed either; the isomer can be considered stable [21].

K isomers

In deformed nuclei, the projection K of the total angular momentum J onto the symmetry axis is almost a good quantum number (see also Section 1.2). The K quantum number shows how the nucleon's orbit is situated relative to the symmetry axis of the deformed inert core. The selection rule for transitions demands $\Delta J \geq \Delta K$, which means the lowest allowed multipole order for electromagnetic transitions is $L = \Delta K$. These isomers in deformed nuclei are different from pure spin isomers, even though the mechanism is similar. Not only the absolute values of the angular momenta of the states involved are important, but also their projections K. The difference of the total angular momenta of two states could allow a fast E2 transition, but the K selection rules only permit much higher multipolarity, resulting in an isomer. Note, that K is not really a good quantum number in most cases. The axial symmetry is broken and the selection rule is not strict, but only more or less strongly hinders transitions with $L < \Delta K$. A mass region which displays a number of K isomers (also with spin isomer character) is the rare earth region around ^{180}Hf.

Shape isomers

The mechanism that leads to this type of isomer is of collective nature. In the liquid drop model, a shape isomer is an excited state of the nucleus that corresponds to a minimum in the potential energy surface that is different to that of the ground state, as shown in Figure 1.3. Looking at the Nilsson model (see Section 1.2), one can deduce, that a change in shape, i.e. at the lowest order, a change of the quadrupole deformation

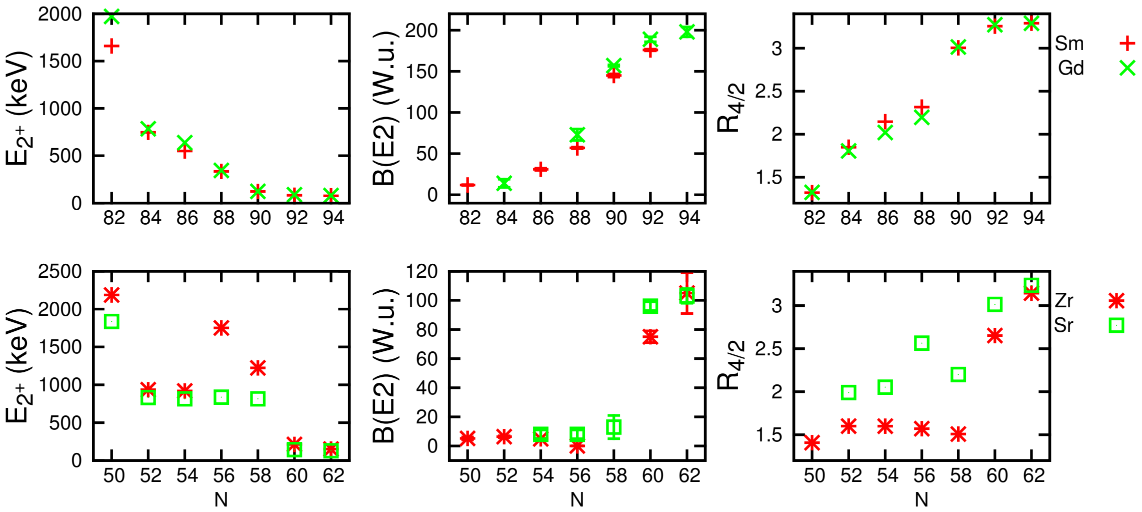

Figure 1.4: Evolution of structure signatures in the A = 100 and A = 140 mass region. Data are taken from the Nuclear Data Sheets [22–37].

parameter β (see Section 1.3), leads to a change in the order of single-particle levels close to the Fermi surface which can result in minima other than the ground state. It is clear, that this also has an effect on the wave function. A transition between two different shapes is strongly hindered, because spontaneously it is only possible by tunnelling. The hindrance strongly depends on the depth of the second minimum and its “distance” to the ground state minimum.

1.6 Sudden onset of deformation at N=60

The neutron rich nuclei in the A = 100 mass region are an active field of nuclear structure studies for decades already. The nuclei in this region display a variety of interesting, and sometimes puzzeling, features. That is true for single nuclei, and even more so for the evolution of nuclear structure - likewise along isotopic and isotonic chains. A picture of this particular section of the nuclear chart can be seen in Figure 1.5. Even the more stable isotopes, like ruthenium and molybdenum, though studied for decades, still pose questions that are heavily debated in the literature. Among the structural phenomena are very low lying 0^+ states along the N = 58 isotonic chain, mixed symmetry states, e.g in molybdenum [38], and the doubly magic character of ^{96}Zr. Triaxiality is observed in rotational bands of rhodium and technetium, but disappears in ^{99}Y. One of the most prominent features of the region is the very sudden onset of deformation at neutron number N = 60. To illustrate this feature, a similar situation, going from a closed shell to larger neutron numbers in the mass region A = 140, is shown in Figure 1.4 for even even nuclei, in comparison to strontium and zirconium isotopes. The figure shows the evolution of $E_{2_1^+}$, $B(E2; 2_1^+ \rightarrow 0_1^+)$ and the ratio $R_{4/2}$ along the respective isotopic chain. This figure also steers attention to a white spot in this region. The 2_1^+ lifetime in ^{98}Zr is still unknown. Only an upper limit of

$T_{1/2} < 11$ ps was measured [39], using β-γ-γ timing. The difference between the picture for the nuclei from the A = 100 region and those from the A = 140 region can clearly be seen. While samarium and gadolinium display a rapid shape change as well, there is a well developed transitional region until stable deformation is reached at N = 92, where strontium shows a pronounced rotor structure until N = 56 and already reaches the maximum deformation at N = 60. A similar behaviour is also found for odd proton nuclei. Figure 1.6 shows the evolution of the ground state quadrupole moment Q_0 for rubidium isotopes. Due to the sub shell closure at Z = 40, the observables jump even farther for zirconium isotopes. Exactly this is also the reason for the sudden jump to deformation, as was first proposed by Federman and Pittel [40]. Rather than a sudden onset of deformation, the phenomenon can be interpreted as an unusual endurance of sphericity relatively far away from the well known closed shell of stable nuclei at N = 50. Indeed it is the microscopic interaction of protons and neutrons in the particular arrangement of single particle orbitals of this region which first inhibits collectivity by forming a subshell closure which is then suddenly obliterated, with the effect of a suddenly increased valence space. The leading actors of this spectacle are the proton $g_{9/2}$, $h_{11/2}$ and neutron $g_{7/2}$, $h_{9/2}$ shell model orbitals [2]. In recent years more and more exotic nuclei in the region are studied. This includes the investigation of deformation saturation beyond N = 60 and also the role of the protons in the various observed

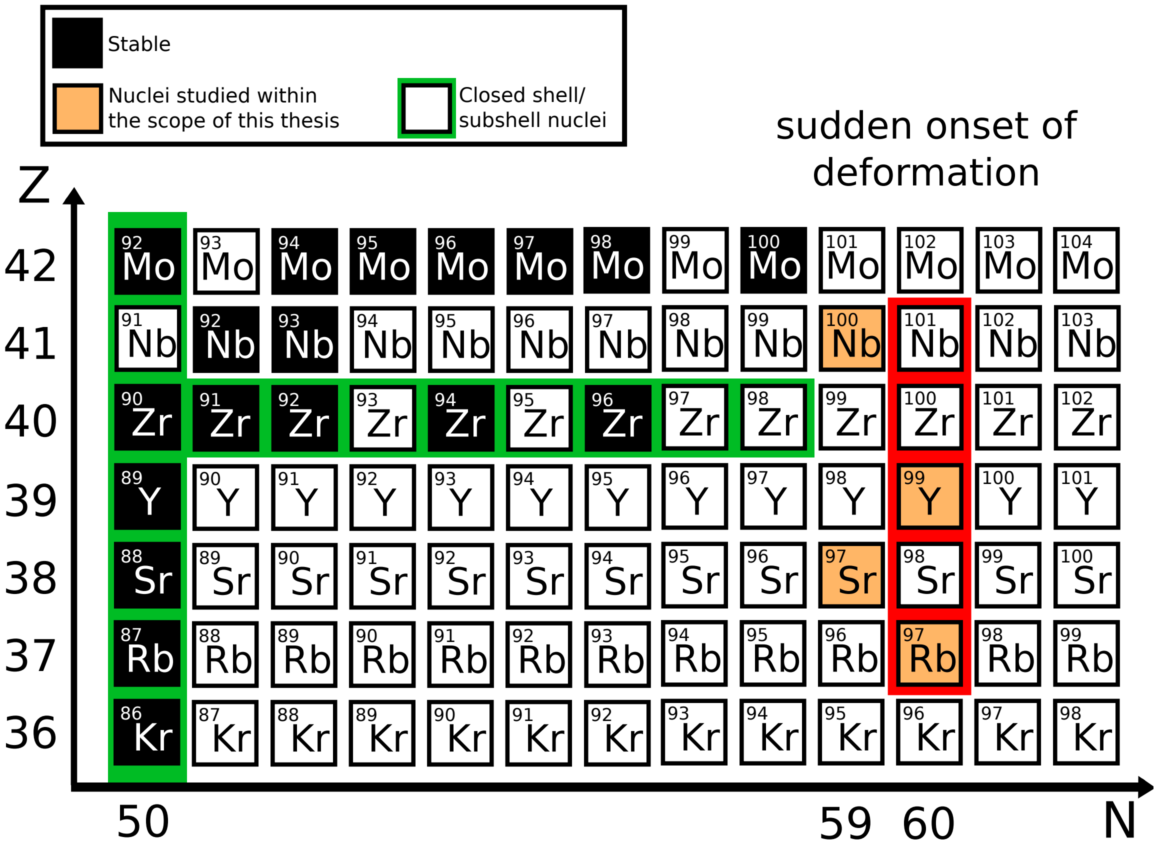

Figure 1.5: The chart of nuclei for the A = 100 mass region. The region of sudden onset of deformation is marked in red.

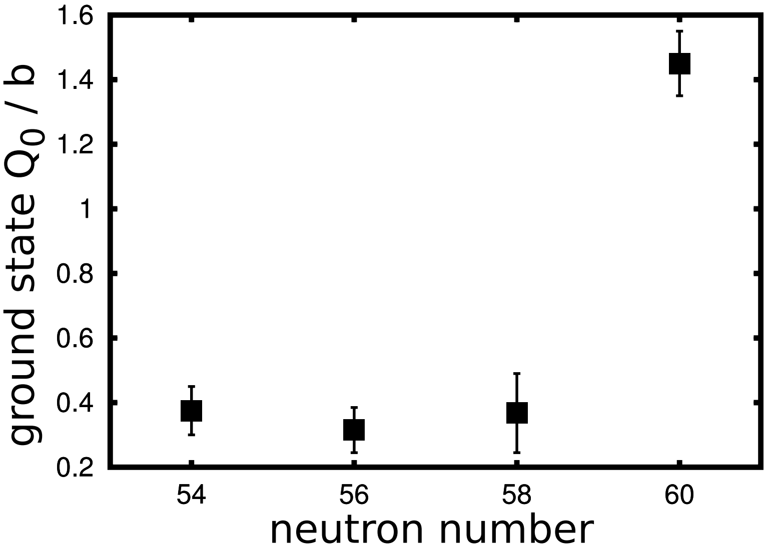

Figure 1.6: Spectroscopic quadrupole moment for odd mass rubidium isotopes (Z = 37). Values were calculated using data from the Nuclear Data Sheets [19, 45–47].

phenomena. It was, for example, shown, that the evolution of collectivity is smooth in the krypton isotopes [41]. Another present field of research is shape coexistence in N = 58 and N = 59 isotones [42]. Odd-A and odd-odd nuclei in this region are studied because they give vital information on microscopic single particle aspects. This includes the identification of intruder states from the next major shell. The identification of the $K = 9/2^+$ shape isomers in ^{97}Sr and ^{99}Zr is a good example how data in odd-A nuclei can help to understand the role of neutron orbitals played in the transitional nuclei with N = 59 [43]. In this region there is also prolate-oblate shape coexistence predicted by theoretical calculations [44]. There is some indication for this in the data on ^{97}Rb, presented in Section 3.1 and discussed in Section 5.1. It is desired to have a nuclear model that can describe the evolution of structure in this mass region in one single frame work. The IBM, e.g., is in principle able to describe the different collective modes, also in terms of a shape phase transition [48]. A very promising development concerning this unified description is the recently proposed mapping procedure to obtain IBM wave functions and eigenvalues on the basis of microscopic energy density functional theory. This formalism showed promising results in describing shape coexistence in ^{98}Mo [38]. The author is convinced the investigation of this region will keep nuclear physicists, experimentalists and theoreticians alike, busy for quite some time longer.

Chapter 2

Applied experimental methods

This chapter is intended to give an overview of the main experimental methods and devices that were applied in this work. The method of electronic lifetime measurements using delayed coincidences is introduced and briefly reviewed in the first Section. The Lohengrin mass spectrometer, which was used to separate the fission fragments, is described, as are the experimental methods of fast electronic timing and electron spectroscopy. More detailed accounts of the single experiments are given in the respective sections of Chapter 3 and 4.

2.1 Lifetime measurements

The lifetime τ of a nuclear excited state is an important observable in nuclear structure physics. The transition rate $\lambda = 1/\tau$ is sensitive to the structure of the nuclear wave functions of the states involved. Precise lifetime measurements are therefore crucial for testing and developing nuclear structure models and to solidify and expand out understanding of the complex system that is the atomic nucleus. Different techniques had to be developed, to accommodate the wide range of lifetimes that occur in the nuclear system. A review of the most common techniques can be found in [15]. In this Chapter the method of electronic fast timing, often referred to as delayed coincidence method, is presented. This method was used for lifetime measurements within the scope of this thesis. Section 2.1.1 introduces the principle idea of electronic fast timing in delayed coincidence experiments. Section 2.1.2 is dedicated to $\mathrm{LaBr_3(Ce)}$ scintillator detectors and their application in electronic fast experiments. The last three Sections deal with the analysis of time spectra.

In the following only a brief introduction on electronic fast timing and the analysis of time spectra is given, the main purpose of which is to introduce important concepts and definitions. For an exhaustive review and comprehensive study of the technique and its application in nuclear physics experiments the reader is referred to [49] and references therein.

2.1.1 Electronic fast timing

The general idea behind the experimental technique of electronic fast timing in nuclear physics is the direct determination of the time difference between two measurement signals (start and stop) with the goal to extract the lifetime of a nuclear state. One signal determines the moment of population of the state of interest (feeder), the other its decay (see Figure 2.1 (a,b,c)). Principally any measurable event which determines the population or decay within the desired accuracy can be used. For lifetime measurements of nuclear excited states the time reference for population is generally determined by direct reaction or decay products such as scattered particles, implanted ions, β or γ radiation. The time reference of a pulsed beam has also been used for this purpose [49]. As reference for the decay of a nuclear excited state, the first choice is radiation from directly depopulating transitions. The technique is also called delayed coincidence method. This name alludes to the fact that the experiment has to allow for a clear correlation of the two signals in order for them to be assigned to one and the same deexcitation process. This is also a reason for the de-facto upper limit of $\tau \leq 10^{-6}$ s for lifetimes measurable with this method, as quoted, for example, in [15]. To determine lifetimes in the millisecond region and above, the time dependent activity of a nucleus in a certain state can be measured instead of the time difference between population and decay of this excited state in individual nucleons via delayed coincidence measurements. Both methods measure the distribution N(t) which is governed by the radioactive decay law (see equation (1.1)). But they are applicable to different lifetime regions.

As a matter of principle, all experimental fast timing setups have three stages. One to measure a signal from the physical events that mark population and decay. A second one to get a consistent time reference from these signals, the so-called time pick off. A third component is needed to measure the difference between two such time references. There exists a number of possible implementations of these three stages. In fast timing experiments with scintillator detectors, a setup like the one shown in Figure 2.1 (d) is common. Scintillator signals are sent through a constant fraction discriminator (CFD) for time walk minimisation. The shape of the CFD output signal is uniform and has a sharp flank. A time to amplitude converter (TAC) measures the time difference between the signals at its start (detector 1) and stop (detector 2) input. The TAC signal $T(E_1, E_2)$ is recorded in coincidence with the two detector energy signals E_1 and E_2. A gate can then be applied to select a decay cascade. In another implementation the fast filter signal from a digital gamma finder can be used as signal time reference. The determination of the time difference is then a simple subtraction of two counter values of internal clock ticks. Which implementation is applied depends on the detectors which are used and on the aspired accuracy. The internal clock of xia DGF 4C, revisionE modules[1], as they were used for data recording in the experiments described in Chapter 3, operates at 40 MHz. This corresponds to one clock tic every 25 ns - much too long for measurements in the picosecond region, but sufficient for lifetime measurements of μs isomers.

The result of a fast timing measurement is a time difference spectrum, which follows the law of radioactive decay (see Section 1.1). The lifetime is then extracted from the

---

[1] Xia digital gamma finder (DGF) 4C revision E, www.xia.com/Manuals/

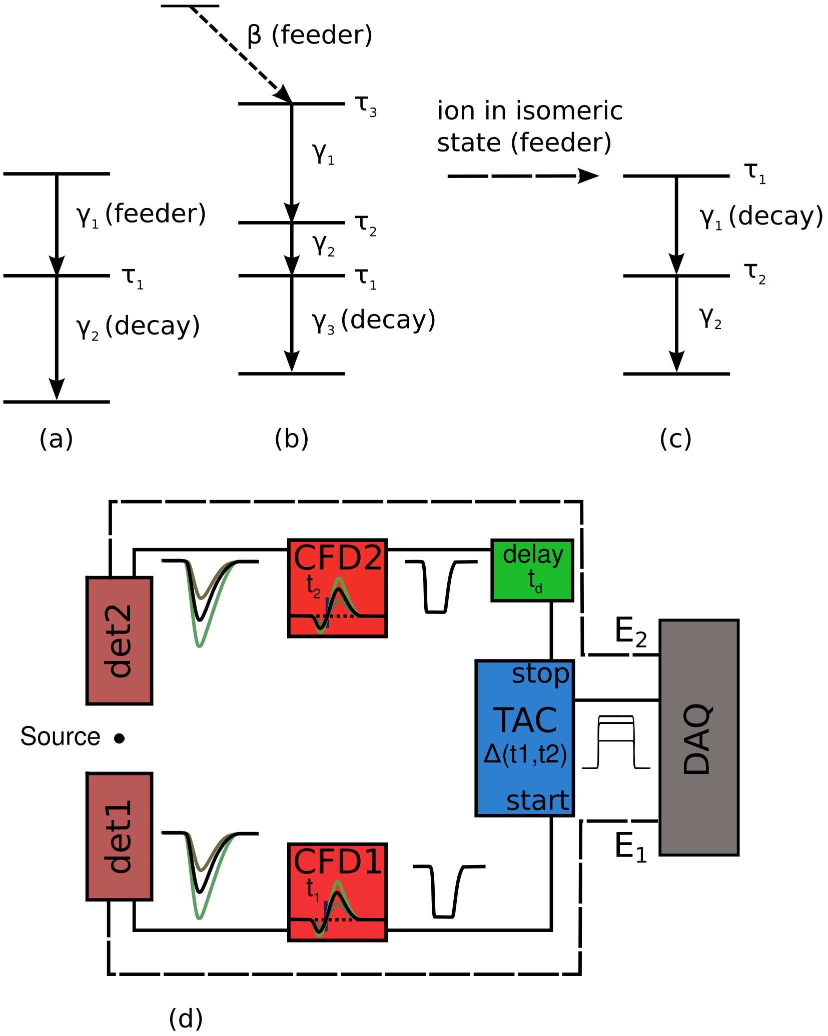

Figure 2.1: (a,b,c) Possible decay - feeder cascades for delayed coincidence measurement of a lifetime τ_1 of an excited nuclear state. Shown are cascades for direct $\gamma\gamma$ fast timing (a), $\beta\gamma\gamma$ timing (b), and ion-γ timing (c). Possible side feeding in (b) and (c) is not shown. (d) A simple fast timing setup for two detectors.

time distribution using one of several analysis methods, which are described in Section 2.1.3.

One important characteristic of a fast timing setup is its prompt response function (PRF) $P(f)$. Two coincident signals are called prompt, if their time difference cannot be resolved with the experimental setup used to measure them. This is always true for real prompt events, like the emission of 511 keV electron-positron annihilation radiation. Depending on the setup, delayed events below a certain limit cannot be distinguished from prompt events. In a typical fast timing experiment with LaBr detectors (see below) events with a mean delay of 5 ps can be considered prompt. The time spectrum of such prompt coincident events is the PRF of the timing setup. Its position in the time spectrum is defined by a constant offset (delay) and any existing time walk. $P(t)$ can often be approximated by a Gaussian distribution if scintillation detectors are used. A delayed coincidence from a cascade with a lifetime larger than the full width at half maximum (FWHM) of the PRF shows an asymmetric time spectrum, with a slope that corresponds to the mean lifetime. Due to the finite width of the PRF, the radioactive decay law shows itself as a convolution of the exponential decay distribution and the prompt response function

$$D(t) = \lambda N_0 \int_{-\infty}^{t} P(t')\ e^{-\lambda(t-t')} \mathrm{d}t'. \tag{2.1}$$

2.1.2 LaBr$_3$(Ce) scintillator detectors

In recent years the use of cerium doped lanthanum-tribromide LaBr$_3$(Ce) scintillation detectors (from now on simply called LaBr detectors) has been established for $\gamma\ \gamma$ delayed coincidence measurements in nuclear physics experiments. They are very well suited for the task as they have very good timing characteristics combined with good energy resolution. The latter is important for direct γ-γ fast timing. Apart from the obvious fact, that a narrower peak guarantees better energy selection in order to get clean coincidences, a better energy resolution also means a better peak-to-background ratio compared to detectors with worse resolution. Background contributions are very important for lifetime extraction from time difference spectra, especially if the centroid shift method is used (see next Section 2.1.4).

As scintillation detectors, LaBr-detectors consist of the scintillation crystal, a photo multiplier tube (PMT), and a base, where the signal cables and the high voltage supply can be connected to. An optical clear adhesive is used to connect the crystal to the top of the PMT. All components are usually packed into a metal tube in a lightproof way. The detectors need no cooling, and are easy to handle. The specifics of the detectors used in the ^{99}Y and ^{100}Nb experiments are given in Chapter 3.3.

LaBr$_3$(Ce) as a scintillation crystal has one of the highest output luminosities of all known scintillators [49]. Relevant for timing are the two scintillating states, which have different decay times τ. One short-lived one, τ_{fast}, which is responsible for the good timing qualities, and one long lived one, τ_{slow}. For LaBr$_3$(Ce), $\tau_{\text{fast}} = 15 - 26$ ns and $\tau_{\text{slow}} = 66$ ns [49].

The time resolution of a delayed coincidence setup is proportional to the full width at half maximum (FWHM) of the prompt response function (PRF) $P(t)$, introduced in Section 2.1.1. The main contributing factors to the resolution δt are the size and material of the scintillator, the electron time spread in the PMT, the electronic time pick off by the CFD and the setup geometry, including a finite size of the γ ray source (cf. [49] and [50]).

$$\delta t = \frac{FWHM}{\sqrt{2}} \approx \sqrt{\sigma_{\text{sc}}^2 + \sigma_{\text{PMT}}^2 + \sigma_{\text{CFD}}^2 + \sigma_{\text{geom}}^2}\ .$$

The time resolution is especially important if the slope method is applied (see Section 2.1.1) as it determines the part of the time spectrum that can be used for fitting. This can have a huge impact on needed statistics. For the centroid shift method it is of lesser importance. This is due to the fact that the centroid of a distribution can be determined with high accuracy, even for a broad distribution. That is why an improvement of some percent in time resolution does not bring as big an improvement in precision of timing results as one might be tempted to think. This is also the reason why in the planned new LaBr arrays, larger crystals are often preferred over smaller ones. The smaller crystals bring a better time resolution, but the superior full energy peak efficiency of the larger crystals brings a greater advantage for fast timing measurements, as peak-to-background ratio improves - in the low energy regime.

2.1.3 Analysis of time spectra

Let us assume the two transitions γ_1 and γ_2 in Figure 2.1 (a) are not in prompt, but in delayed coincidence. Detector 1 starts the TAC (start) and is gated on transition γ_1 with energy E_1 which feeds the state of interest (feeder), while detector 2 is gated on the decay transition γ_2 (decay), with energy E_2, and stops the TAC (stop). The lifetime of the state shows itself in the time spectrum as a pronounced asymmetry with a tail on the right flank. This tail is commonly called the slope. It consists of events which are measurably delayed with respect to the position of two prompt events. If the gates on the two detectors are now switched - decay on start and feeder on stop, the slope is on the left hand side. This terminology of decay, feeder, start and stop will be used throughout this thesis.

Slope fit method

If the lifetime τ is larger than the time resolution of the fast timing setup, i.e. the FWHM of the PRF, the time distribution becomes asymmetric and a pronounced tail is visible, which corresponds to the exponential decay, according to the radioactive decay law (see equation (1.1)). The lifetime can then be determined by measuring the slope of the delayed time distribution D(t),

$$ln\,[D(t)] \sim -\lambda t,$$

where $\lambda = 1/\tau$ is the decay constant. This method is applicable, if there are enough data points in the region where $\frac{P(t)}{D(t)} \ll 1$.

Convolution fit method

If the time distribution is asymmetric, but the conditions for the slope method are not met, then the lifetime can be extracted by a fit of the convolution given in equation (2.1) to the time distribution. In order to calculate the convolution, the shape of the PRF has to be known. In the case of an approximately Gaussian prompt distribution, the convolution has the following form:

$$D(t) = \frac{N_0}{2\tau}\, e^{\frac{\sigma^2}{2\tau^2} - \frac{t-t_0}{\tau}}\ \mathrm{erfc}\left(\frac{\sigma}{\sqrt{2}\tau} - \frac{t-t_0}{\sqrt{2}\sigma}\right), \tag{2.2}$$

where t_0 is the position of the maximum of the PRF, σ its width and erfc() the Gauss complementary error function. This method has the advantage that the statistics of the full distribution can be used for the fit. However, the fit function has four parameters, opposed to only two in the case a slope fit (ignoring a constant background), with a much more complicated fit function. This makes the application of a least square fit a somewhat dangerous endeavour, as the residuum function generally has more than one minimum. This is especially the case for long lifetimes with low statistics in a large part of the slope, where the least square fit underestimates the lifetime, as remarked in [50]. In this case a fit with a maximum likelihood algorithm is superior. Furthermore the condition of a known PRF shape, let alone that of a Gaussian one, is not always fulfilled in real fast timing experiments. Still, for lifetimes not much shorter than the time resolution, this method often yields results consistent with other methods. This is demonstrated in [50] and also in Section 3.3 and 3.4 of this work.

Centroid shift method

The determination of lifetimes from a time difference distribution $F(t)$ using the method of moment analysis was first proposed by Bay [51] in 1950. It was then extensively used in β-γ-γ experiments [50] and has recently experienced a renaissance in combination with the advent of larger arrays of ultra fast LaBr scintillator detectors, like the ROBALL at NIPNE, Romania, the EXILL fast timing arrays in a campaign at the ILL early in 2013 and the planned FATIMA array.

Most commonly the first moment, the centroid $C(F(t))$, of the time distribution is used for lifetime determination. It is defined as

$$C(F) = \frac{\int tF(t)}{\int F(t)}, \quad \text{which simplifies to} \quad C(F) = \frac{\sum (tF(t))}{\sum (F(t))}$$

in the case of a discrete spectrum. Considering that a delayed time distribution $D(t)$ is the convolution of the decay part with lifetime τ and the PRF of the setup, $P(t)$, the following simple relation is true [51]:

$$\tau = C(D) - C(P). \tag{2.3}$$

The lifetime τ can be determined by measuring the centroid of the delayed and prompt time distribution. $C(D)$ can be measured with high accuracy for two coincident transitions. The corresponding prompt centroid position has to be determined in a calibration measurement, because it is energy dependent.

Bay already remarked in [51], that the method is applicable “under the most general circumstances”. He had in mind the determination of lifetimes from time distributions which include several decay constants, as they are encountered when measuring the time difference between two signals with several intermediate states of different lifetimes. In this case the centroid shift method leads to the following relation between the intermediate lifetimes τ_i and the *mean lifetime* Θ, determined from equation (2.3):

$$\Theta = \sum_i \tau_i \ .$$

This relation is simple, especially compared to the complicated time distribution shapes following for multi state cascades from the Bateman equations ([52]). It is exploited in the β-γ-γ method for cascades like the one shown in Figure 2.1 (b). Another huge advantage of this validity under "most general circumstances" is that these also include background contributions to the centroid. This is discussed in more detail in Section 2.1.5.

A refinement of the centroid shift method is the *mirror symmetric centroid difference method* (MSCD), introduced by Régis [49] in 2011. This method is more robust towards systematic uncertainties, like, e.g., TAC drifts. It can also be generalised to make lifetime measurements with a large number of timing detectors easier and more precise at the same time [53]. The specifics of this *generalised centroid difference method* (GCD) are reviewed in the next Section.

2.1.4 The generalised centroid difference method

The prompt curve calibration is the main problem of the centroid shift method. A two detector system has a combined time walk, dependent on the energy of both gates. That is why it can be argued that, until recently, the most successful and fruitful application was in β-γ-γ experiments [50, 54]. In these experiments, the gate on the β energy is the same for all measurements, and thus a very exact calibration can be accomplished. In $\gamma\ \gamma$ experiments however, the energy gates of the two detectors change, depending on the state whose lifetime is to be measured. This combined energy dependent time walk is non-linear and asymmetric [55]. It turns out that a measurement of the difference ΔC of the two centroids $C(D_{\text{stop}})$ and $C(D_{\text{start}})$ has several advantages. These are exploited in the mirror symmetric centroid difference method [55] and its extension for multi detector systems, the generalised centroid difference method [53]. Both are briefly described below, based primarily on these two references. Notation is mainly adopted from [49].

To describe the basics of the MSCD method, we assume a fast timing setup like it is shown in Figure 2.1(d) and a $\gamma\ \gamma$ cascade as it is depicted in Figure 2.1(a). A time distribution D_{stop} is obtained if the stop detector is gated on the decay transition with energy E_{decay} and the start detector is gated on the feeding transition with energy E_{feeder}. For a long lifetime, this means a slope on the right hand side. D_{start} denotes the reverse case, in which the stop detector is gated on the feeding transition and the start detector on the decay. In this case the slope appears on the left hand side. The following formulae lay out some nomenclature definitions, which are very important to grasp the principle of the method. They can be confusing when encountered for the first time. Attention is called to the introduction of the concept of a reference transition. The centroid difference depends on the energies of the two gates and on the fact which gate is a feeder or decay transition. The choice of a reference transition fixes the character (feeder or decay) and the energy E_{ref} of one gate. For convenience the following shorthands are defined for the definitions of the two centroids defined above:

$$C(D_{\text{stop}}) = C(E_{\text{start}})_{E_{\text{ref}}\ \text{on stop}} = C(E_\gamma)_{\text{stop}},$$

with the reference transition gated on the stop branch and

$$C(D_{\text{start}}) = C(E_{\text{stop}})_{E_{\text{ref}}\ \text{on start}} = C(E_\gamma)_{\text{start}},$$

with the reference on the start branch. The centroid difference for a reference transition (either decay or feeder) with energy E_ref and a corresponding given other transition at energy E_γ is then defined as

$$\Delta C(E_\gamma)_\text{decay} = C(E_\gamma)_\text{stop} - C(E_\gamma)_\text{start}$$

$$\Delta C(E_\gamma)_\text{feeder} = C(E_\gamma)_\text{start} - C(E_\gamma)_\text{stop} \ .$$

With the definition $\Delta E = E_\text{feeder} - E_\text{decay}$, the following symmetry between the choice of a feeder or decay as reference can be found [55]:

$$\Delta C(\Delta E)_\text{decay} = -\Delta C(-\Delta E)_\text{feeder} \ .$$

This relation is responsible for the name *mirror symmetric* centroid difference method.

The centroid difference $\Delta C(E)_\text{ref}$ of a prompt coincidence is the prompt response difference $\text{PRD}(E)_\text{ref}$ for a reference transition with energy E_ref. Applying equation (2.3), the following relation between lifetime and centroid shift is true for a delayed cascade connecting a level with lifetime τ:

$$2\tau = \Delta C(E_\text{feeder})_\text{decay} - \text{PRD}(E_\text{feeder})_\text{decay}, \tag{2.4}$$

$$2\tau = \Delta C(E_\text{decay})_\text{feeder} - \text{PRD}(E_\text{decay})_\text{feeder}. \tag{2.5}$$

The PRD depends on the reference energy. PRDs corresponding to different reference energies are shifted in parallel by a constant time offset $s(E_\text{ref1}, E_\text{ref2})$. Analogous to the promt curve of the original centroid shift method, the PRD has to be calibrated to extract lifetimes from the time spectra. It has been shown, that the ^{152}Eu soure is very well suited for this purpose [49]. Note that, by definition, $\Delta C(E_\text{feeder})_\text{decay} = \Delta C(E_\text{decay})_\text{feeder} = 0$ for prompt transitions with $E_\text{decay} = E_\text{feeder}$, which serves as an additional calibration point [55]. It can be used to determine the shift $s(E_\text{ref1}, E_\text{ref2})$. To fit the PRD, the function

$$PRD(E_\gamma)_\text{ref} = \frac{a}{\sqrt{b + E_\gamma}} + cE_\gamma + d, \tag{2.6}$$

as proposed in [55], is used. Note that the first term on the right side of this formula can be related to the time walk behaviour expected from a CFD [49]. A plot of a PRD fit using this function can be seen in Figure 3.10. The PRD calibration has to be performed using full energy peaks from prompt cascades. It was demonstrated, that the use of coincident Compton events, e.g. from a ^{60}Co source, is not adequate for high precision measurements as the Compton continuum itself has a complicated time structure [49]. This effect becomes more pronounced with increasing crystal size.

The MSCD method shows its full potential in the application with large fast timing arrays. To this point, the discussion in this Section was restricted to systems comprised of two detectors and one TAC. If the number of detectors N is increased, the number of possible combinations for coincident measurements grows like $\frac{N(N-1)}{2}$. With six detectors there are already 15 combinations. In the EXILL fast timing campaign, conducted at the ILL in spring 2013, 16 detectors were used which already amounts

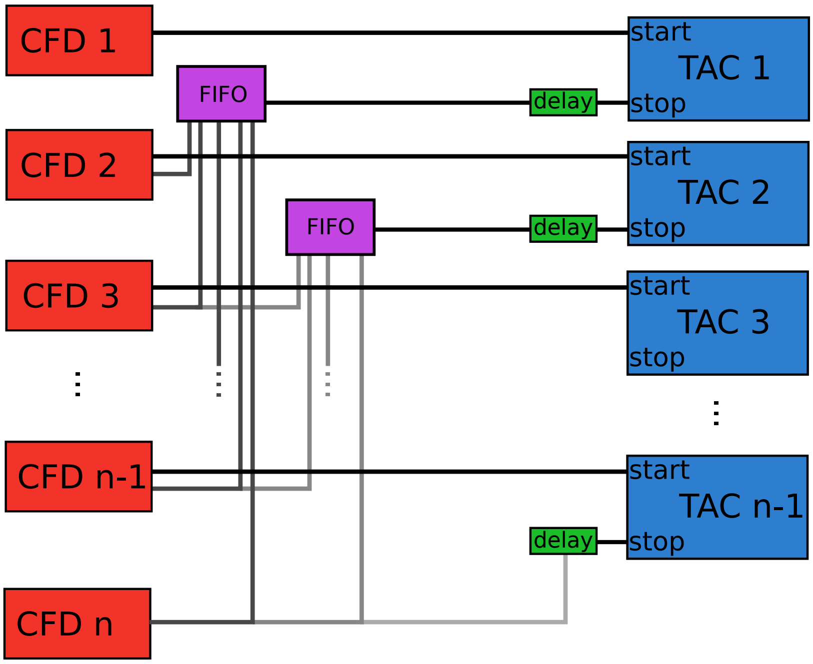

Figure 2.2: *Common stop* timing circuit for n detectors with $(n-1)$ TACs. Each TAC is startet by an individual detector and stopped by detectors with higher index numbers. All $N(N-1)/2$ detector-detector combinations are measured with $n-1$ TACs. Fan in-Fan outs (FIFOs) are used to generate the the common stop.

to 120 combinations[2]. A number which renders analysis in the way described above tedious. A very elegant, simple and precise way to evaluate fast timing data from such experiments was recently introduced by Régis *et al.* with the *generalised centroid difference* (GCD) method. In [53] it is shown that, instead of $\frac{N(N-1)}{2}$ PRD functions, a mean PRD curve can be determined by evaluating the centroid of the sum of all combinations. Lifetimes are then determined from the shift of the mean centroid difference with respect to this mean PRD, using equation (2.4). In the same work it is also shown that precision measurements down to 5 ps are possible with this method.

To measure all $\frac{N(N-1)}{2}$ possible combinations, it is not necessary to use the same number of TACs. All combinations can be measured with a common stop fast timing circuit. A schematic diagram of such a setup is shown in Figure 2.2 (a). The detectors and TACs are labelled from 0 to N. Detector i starts TAC i, which in turn is stopped by all detectors with index number $j > i$. This way, all combinations are recorded with $N-1$ TACs. The common stop setup is favoured over the common start to reduce dead time. Once a signal is detected at the start input of the TAC, no further start signals are accepted for the duration of the TAC range. The TAC range is usually set to 50-100 ns to measure picosecond lifetimes in fast timing experiments using LaBr detectors.

---

[2] This is the maximum possible number of combinations. In the analysis 24 combinations had to be excluded, due to heavy contaminations from cross talk events.

2.1.5 Considerations about the measurement uncertainty

The main contribution to the measurement uncertainty using the GCD method comes from systematic uncertainties and their correction. The uncertainty of the time calibration of the TAC can be done very precisely ($< 0.5ps$) and can be neglected in most cases. With reasonable statistics the centroid of the delayed distribution itself can often be measured with a precision below 1%. The calibration of the PRD introduces an uncertainty of typically 5 ps on the mean lifetime.

In delayed γ γ coincidence measurements, the largest contribution to the measurement uncertainty, however, is due to timing background corrections. If coincidences are sorted, the gate usually contains background events on top of the desired full energy peak events. Few of these background events are truly random with respect to the events in the coincidence gate of the other detector. Compton and multiple compton events from coincident transitions with higher energy are the main source of delayed time background in the energy region above 300 keV. Below 300 keV, the background is heavily delayed towards prompt full energy transitions. Here the background mainly consists of compton events, back scatter events, and heavily delayed scattered γ rays from the surroundings, including time correlated cross talk events from neighbouring detectors.

If the peak to background ratio is close to ten or larger, the contribution of the background to the true full energy centroid can be neglected [49]. However, for smaller peak to background ratios, a correction has to be applied. In these cases, the contribution from the background to the time distribution, yielded by gating on the full energy peak, is larger than 1 ps and can no longer be neglected in the determination of the lifetime [53]. A correction has to be applied. The background contribution C_{bg} to the measured total centroid C_{tot} is determined by gating on a transition and then setting gates in the background around the corresponding coincident transition. This way the background contribution can be interpolated. By determining the peak to background ratio $\beta = \dfrac{\text{Vol}_{\text{fep}}}{\text{Vol}_{\text{bg}}}$ in the gate limits of the coincident transition, the value of the full energy peak centroid C_{fep} can then be determined:

$$C_{\text{fep}} = C_{\text{tot}} + \beta(C_{\text{tot}} - C_{\text{bg}}) \ , \tag{2.7}$$

which brings a value of

$$\Delta C_{\text{fep}} = \frac{1}{2}\sqrt{(1+\beta)^2(\Delta C_{\text{tot}})^2 + \beta(\Delta C_{\text{bg}})^2} \tag{2.8}$$

into the uncertainty of the final mean lifetime τ, neglecting the uncertainty of β.

Time-correlated background is the biggest problem for lifetime measurements involving transitions below 300 keV. It has been demonstrated, that active and passive shielding is very efficient in this kind of experiments [49].

2.2 Spectroscopy of exotic nuclei

The nuclei investigated within the scope of this thesis are situated in the proton mid-shell region between the magic numbers Z=28 and Z=50 and close to neutron number

N=60 (see Figure 1.2). This means, all these nuclei are exotic and neutron rich. Over the past decade exotic nuclei have become more and more a focus of nuclear structure research. With the development and extension of experiments such as (REX-)ISOLDE, RIKEN, the construction-in-progress FAIR-facility and many similar sites around the world, great efforts are undertaken to investigate nuclear structure far from β-stability. While non-stable nuclei close to stability can be produced at relatively low energies in direct ion-beam reactions[3], exotic nuclei demand other production methods. Exotic proton rich nuclei are accessible through fusion evaporation reactions. In this type of reaction a new nucleus is formed by a fusion reaction of two lighter nuclei, which are typically stable. Directly after the fusion process, the compound is highly excited, resulting in emission of neutrons and protons. As the proton-neutron-ratio N_π/N_ν decreases going from light to heavy masses, fusion of two nuclei results in a proton rich product, situated east of the valley of stability in Figure 1.2. These reactions can be induced with ion beam accelerators, a well established tool of nuclear physics since its early times, like, e.g., the Cologne Van-der-Graaf Tandem accelerator. Exotic neutron-rich nuclei, east of the valley of stability, are not accessible through this technique. Historically, exotic neutron-rich nuclei have first been investigated by observing fission products. The discovery of nuclear fission by Otto Hahn, Lise Meitner *et al.* [56, 57] can be considered the beginning of these studies. An introduction to nuclear fission as a tool for experimental nuclear structure physics is given in Section 2.2.1. Another way to produce very exotic nuclei (proton- and neutron-rich) is nuclear fragmentation, a type of nuclear reaction, which is not discussed further here. These two kinds of reactions have in common, that they are not particularly selective concerning their production channel. Thus it is necessary to select and identify the isotope of interest. This can be achieved using different methods. One of these is fragment separation using electric and magnetic fields. This method is applied at the Lohengrin mass spectrometer, which is described in Section 2.2.2 below. Another aspect of experiments with exotic nuclei is

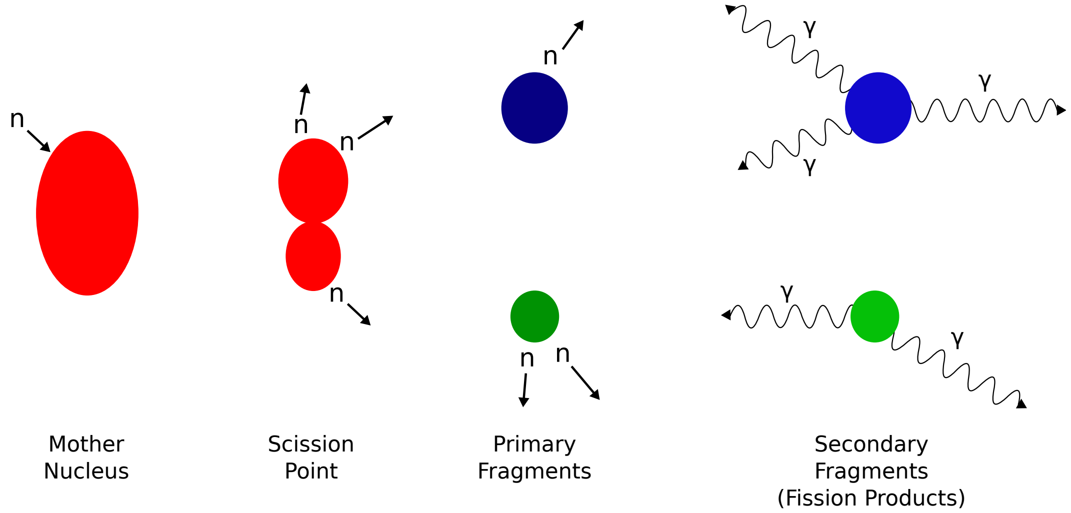

Figure 2.3: Stages of binary fission.

---

[3] Neutron capture reactions have to be included here.

the signal to noise ratio, which is typically much lower than in non-exotic experiments. All this demands for sophisticated experimental setups. The Lohengrin separator at the ILL[4] is one of the setups designed with the intent to meet these challenges.

2.2.1 Nuclear fission and its application as a production method for radioactive nuclei

The process of nuclear fission was discovered by Hahn and Strassmann [56]. The process itself is very complex and far from well understood. It is still subject of fundamental nuclear structure research. A detailed review is beyond the scope of this thesis and only a superficial phenomenological description will be given in this section. Reviews on the topic can be found, e.g., in [58].

Nuclear fission is observed in heavy nuclei. In the picture of the liquid drop model, fission can be interpreted as a process where the nucleus is elongated and, at a certain elongation, scissions into two parts (see Figure 2.3). This process happens spontaneously in some actinide nuclei. In these nuclei, the surface tension energy of the large deformation preceding fission is compensated by the coulomb repulsion of the protons. The energy barrier for fission is small in these nuclei. The cross section for fission increases if the nucleus is excited, for example after the capture of a neutron. The different stages of the process are schematically depicted in Figure 2.3. Fission of a nucleus ${}^{A}_{Z}X_{N}$ produces two (binary fission) or more (ternary and higher order fission) lighter nuclei in highly excited states, as well as typically 2-3 neutrons. The following description will be limited to binary fission, which is by far the most likely reaction channel. The primary fission fragments are emitted in opposite directions. They emit neutrons until nucleon emission is no longer favored energetically. The products are then called secondary fission fragments. Nuclear fission is asymmetric with respect to the mass of the fission fragments, yielding one light and one heavy product nucleus per fission. These two are called fission partners.

Mass yields for neutron induced fission of ^{233}U, ^{235}U, ^{241}Pu, and ^{241}Am are shown in Figure 2.4. The two so called *humps* correspond to the light and heavy fission partners, with maxima around A = 90 and A = 130 respectively. Note that with increasing mass of the fissioning nucleus, the *hump* of light nuclei travels to larger masses, while that of the heavy fragments does remain fairly constant. This fact, and asymmetric fission itself, can be understood qualitatively in terms of the shell model. At the moment close to fission, the structure of the two parts resembles more and more that of the individual product nuclei. For these, the shell structure favores energetically nuclei with a doubly magic character. For symmetric fission of the actinides, the closest doubly magic configuration is ^{132}Sn. If one part is close to, but below this number, it will bind more nucleons until it is slightly heavier than ^{132}Sn. The remaining nucleons then make up the lighter fragment. This mechanism for forming the heavier fragment is the same for fission of all nuclei in the actinide region, and thus the mass yield distribution of the heavy fragments is also similar.

---

[4] Institute Laue-Langevin. The ILL nuclear reactor is one of the strongest neutron sources for scientific use world wide. www.ill.eu

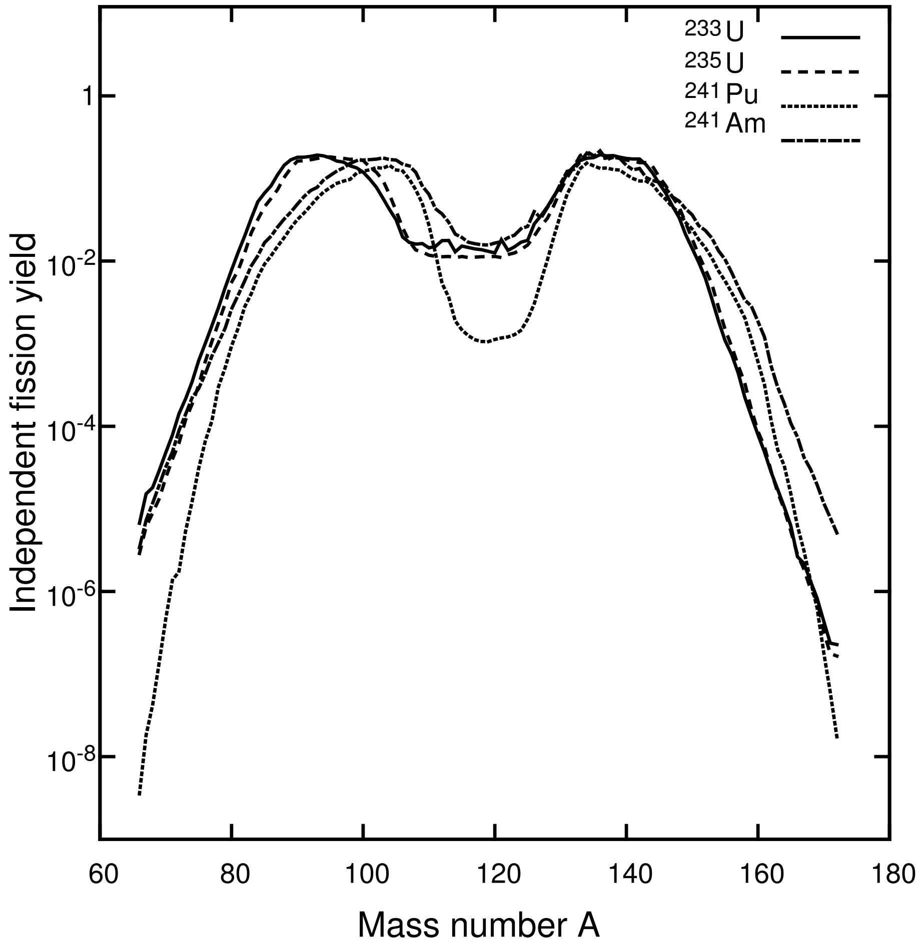

Figure 2.4: Independent mass yields after fission induced by thermal neutrons for the fission targets ^{233}U, ^{235}U, ^{241}Pu, and ^{241}Am according to the database ENDF/B-VII.1 [59].

Fission releases about 200 MeV of energy, which is distributed among the two fragments and emitted neutrons. The kinetic energy E_{kin} of the heavy fragments is smaller than that of the light ones. Typically $E_{\mathrm{kin}} \approx 70-90$ MeV and $E_{\mathrm{kin}} \approx 80-100$ MeV.

The neutron excess of stable nuclei increases with increasing mass number. Fission of a heavy nucleus therefore results in two nuclei, which have a larger neutron excess than their corresponding stable isobars; the products are exotic. This fact makes fission interesting for the experimental study of neutron-rich nuclei. As fission produces a whole range of nuclei with similar probability, measurements of particular isotopes demand for techniques to select the the fission fragments based on their mass A and nuclear charge Z. One possibility to achieve this is fragment separation with electric and magnetic fields. The Lohengrin separator, described in the following section, applies exactly this technique.

2.2.2 The Lohengrin mass separator

The Lohengrin mass spectrometer [60] for separation of fission fragments is installed in the reactor hall at the Institute Laue Langevin (ILL) in Grenoble, France. Figure 2.5 shows a schematic depiction of the setup. A photograph of the separator, without the radiation protection walls usually surrounding the beam tube, is shown in Figure 2.6. The fragments are produced after a fission reaction, induced by thermal neutrons, in a target situated close to the core of the ILL nuclear research reactor. At this point the neutron flux is $5 \cdot 10^{14} \frac{1}{\mathrm{cm}^2\mathrm{s}}$. The fission targets have a typical thickness of 200-400 μg/cm^2. A collimator is positioned close to the target which selects fragments emitted in the direction of the Lohengrin beam tube, essentially creating a beam of the ion cocktail of fission fragments which have various kinetic energies E_{kin}, masses A, and ionic charges q. Isotope, energy and mass distribution after fission were discussed in Section 2.2.1. The ions are not fully ionized but have a statistically distributed ionic charge after passing a thin layer of nickel (few tenth of a μm), directly after they leave the target. The mean ionic charge lies between $q = 19$ and $q = 21$ for the light fragments. The typical energy of the fragments is of the order of $E = 100$ MeV, which corresponds to about 1 MeV per nucleon.

Separation of the fission fragments is accomplished by the combination of a magnetic and an electric field, produced by the main magnet and the condenser[5] (see Figure 2.5). The fission fragments are split onto different parabolas, according to the ratio of their mass and energy to ionic charge, A/q and E_{kin}/q. Fragments with the selected ratios first pass the magnetic field $\mathcal{B}$ which is constant and perpendicular to the ions' momentum. The ions are deflected in the horizontal x-direction. After that they pass the condenser, which is shaped so that selected ions travel along a circular line of equal electric field strength $\mathcal{E}$. Here deflection happens in the vertical y-direction. The movement of ions with charge q, mass A, velocity v in these fields follows the equations

$$q v \mathcal{B} = \frac{A v^2}{r_{\mathrm{mag}}} \tag{2.9}$$

$$q \mathcal{E} = \frac{A v^2}{r_{\mathrm{con}}}. \tag{2.10}$$

Here r_{mag} and r_{con} are the radii of curvature of the circular trajectory on which the ions are forced by the main magnet and the condenser respectively. $\mathcal{E}$ and $\mathcal{B}$ are adjusted in a way, that A, q and E_{kin} of the desired fragments correspond to the radii of curvature that allow a passing of the whole spectrometer. By dividing equation (2.9) by equation (2.10), one arrives at an expression for the velocity

$$v = \frac{r_{\mathrm{con}}}{r_{\mathrm{mag}}} \frac{\mathcal{E}}{\mathcal{B}}.$$

The kinetic energy of the fission fragments is smaller than 1 MeV per nucleon, which is much smaller than the rest energy of a nucleon, $E_{\mathrm{rest}} \approx 1$ GeV. Then a non-relativistic

---

[5] The old English word *condenser* for capacitor still sticks to this particular one.

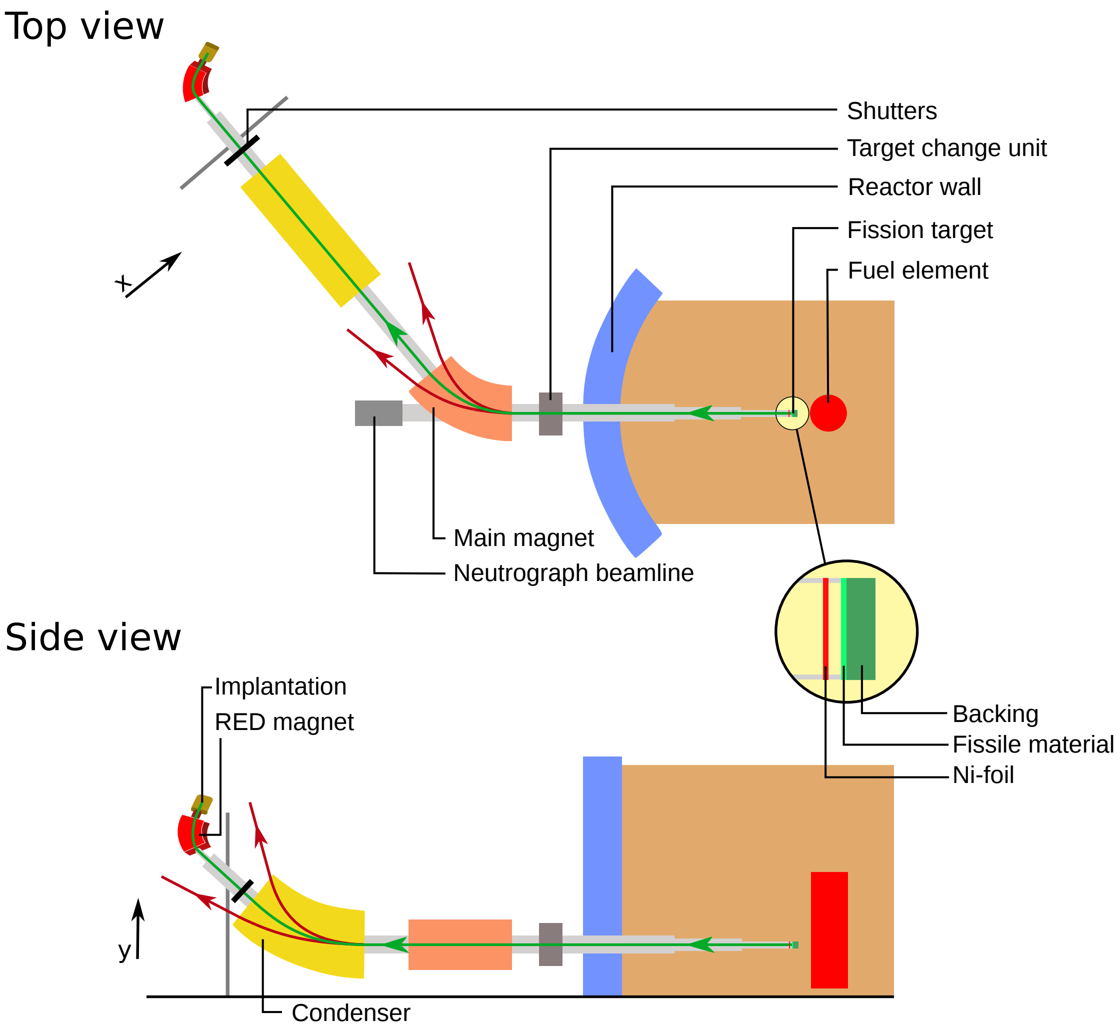

Figure 2.5: Schematic drawing of the Lohengrin mass spectrometer, based on a figure on the ILL website[61] and the author's own observations. The top view shows the deflection in x-direction induced by the main magnet. The side view shows the deflection in the y-direction by the condenser. The green line depicts the path of focused fission fragments that reach the ionization chamber, where they are stopped. The path length for these ions is 23.15 m.

treatment is sufficient and the relation

$$E_{\text{kin}} = \frac{A}{2} v^2$$

holds. The electric field of a plate capacitor is

$$\mathcal{E} = U/d,$$

where d is the distance between the plates, and U is the electrostatic potential. By

Figure 2.6: Photograph of the Lohengrin mass spectrometer without the radiation protection usually surrounding it. The condenser (a) and the main magnet (b) can be seen. Picture taken from [62].

combining these equations, the following focusing conditions are derived:

$$\frac{A}{q} = \frac{1}{\chi}\frac{\mathcal{B}^2}{U} \tag{2.11}$$

$$\frac{E}{q} = \phi U, \tag{2.12}$$

with the two spectrometer parameters

$$\phi = \frac{r_{\mathrm{con}}}{2d}, \quad \chi = \frac{2\phi}{r_{\mathrm{mag}}^2}. \tag{2.13}$$

Two general types of decay spectroscopy experiments are performed at Lohengrin, namely β decay studies and μs isomer spectroscopy. All experiments presented in this thesis are μs isomer experiments at Lohengrin. To determine whether an experiment on a certain nucleus is feasible at Lohengrin, the following points have to be considered:

- the fission yield of the mass of interest,
- the independent fission yield of the isotope of interest,
- the energy distribution of the fission fragments,
- the isotopes‘ charge state distribution after crossing the Ni foil,
- contaminations by nuclei with similar A/q and E/q in the same mass region,

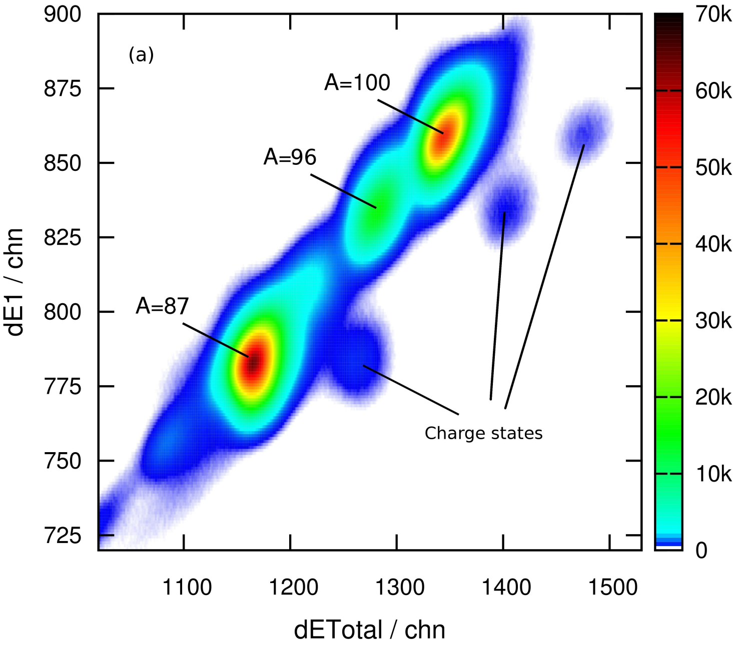

Figure 2.7: (a) Plot of the energy loss in the first part of the ionization chamber, ΔE_1, against the total fragment energy $E_{\text{total}} = \Delta E_1 + \Delta E_2$, for the setting A = 87, q = 20, E = 88. Apart from mass A = 87, fragments with mass A = 96 and mass A = 100 are also detected.

- the fission yield of these contaminants, and
- the known isomers and β decays.

The first points mainly influence the choice of fission target. As can be seen from Figure 2.4, the mass distribution of fission fragments strongly depends on the fission target material. Mass yields can vary over several orders of magnitude, most notably in the mass region between the humps and on the edges. It can be argued that it is of advantage to choose a target, where the desired mass is situated close to this edge of the distribution, because in this way the yield of possible contaminents decreases quickly in one direction, leading to a potentially cleaner measurement.

Another aspect is the fine tuning of the separator in order to achieve a clean and strong signal of the desired isotope. After each major setup change and after each target change, a calibration scan of B_{main} is performed with a strongly produced mass, to adjust the parameter χ. Figure 2.8 shows such a scan. After the scan, the old χ value is changed so that the maximum of the distribution lies at the correct value. Then the Lohengrin spectrometer is set up for separation of the desired mass. To find a setting, as a first step, coarse estimates for the field values are calculated for the isotope of interest. If there is no estimate for q from earlier measurements, a q-value of 21 is chosen as a starting point. For a clean setting it is desired to get as few ions as possible from neighboring masses with similar A/q and E/q values (see equations (2.11) and (2.12)). This can be influenced by the number of shutters opened behind the focal plane. Of course, a wide open collimator means more ions, but also more background.

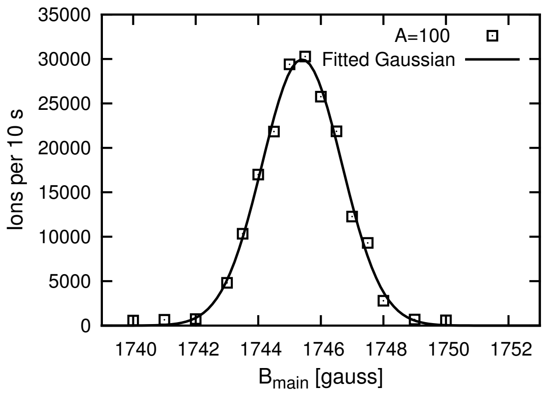

Figure 2.8: Calibration scan with the ionization chamber. At different magnetic fields B_{main} of the main magnet, the number of ions with mass A = 100, atomic charge q = 20 and energy E = 94 was measured for ten seconds to determine the optimal value of the instrument parameter χ (see equation (2.13)). A fitted Gaussian distribution is also shown.

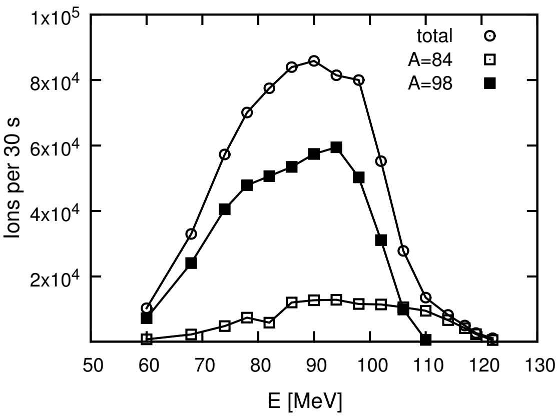

Figure 2.9: Yield scan with the ionization chamber for different fragment energies. The spectrometer was set for mass A = 98 and ionic charge q = 21. From the scan it follows, that the optimum energy lies at E = 92 MeV.

For isomer spectroscopy experiments, it is especially important, to minimize the overlap of energy-loss distributions of the contaminants in the ΔE_1-ΔE_2 ionization chamber with that of the isotope of interest. That is because mass selection is achieved by gating on the ionization chamber data. The amount of contamination can be estimated by calculating the ionic charge q for the neighboring masses which fulfills the focusing condition of the setting. If the necessary ionic charge has a value right between two integers, the contaminants' transmission is low. Depending on the fission yields, it can still be larger than that of the desired mass. Fine tuning is accomplished by performing measurements with settings corresponding to a series of values for E and q. Figure 2.9 show data from an E scan for mass A = 98, performed during the experiment described in Chapter 4 of this thesis. It can be seen, that the absolute number of ions with A = 98 and ions with A = 84, as well as their ratio, depends on the selected E value. In this way it often has to be decided whether the priority is set on a clean measurement or on a high yield of the desired mass; a kind of trade-off situation every experimentalist encounters sooner or later. A similar weighing has to be done for the relative yields of isotopes of one mass, but here the effect is not as pronounced.

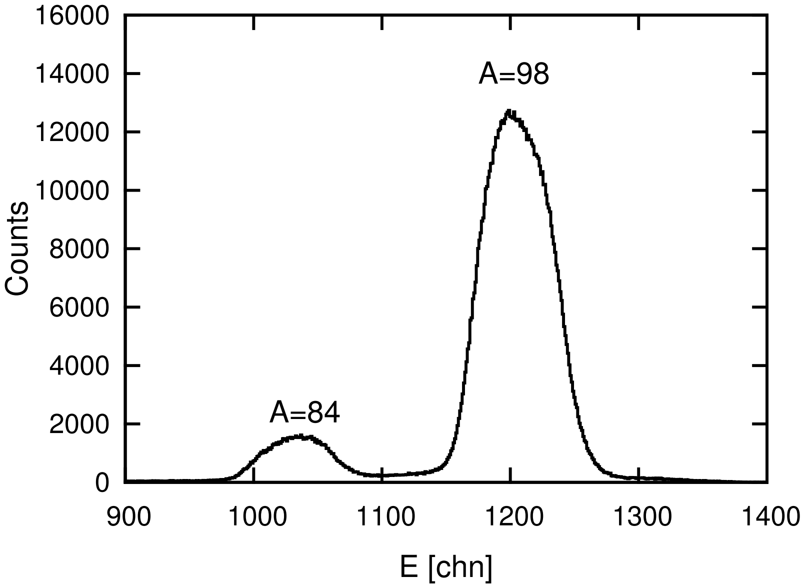

Figure 2.10: Total energy of fission fragments measured with the ionization chamber. Lohengrin was optimized for mass A = 98, with q = 21 and E = 92. Mass A = 84 appears too, but is well separated.

2.2.3 Isomer spectroscopy with the Lohengrin mass separator

If a fission fragment, recoiling from the target, passes the whole spectrometer in an isomeric state, it is possible to directly measure the lifetime of this state via delayed coincidence between the ionization chamber signal and radiation from the isomeric decay. E.g. a γ ray detected by one of the germanium detectors. The data is acquired using digital electronics[6]. The time difference between signals is determined using the synchronized internal clocks of the digitizer modules. The sampling rate of the modules used for experiments within the scope of this thesis is 40 MHz (25 ns between tics). An exponential function plus a constant background is then fitted to the time distribution to deduce the lifetime. The lower limit for lifetime determination using this method is due to the time of flight through the Lohengrin separator, which is about 1.6 μs. For lifetimes shorter than about 0.5 μs impractically long measuring times are needed to get reliable results. An upper limit of between 60 and 80 μs is less clearly defined and mainly governed by the coincidence window and the counting rate. For a given ion rate and a long-lived isomeric state, a larger coincidence window means a higher probability that after implantation of an isomeric ion another ion arrives during the coincidence window but before the first one emits any radiation or vice versa. In this case it is not possible to unambiguously assign the γ signal to a single ionization chamber signal, which eventually leads to time spectra unusable for lifetime analysis.

If several isomers with similar lifetimes are found to be present in cascade in the same isotope, it is advantageous to use γ-γ timing to measure the halflife of those states lower in the cascade, to avoid uncertainties due to feeding corrections.

---

[6] Xia digital gamma finder (DGF) 4C revision E, www.xia.com/Manuals/

The fact that the decay radiation of these μs isomers is in delayed coincidence with the incoming ions allows for a clean spectroscopy of isomeric cascades. This selectivity, in combination with the mass separation capabilities of the Lohengrin setup was employed in many studies of neutron-rich nuclei (e.g., [63–66]). This possibility to apply selection conditions is especially important in experiments with exotic nuclei, as they can improve the signal to background ratio significantly, which is typically very low in this kind of experiments. In γ spectroscopy the delayed transitions can be identified by setting a gating condition on the ion-γ time difference. Additionally, uncorrelated background can be subtracted to retain clean energy spectra and γ-γ coincidences. This isomer selection can also be applied to reduce background in γ-γ fast timing measurements, as was done in the experiments on ^{99}Y and ^{100}Nb, presented in Section 3.3 and 3.4.

In some cases it is also possible to use the ion-γ correlation of delayed transitions to identify the atomic number Z of the nucleus they originate from. The kinetic energy of the ions is too small to achieve complete Z separation with the ΔE_1-E_{total} ionization chamber. However the Z dependence can be measured with the ΔE_1 distribution if a gate on a γ transition from a μs isomer decay cascade can be set. Within the scope of this thesis, this approach was adopted in the case of ^{97}Rb, as it is described in more detail in Section 3.1.

2.3 Electron spectroscopy

Figure 2.11 shows examples of conversion electron spectra. The left spectrum was measured with an *Orange* type magnetic spectrometer, the spectra on the right hand side with a cooled lithium drifted silicon detector. With the magnetic spectrometer, only the electrons are measured, while in the Si(Li) spectrum γ and X rays are also detected. The electrons lines originating from different subshells are clearly visible in both cases. The L-conversion lines are slightly wider than the K-lines, due to their substructure.

The conversion coefficient α contains information on the nuclear transition. As mentioned in Section 1.1, transition multipolarities, can be determined by measuring total or relative internal conversion coefficients. These measurements are intensity measurements of γ and conversion electron transitions.

Conversion coefficient ratios like $\alpha_{\mathrm{K}}/\alpha_{\mathrm{L}}$ can be measured by just comparing the relative intensities of electron peaks in the electron spectrum

$$\frac{\alpha_{\mathrm{K}}}{\alpha_{\mathrm{L}}} = \frac{I_{\mathrm{K}}/I_\gamma}{I_{\mathrm{L}}/I_\gamma} = \frac{I_{\mathrm{K}}}{I_{\mathrm{L}}} \ .$$

A knowledge of relative electron detection efficiency is sufficient. For determination of absolute conversion coefficients, a knowledge of absolute γ and electron intensities is necessary. This was done in the experiment on ^{97}Rb, presented in Section 3.1.

The Si(Li) detector measures electrons as well as γ rays. Due to the proximity and comparably high detection efficiency for electrons of the Si(Li) detector, K-electrons

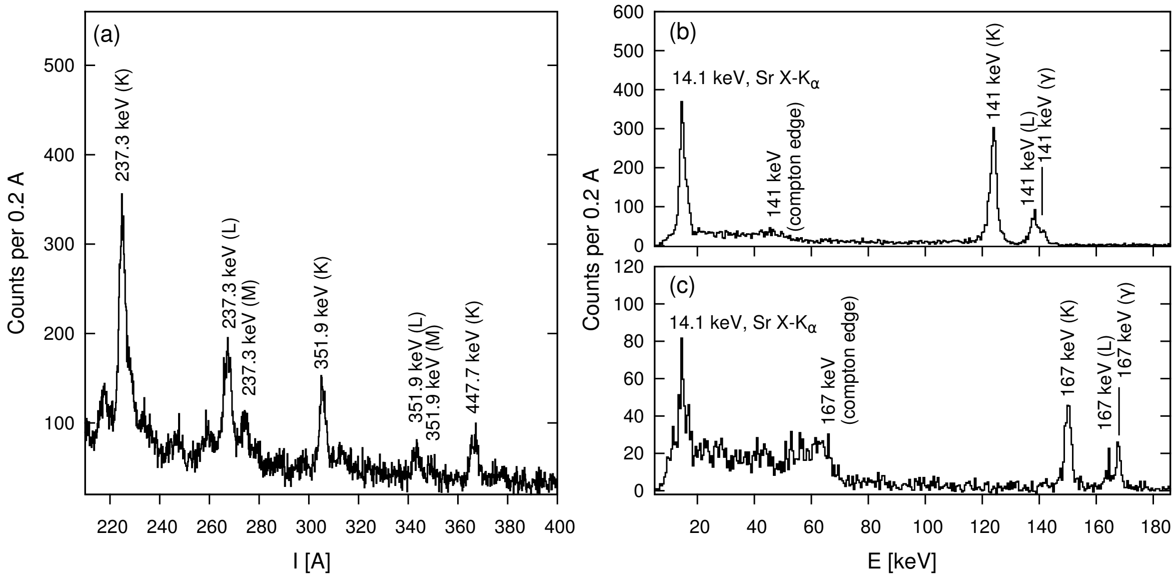

Figure 2.11: Examples of electron spectra. (a) Conversion electron spectrum of ^{178}W, measured with the Cologne Orange spectrometer [67]. The data is from [68]. L and M conversion lines are resolved. On the right hand side two coincidence spectra, measured with a Si(Li) detector, are shown. The transitions are from ^{97}Sr, with data from the experiment discussed in Section 3.2. A germanium detector gate was set on the strong coincident transitions at 167 keV (a) and 141 keV (b). The K X ray line, Compton continuum and the respective γ ray lines are also visible.

are frequently measured in coincidence with K$_\alpha$ and K$_\beta$ X rays. The energies then adds up to the energy of L and M conversion electrons:

$$\left.\begin{array}{rl} E_K = & E_{\text{trans}} - E_{\text{bind}K} \\ E_L = & E_{\text{trans}} - E_{\text{bind}L} \\ E_M = & E_{\text{trans}} - E_{\text{bind}M} \\ E_{K_\alpha \mathrm{X}} = & E_{\text{bind}K} - E_{\text{bind}L} \\ E_{K_\beta \mathrm{X}} = & E_{\text{bind}K} - E_{\text{bind}M} \end{array}\right\} \Rightarrow \left\{\begin{array}{ll} E_K + E_{K_\alpha \mathrm{X}} & = E_L \\ E_K + E_{K_\beta \mathrm{X}} & = E_M\ . \end{array}\right.$$

This has the effect, that the measured K X ray intensity $I_{K_X} = I_{K_X\alpha} + I_{K_X\beta}$ appears to be too small and L and M intensity is too large. The quantitative systematic uncertainty for an internal conversion with transition energy E_γ can be determined from coincidence spectra like the ones shown in Figure 2.11(b,c). The measured intensities I are

$$\begin{array}{lcl} I_{K_\alpha \mathrm{X}} & = & \omega_K N_{K_e} \left(\epsilon_{K_X} - \epsilon_{K_X} \epsilon_e(E_K)\right) \\ I_K & = & N_{K_e} \left(\epsilon_e(E_K) - \epsilon_e(E_K) \epsilon_{K_\mathrm{X}} \omega_K\right) \\ I_L & = & N_{L_e} \left(\epsilon_e(E_L) - \epsilon_e(E_K) \epsilon_{K_\mathrm{X}} \omega_K\right)\ . \end{array} \tag{2.14}$$

N indicates the total numbers of transitions, ϵ are the respective efficiencies. Not every internal K conversion leads to the emission of an X ray. Emission of Auger electrons from the atomic shell is also possible, in a process analogous to that of internal conversion. The fluorescence yield ω_K accounts for this fact. In strontium

$\omega_K = 0.691$ [8]. Based on the efficiency calibration, the magnitude of the correction to the electron intensity for the experiment presented in Section 3.1 is of the order of 10%.

Chapter 3

Experiments and results

In this chapter the performed experiments on the nuclei ^{97}Rb, ^{97}Sr, ^{99}Y, and ^{100}Nb, are described in detail and the results are presented. The data were collected in two experimental campaigns at the Lohengrin mass separator at the ILL, Grenoble, in June 2011 and October 2012. The Lohengrin setup and general information on the experimental and analytic methods applied are discussed in Chapter 2.

In the first campaign, fission fragments with mass A = 97 were investigated. A new 76.5 keV transition from the decay of a previously unknown μs isomer in ^{97}Rb was observed. This is the first information on an excited state in this nucleus. The lifetime of the isomer was determined. The multipolarity of the transition was established by measuring the K conversion coefficient. From the same data, a new decay branch of the 830 keV isomer in ^{97}Sr could be established.

The second experiment presented here was a fast-timing measurement with the aim to investigate collectivity of excited states in ^{99}Y and ^{100}Nb. In these nuclei the lifetime of 4 levels in the isomer decay cascades were determined for the first time. Additionally lifetimes of excited states in the nuclei ^{99}Nb, ^{100}Nb and ^{100}Mo, populated after β decay, were measured.

The results are discussed and compared to theoretical calculations in Chapter 5. The results on ^{97}Rb and ^{97}Sr obtained in this work were published in the journal Physics Review C [69].

3.1 ^{97}Rb

Data, collected in a measuring campaign with the purpose to find new μs isomers in fission fragments in the mass region around A = 90, showed indications of an unknown isomer in a A = 97 nucleus. The results of this campaign are presented in Chapter 4. However, the data did not allow for the identification of the atomic charge Z of the isotope of interest. Furthermore, the lifetime could not be determined with good accuracy due to weak statistics. Mass 97 appeared only as a side product and separation was not very clean. A new experiment was conducted to investigate this new isomer.

The experiment was performed at the Lohengrin separator at the ILL, Grenoble (see Section 2.2.2). A mixed ^{241}Pu ($\sim$70%) - ^{241}Am ($\sim$30%) target was used for the

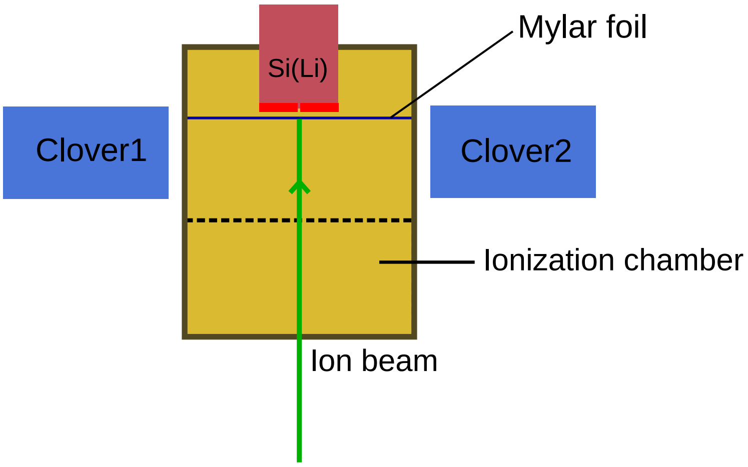

Figure 3.1: Schematic representation of the setup used in the experiment on ^{97}Rb and ^{97}Sr. The ion chamber was used to detect the ions and identify their mass. The two Clover detectors and the cooled Si(Li) detector were used to detect delayed γ rays. With the Si(Li) detector it was also possible to measure conversion electrons.

induced fission reaction. The ^{241}Am in the target is a product of ^{241}Pu β decay. The halflife of ^{241}Pu is $T_{1/2}$=14.290(3) a [70], so decay to ^{241}Am over the course of the experiment is negligible.

Very clean separation of fragments was achieved throughout the experiment, with a fraction of 84% of all registered ions being of mass A = 97. The measurement time was about three days. Ions were detected and identified using a split-anode ΔE_1-ΔE_2 ionization chamber filled with isobutane at a pressure of 44 mbar. The total count rate in the ionization chamber was about 700 ions/s at the beginning of the experiment and 520 ions/s towards the end. Due to target burn up, ion rates decreased over time. The ions were stopped in a 6 μm thick Mylar foil at the end of the chamber. A few millimeters behind the Mylar foil, a two-fold segmented Si(Li) detector was installed. The detector was cooled with liquid nitrogen to allow measurement of low-energy γ rays and conversion electrons with good energy resolution. The Si(Li) crystal was 4 mm thick. Each segment had an active area of 2 x 3 cm^2. The pressure of the isobutane in the ionization chamber was adjusted such that the incoming ions were stopped in the last quarter of the Mylar foil. This was done to assure that no ions hit the Si(Li) detector directly. By stopping the ions at the end of the Mylar foil, conversion electrons lost little energy on their way to the Si(Li) detector. This is important as one goal of the experiment was to measure low-energy conversion electrons. Outside the ionization chamber and perpendicular to the Mylar foil, two HPGe Clover detectors were placed in order to detect delayed γ radiation. A fixed coincidence window of 60 μs was set for ion-γ and ion-electron events. A schematic depiction of the detection setup can be found in Figure 3.1.

3.1.1 Calibrations

The energy calibration was done using in-beam β decay data. A linear fit brought an accuracy of 0.2 keV over the energy range from 50 keV to 1.4 MeV for the Clover detectors. In the case of the Si(Li) detector the low energy regime was of great importance. The setup allowed the measurement of energies down to about 11 keV. Low-energy γ rays and X rays following β decay of ^{97}Rb, ^{97}Sr and ^{97}Y - present as background - were used for the energy calibration. A separate calibration had to be done for the electrons, as they lose energy by traveling from the point of implantation of the ion to the Si(Li) detector and by passing the thin dead layer of the Si(Li) detector. The energy loss was of the order of 5 keV at a detected electron energy of 50 keV.

An absolute full-energy-peak efficiency calibration was performed for the Ge detectors and the Si(Li) detectors to determine conversion coefficients and branching ratios. This was achieved applying the sum peak method. If a γ ray with energy E_1 hits a detector, there is a certain probability, that a coincident γ ray with energy E_2 hits the same detector while charge collection is still in progress. This means the energy of both γ rays is detected as if they were a single one. For strong transitions, this becomes noticeable by the appearance of a sum-peak in the γ spectrum. In the calibrated energy spectrum the sum-peak appears at the summed energy $E_{\sum} = E_1 + E_2$. While in spectroscopy this effect is usually bothersome because it is in essence a contamination, it can be used to do an absolute efficiency calibration. Let N_E be the total number of decays of a transition with energy E (γ and conversion electrons) that happen during the measurement time. Let A_E be the measured volume of the same transition in the γ spectrum recorded with the detector whose efficiency is to be determined. Let us also assume a scenario of a cascade with exactly two transitions (like in Figure 2.1 (a)), i.e. $N_{E_1} = N_{E_2} = N_{\text{tot}}$[1]. Then the following set of linear equations is valid

$$\begin{aligned} A_{E_1} &= N_{\text{tot}}\epsilon_{E_1}\,\eta_{E_1} && (3.1)\\ A_{E_2} &= N_{\text{tot}}\epsilon_{E_2}\,\eta_{E_2} && (3.2)\\ A_{E_{\sum}} &= N_{\text{tot}}\;\epsilon_{E_1}\;\epsilon_{E_2}\;\eta_{E_1}\;\eta_{E_2}\;W(\Theta), && (3.3)\end{aligned}$$

where ϵ_E is the (full energy peak) γ detection efficiency at energy E and $\eta_{E_1} = \dfrac{1}{1+\alpha_{E_1}}$ with the total conversion coefficient α_{E_1} of the respective transition. $W(\Theta)$ accounts for the angular correlation and depends on the multipole character of the two transitions. As the two γ rays are detected in the same detector, $\Theta = 0°$ applies. The system of equations can be solved to obtain the unknown values ϵ_{E_1}, ϵ_{E_2} and N_{tot}.

$$\begin{aligned} \epsilon_{E_1} &= \frac{A_{E_{\sum}}}{A_{E_2}}\,\frac{1}{\eta_{E_1}\;W(\Theta = 0^\circ)}\\ \epsilon_{E_2} &= \frac{A_{E_{\sum}}}{A_{E_1}}\,\frac{1}{\eta_{E_2}\;W(\Theta = 0^\circ)}\\ N_{\text{tot}} &= \frac{A_{E_1}A_{E_2}}{A_{E_{\sum}}}\;W(\Theta = 0^\circ)\end{aligned}$$

---

[1] For more complex cascades branching has to be added.

With one such cascade the absolute efficiency of the detector can be determined for two energies. In case of a segmented system the procedure has to be applied for each segment individually.

The strong 197 keV → 381 keV → 1313 keV cascade depopulating the 1892 keV μs isomer in ^{136}Xe was used to perform the absolute efficiency calibration. Strong lines from β decay of ^{136}Xe, ^{142}La, and other isotopes were used for the relative efficiency calibration which was then shifted to match the absolute values. The results were throughout consistent. In this experiment the total efficiency of the Clover detectors was 16(2)% and 3.2(4)% for γ rays of 0.1 and 1 MeV, respectively.

The γ efficiency calibration for the Si(Li) detector could not be done using the sum peak method, as there were no sum peaks visible[2]. The absolute full energy peak efficiency was determined using equation (3.1). The total number of decays N_{tot} was obtained using the calibrated Clover detectors. The efficiency was compared to that obtained in earlier measurements which used the exact same detector and found to be consistent. The absolute photo efficiency of both segments of the Si(Li) detector combined was 3.3(7)% at 50 keV. The intrinsic efficiency for electrons is close to unity in the considered energy range. The absolute efficiency for electrons is a constant, governed mainly by the solid angle covered by the detector. It was measured to be 14(2)%.

3.1.2 Results

A background subtracted spectrum of delayed γ rays in coincidence with A = 97 fission fragments can be seen in Figure 3.2. The time window was set to 15 μs after arrival of the ions. Strong decay lines at 141 keV, 167.1 keV and 522.7 keV, originating from the decay of the 830 keV μs isomer in ^{97}Sr, can clearly be seen. Other transitions are discussed in the following Section (Sec. 3.2). A rather strong line is visible at 76.5 keV. A gate on this transition allowed for the determination of its lifetime using ion-γ timing as described in Section 2.2.3. The measured halflife of the 76.5 keV transition is $T_{1/2} = 5.1(4)$ μs, see Fig. 3.3. This value is very different to the $T_{1/2} = 526(13)$ ns reported for the 830 keV isomer in ^{97}Sr [72] and much longer than the halflife $T_{1/2} = 0.10(2)\mu$s measured for the 1264 keV isomer in ^{97}Zr [19]. Apart from these two, there is no report on isomers with halflifes in the μs region in fission fragments with mass A = 97. This leads to the conclusion that the transition belongs to a previously unknown μs isomer in a A = 97 nucleus.

Two methods were used to identify the nuclear charge Z of the isotope emitting the new 76.5 keV γ transition. First the Si(Li) was used to measure X rays in coincidence with the K-electron conversion line of the transition. A background subtracted spectrum of delayed conversion electrons and photons in the range of 3.75 μs to 17.25 μs after the arrival of an A = 97 fission fragment can be seen in Figure 3.4(a). The time window was chosen this way in order to ensure that no γ rays from the decay of the

---

[2] The photo effect, responsible for the full energy peaks, has a strong Z dependence of $Z^{4.5}$ (see e.g. [71]). Thus sum peak detection is much more likely in germanium detectors than in silicon detectors ($Z_{\mathrm{Si}} = 14, Z_{\mathrm{Ge}} = 32$). Furthermore, the Si(Li) segments were much thinner than the Clover Ge-crystal.

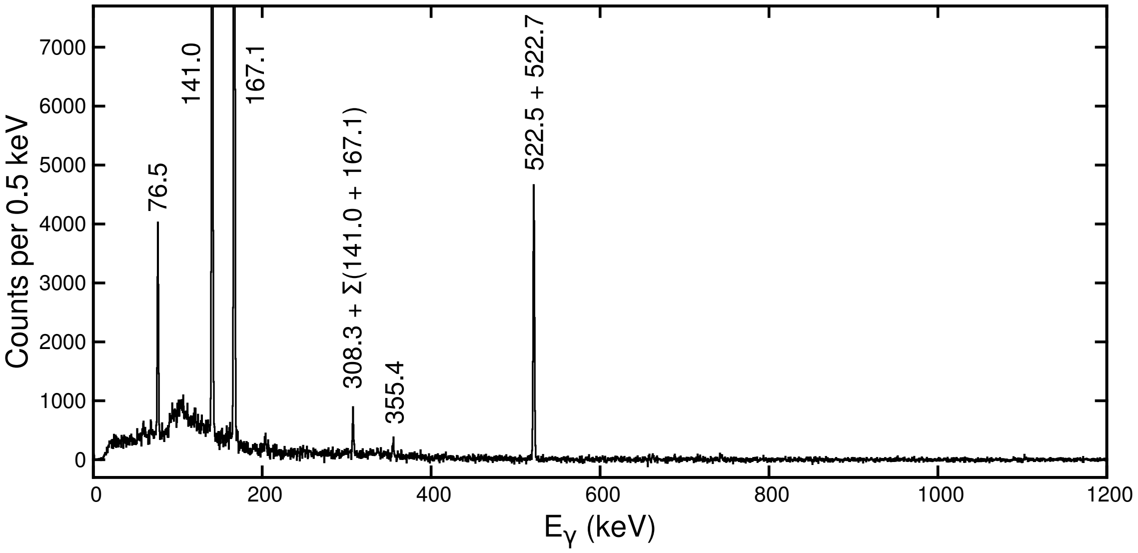

Figure 3.2: Background subtracted spectrum of delayed γ rays up to 15 μs after the arrival of an ion of mass A = 97. The spectrum was measured with the two Clover detectors.

strongly populated 830 keV isomer in ^{97}Sr appear in the spectrum. In Figure 3.4(b), a coincidence spectrum of one of the Si(Li) segments, with a gate on the K-conversion line of the 76.5 keV transition in the other segment, is shown. Only one X ray transition at an energy of E = 13.4(2) keV can be seen in coincidence. The K$_\alpha$ X ray energies for Kr, Rb, Sr, Y and Zr are 12.6, 13.4, 14.1, 14.9, and 15.7 keV respectively [8]. With this the 76.5 keV transition can be assigned to ^{97}Rb.

To confirm this result the energy loss of A = 97 ions in the first part of the ionization chamber was analyzed. This technique has been used before to assign delayed transitions in ^{95}Y [63] and ^{107}Tc [73]. The mean energy loss, ΔE_1, depends on the nuclear charge Z. A calibration was performed by measuring ΔE_1 of ions in coincidence with the strong 522 keV line of the μs isomer in ^{97}Sr, and of all A = 97 ions as shown in fig. 3.5(a). A mean value of Z=38.8(1) for all A = 97 fission fragments was calculated using independent fission yields of ^{241}Pu from the ENDF/B-VII database [59]. By assuming a linear correlation between ΔE_1 and Z, it was possible to determine a calibration factor of ΔE_1 = 17.5 channels per $\Delta Z = 1$. Note that the contribution from ^{241}Am fission fragments with mass A = 97 was less than 10% of all ions detected with this mass. ^{241}Am itself is not fissile by thermal neutrons, but undergoes fission after capture of two neutrons. The resulting influence on mean Z of the total distribution was calculated to be negligible. For comparison, expected distributions of ^{97}Y and ^{97}Zr are shown in Figure 3.5(a) as solid lines. The areas under the peaks correspond to the independent fission yields, normalized to the total distribution. The width corresponds to the width of the measured ΔE_1 distribution of ^{97}Sr. The positions of the maxima of the distribution for the different A = 97 isobars are shown in Figure 3.5(b) along with the ΔE_1 distribution of ions in coincidence with the 76.5 keV transition. An expected distribution for ^{97}Rb ions is drawn as a solid line. The centroid position was taken from the calibration, the width was taken from the ^{97}Sr distribution. Only

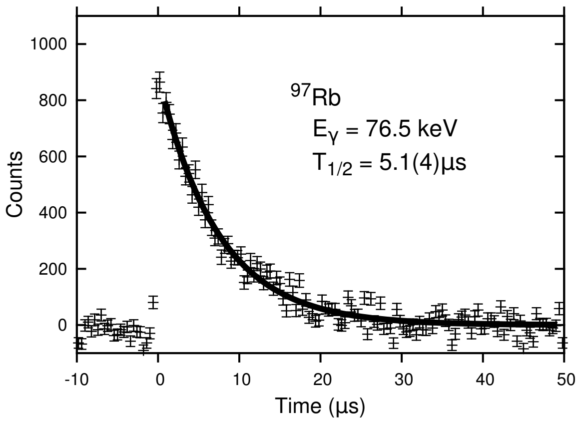

Figure 3.3: Ion-γ time difference spectrum for the delayed 76.5 keV transition from the isomer of ^{97}Rb.

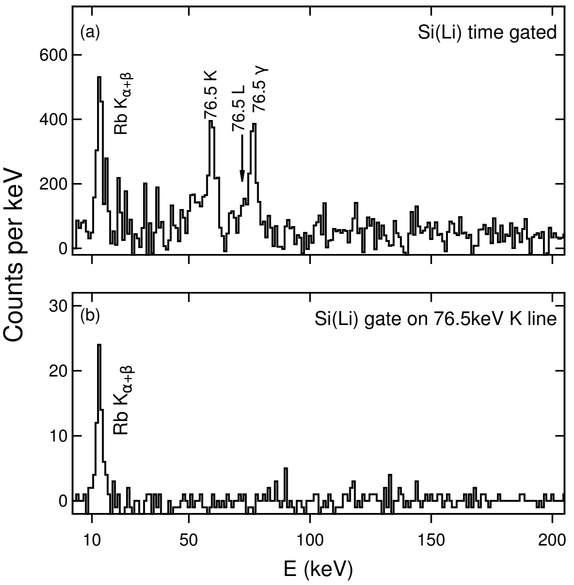

Figure 3.4: Delayed conversion electrons and X rays observed in the Si detectors in a time range 3.75–17.25 μs after the arrival of an A = 97 ion: (a) singles spectrum with subtracted β decay background and (b) Si-Si coincidences gated on the K electrons of the 76.5-keV transition.

the area under the distribution was adjusted to the experimental data for comparison. Based on this analysis the transition is assigned to ^{97}Rb, in accordance with the X ray measurement.

The Si(Li) detector allowed for conversion electron spectroscopy. The K conversion coefficient α_{K} was determined, as described in Section 2.3. Comparing the K-conversion line intensity to the intensity of the γ line in the Si(Li) detector, $\alpha_{\mathrm{K}} = 0.16(4)$ was measured for the 76.5 keV transition. A comparison to the γ intensity measured with the Clover detectors yielded $\alpha = 0.21(3)$. Both values are in agreement with each other. Predicted K conversion coefficients for a 76.5 keV transition in rubidium are 0.187(3), 0.269(5) and 2.14(4) for E1, M1 and E2 respectively [6]. The experimental results are sufficiently precise to determine the multipole character of the transition to be E1. An upper limit of $\alpha_{\mathrm{L}} < 0.07$ was determined for the L conversion coefficient. This result is in agreement with $\alpha_{\mathrm{L}} = 0.0206$ [6], predicted for E1 multipolarity of this transition.

No γ rays (apart from rubidium X rays) or conversion electrons were observed in coincidence with the 76.5 keV transition. Therewith the transition is possibly a direct ground state transition of an isomeric state at energy $E = 76.5$ keV. In this scenario, the E1 character of the transition constricts spin and parity of the isomer to $1/2^-$, $3/2^-$, $5/2^-$, as the ground state spin and parity of ^{97}Rb were measured to be $3/2^+$ [74]. However, it cannot be unambiguously shown from the data that the 76.5 keV γ

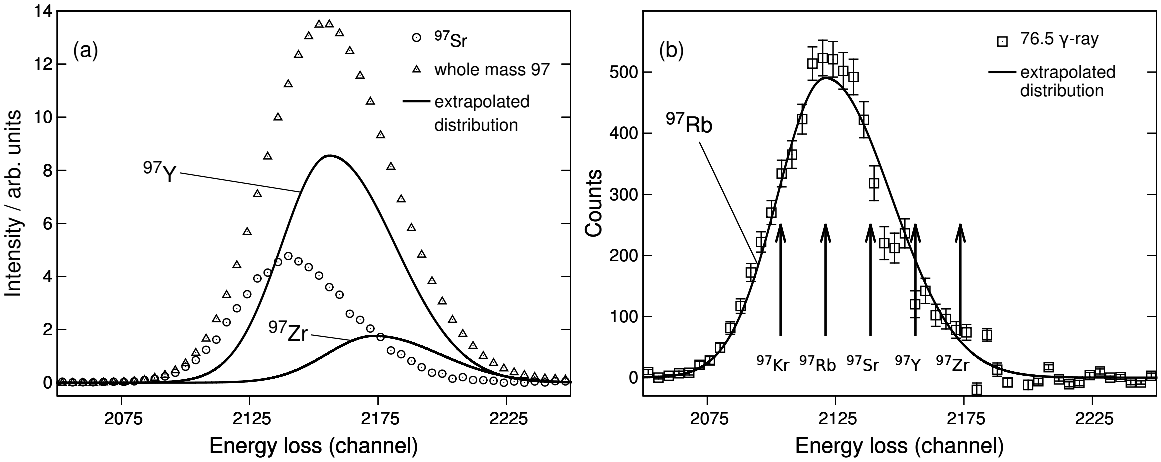

Figure 3.5: Measured energy loss ΔE_1 in the first stage of the ionization chamber for (a) ^{97}Sr and all ions with mass A = 97 and (b) ions in coincidence with the 76.5 keV γ ray. Solid lines show extrapolated distributions of other mass A = 97 isotopes that are strongly produced in the fission reaction ^{241}Pu(n_{thermal},F). Arrows are drawn in (b) that indicate the centroid position of these distributions. See text for more details.

ray belongs to the ground state transition from the isomeric state. The detection limit of the Si(Li) detector was around 11 keV, so an upper limit of 90 keV is given for the excitation energy of the μs isomer responsible for the delay of the 76.5 keV transition. The results are summarized in Table 3.1.

Table 3.1: Results on the delayed 76.5 keV transition in ^{97}Rb. α_K is the weighted average of the two results gained using the Si(Li) detector and the Clover detectors. See text for more details.

Nucl.	E_{isomer} (keV)	E$_{\text{trans}}$ (keV)	$T_{1/2}$ (μs)	α_K	α_L	σL
^{97}Rb	<90	76.5(2)	5.1(4)	0.19(3)	<0.07	E1

3.2 ^{97}Sr

The 830.8 keV isomer in ^{97}Sr was investigated at Lohengrin before. Its decay scheme and lifetime was measured by Zlomaniec *et al.* [72], a slightly more precise halflife value was obtained in a measurement presented in chapter 4 of this work. The improved statistics for fission fragments of mass A = 97 gathered in the experiment allowed to establish a new decay branch of the 830.8 keV isomer of ^{97}Sr, besides the known, strong 522.7 keV transition. Figure 3.6 shows the time distribution of delayed 522.7 keV γ rays after the arrival of an A = 97 fission fragment. The deduced half-life is 515(10)

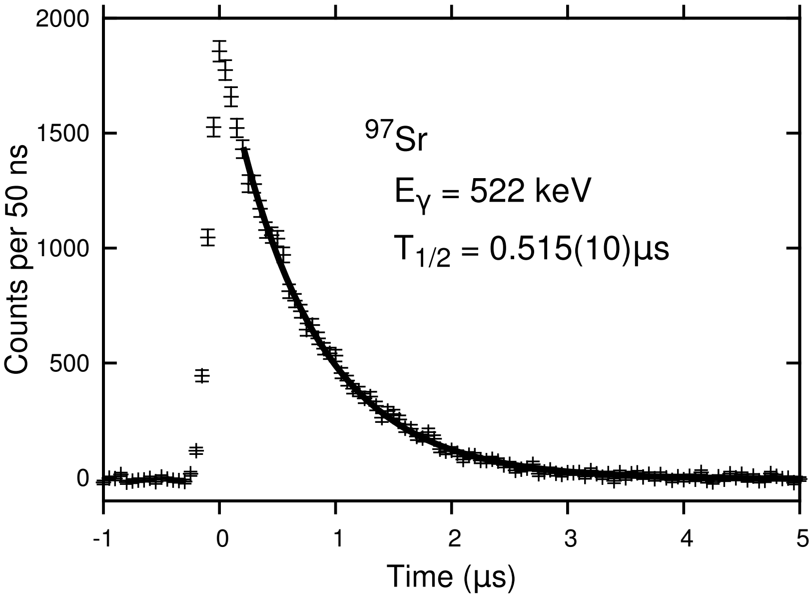

Figure 3.6: Ion-γ time difference spectrum for the 522.7 keV transition from the 830.8 keV isomer of ^{97}Sr.

ns, in agreement with the value reported in [72] and the one presented in Section 4.1 of this work.

In Figure 3.2, two weak transitions can be seen at energies of 308 keV and 355 keV. An analysis of γ-γ coincidences allowed these transitions to be assigned to the 830.8 keV isomer decay of ^{97}Sr. The 355 keV transition was observed in coincidence with the 167 keV ground state transition of the first excited state of ^{97}Sr, as can be seen in Figure 3.7(a) and 3.7(c). Furthermore, the halflife of this transition can be measured to be 505(40) ns, in agreement with the isomer half-life $T_{1/2} = 526(13)$ ns reported in [72], and the 515(10) ns measured in this work. Figures 3.7(b) and 3.7(c) show a clear coincidence of 308.3 keV γ rays with the 355.3 keV transition. In the coincidence spectrum of the 308.3 keV line (3.7(b)) a transition at 522.5 keV and signs for a very weak one at 214 keV can be seen as well. In previous β decay studies, a level at 522.4 keV was reported, which decays via γ rays of energy 522.5, 355.3 and 214.3 keV [75, 76]. Based on the coincidence data it is evident, that the same level was populated in the present work. The sum of the measured energies of the 522.4 keV level and the new 307.3 keV transition adds up to the excitation energy of the 830.8 keV isomer. All these considerations allowed for the construction of the revised isomer decay scheme shown in Figure 3.8. The spin of the isomer was assumed to be $(9/2^+)$ [72].

It should be added, that the peak at 308 keV in Figure 3.2 is an unresolved doublet of the 308.3 keV transition and the sum-peak of the strong 141.0 and 167.1 keV transitions. Due to this fact the peak area of the 522.5 keV transition in Figure 3.7(b) is larger than it would be expected from the decay branching of the 522.4 keV state reported in a β decay study by Lhersonneau *et al.* [75]. The contribution of this sum peak can be calculated with the efficiency calibration, but its contribution cannot be excluded in the coincidence spectra. The 522.5 and 522.7 keV transitions are also

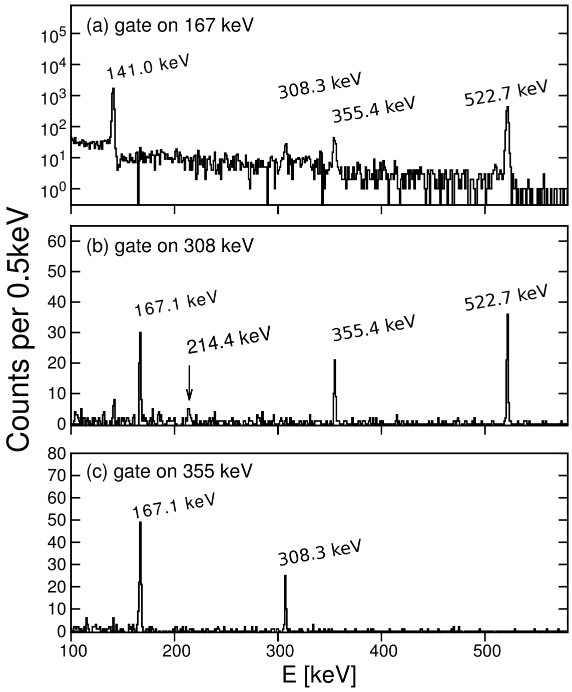

Figure 3.7: γ ray coincidence spectra obtained by setting gates on the indicated delayed transitions from the decay of the 830.8 keV isomer in ^{97}Sr.

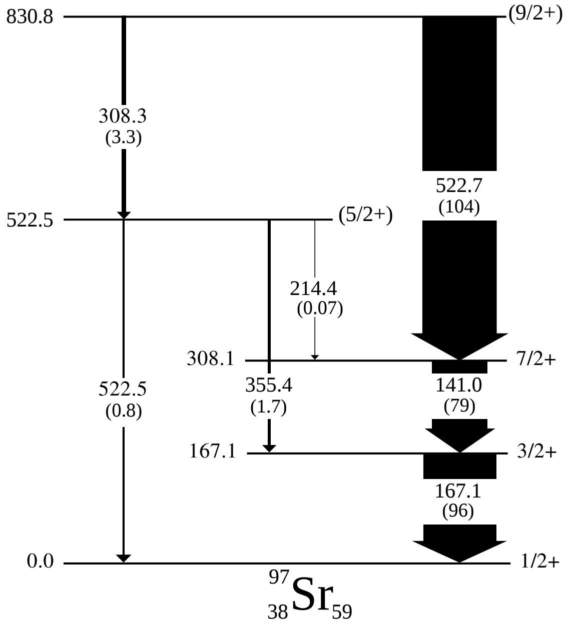

Figure 3.8: Decay scheme of the 830.8-keV isomer of ^{97}Sr obtained from the present work. The relative γ-intensity of each transition is given in brackets. See the text and Table 3.2 for more details.

observed as an unresolved doublet.

The relative transition and γ-intensities of the 830.8 keV isomer of ^{97}Sr are shown in Table 3.2. They were obtained from single spectra and gated coincidence spectra using the absolute efficiency calibration for the Clover detectors (see Section 3.1). The unavoidable sum-peak contribution to the 308 keV γ rays made a determination of the 522.5 keV γ-intensity impossible with the data from this experiment. Therefore, the branching ratios of the 522.4 keV level reported in [75] were used to determine the branching of the weak 214 and 522 keV transitions. The intensities were normalized to the intensity of the 355.4 keV transition measured in this work.

Table 3.2: Level energies, γ ray energies, and intensities of the delayed cascade of ^{97}Sr up to 6.75 μs after the arrival of an A = 97 ion. The newly found transition is labeled with an asterisk *. The uncertainty on the measured γ ray energies is 0.2 keV.

Level energy (keV)	E_γ (keV)	I_γ (rel.)	I_{Total} (rel.)
167.1	167.1	96(19)	100(20)[a]
308.1	141.0	79(23)	102(29)
522.5	214.4	0.07(3)	0.07(5)[b]
	355.4	1.7(5)	1.7(5)
	522.5	0.8(3)	0.8(3)[bc]
830.8	308.3*	3.3(12)	3.4(12)[c]
	522.7	104(30)	105(35)[c]

[a] Reference transition ($I_{\text{Total}} = 100$), including conversion-electron intensity.

[b] The relative intensities of the weak 214.4 and 522.5 keV lines were obtained from the branching ratios reported in Ref. [75], after normalization to the measured intensity of the 355.4 keV transition.

[c] The 522.5 and 522.7 keV γ rays are observed in the singles spectrum as an unresolved doublet, as are the 308.3 keV transition and the sum peak at 167.1 + 141.0 keV. The individual intensities are extracted from coincidence spectra and comparison with other peak intensities. The measured intensities of the 522 and 308 keV doublets are I_γ = 105(30) and 7.7(22), respectively.

3.3 ^{99}Y

The second experiment planned and performed within the scope of this thesis was a fast timing measurement on nuclei in the neutron rich region around N=60. The aim was to measure lifetimes of excited states in ^{99}Y and ^{100}Nb, in order to shed light on their structure and collectivity. The measurement on both nuclei took place within 14 days in October 2012. The lifetimes were measured with the delayed coincidence method, using four LaBr detectors. The time spectra were analyzed using the generalized centroid difference method 2.1.4.

The experiment was performed at the Lohengrin separator at the ILL, Grenoble (see Section 2.2.2). The nuclei were produced in an induced fission reaction in a ^{235}U target. Incoming ions were detected with a split-anode ΔE_1-ΔE_2 ionization chamber filled with isobutane at a pressure of 20 mbar. The ions were stopped in a block of scintillating fiber optics. The scintillator block consisted of approx 1 mm thick fibers glued together. Outside the ionization chamber the fiber optics were optically connected to a position sensitive photo multiplier tube (PSPMT), in order to measure the implantation position of each detected ion. Around the ionization chamber, perpendicularly to the beam direction, four LaBr detectors were installed in a close geometry. Each detector consisted of a 1.5″ x 1.5″ cylindrical LaBr$_3$:Ce crystal, connected to a Hamamatsu R9779 photo multiplier tube. The energy resolution was about 8 % at 140 keV and below 5 % for energies larger than 600 keV. A schematic depiction of the detection setup is shown in Figure 3.9. The time difference between the LaBr signals was measured with time to amplitude converters (TACs) in a common stop set-up (see Section 2.1.1). The TAC range was set to 50 ns. A time calibration was performed using an Ortec 462 time calibrator. The calibration factor was similar for each of the three TACs, and had a value of 2.0 ± 0.1 ps/channel.

The data were collected in list mode using xia digital gamma finders[3]. Events were

---

[3] Xia digital gamma finder (DGF) 4C revision E, www.xia.com/Manuals/

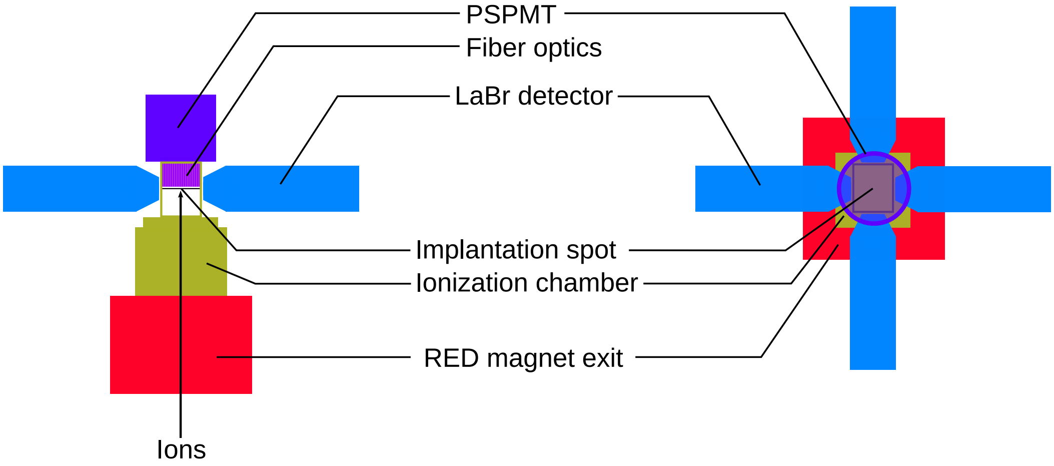

Figure 3.9: Schematic representation of the setup used in the experiment on ^{99}Y and ^{100}Nb. The ion chamber was used to detect the ions and identify their mass.

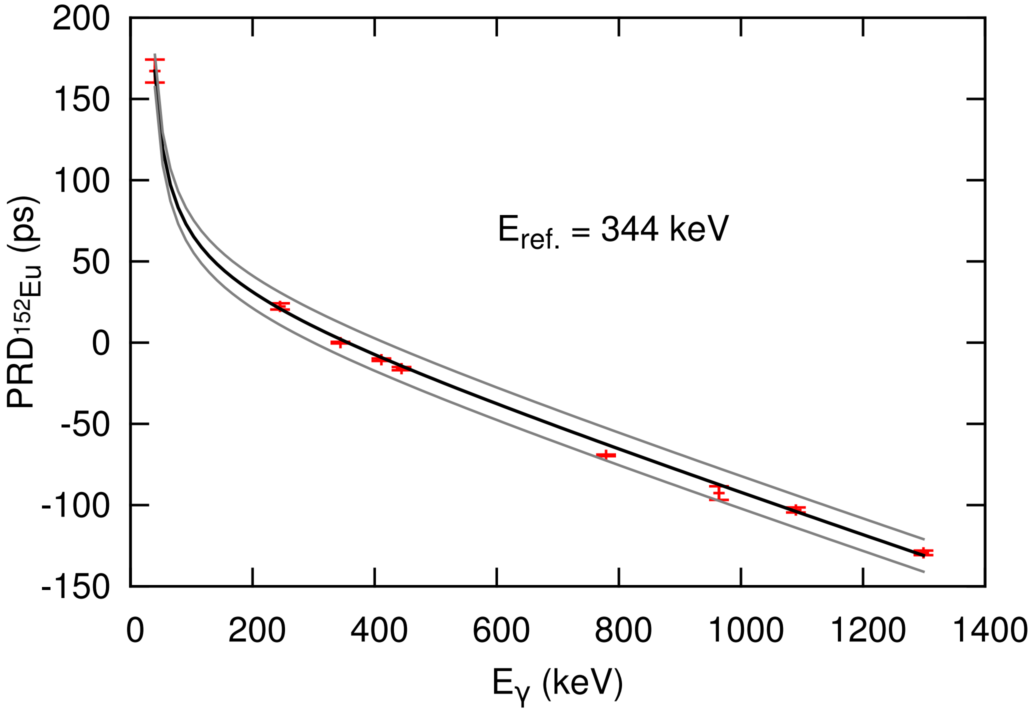

Figure 3.10: Mean prompt response difference curve of the four LaBr detectors for reference energy $E_{\text{ref}} = 344$ keV. The data points were measured with a ^{152}Eu source. A fit of the function from equation (2.6) is shown as a solid black line. This fit is used as the mean PRD calibration. The adopted calibration uncertainty of ±10 ps is indicated with grey lines.

recorded if either of two trigger conditions was met. The first condition was a hit in the first part of the ionization chamber and a simultaneous hit in the PSPMT. The trigger window was set to 80 μs after the arrival of the ion. This condition was chosen in order to get a clean signal from the μs isomer cascade by suppressing background from β decay. As a second condition, a LaBr multiplicity of 2 was set, in order to gather more statistics for lifetimes measurements in nuclei populated after β decay. The trigger window for this condition was set to 15 μs. Very clean separation of fragments was achieved throughout the experiment, with a fraction of 97% of all registered ions being of mass A = 99. The total count rate in the ionization chamber was about 2500 ions/s. The measurement time was about six days.

Lifetimes were measured using electronic fast timing of delayed $\gamma\,\gamma$ coincidences. With a setup of four detectors, the GCD analysis formalism is the method of choice for lifetime determination. The method is described in detail in Section 2.1.4. The time spectra of all detector combination are added together, which increases statistics and simplifies analysis. The difference between delays of each detector combination was corrected for, by measuring the centroid of the strong 779 keV - 344 keV cascade in ^{152}Eu and then shifting all distributions to a reference position. This constant shift introduces no additional error to the measurement of the centroid difference. In order to extract lifetimes from the measured centroid differences, the prompt response difference (PRD) has to be known. A ^{152}Eu source was used to perform a calibration of the mean

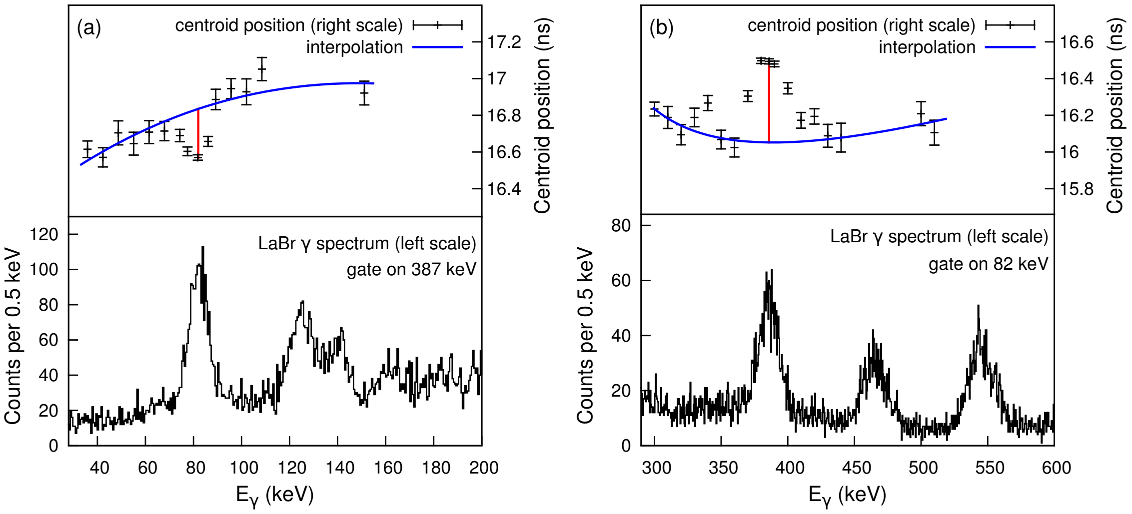

Figure 3.11: Interpolation of delayed background contribution to the centroid position at full energy peak position for lifetime determination of the 387 level in ^{99}Nb. Each centroid position was determined from a γ-γ gated time spectrum. The first gate was set on 387 keV (a) and 82 keV (b). The second gate was set at the indicated energy in the γ spectrum shown in the bottom panel. The width of the second gate was 6 keV (a) and 10 keV (b). Only the points outside the full energy peaks are used for the fit. See also Section 2.1.5.

prompt response difference (PRD) of the timing setup, as described in Section 2.1.4. The PRD calibration is shown in Figure 3.10. and the estimated uncertainty of the PRD calibration, which is 10 ps. The difference between the PRD and a delayed centroid is two times the lifetime (see Section 2.1.4). That means, based on this calibration, the lower detection limit of the system is $\tau > 5$ ps, or $T_{1/2} > 4$ ps. This is comparable to what has been achieved in other fast timing experiments (see e.g. [49]). The ^{152}Eu calibration was done after the experiment, with the ion chamber removed. As it is remarked in [53], a slight change of the setup geometry will not affect the PRD,

$$PRD(E) = PRD_{^{152}Eu}(E).$$

The effectiveness of the GCD in the current experiment was tested by re-measuring short (< 5 ps) or well known halflifes [77] of excited states in ^{99}Nb after β decay. It is worth mentioning that the halflife of $T_{1/2} = 173(4)$ ps of the 469 state was confirmed with the present data by a convolution fit as well (see below). A partial level scheme of ^{99}Nb, reproduced from [77], is shown in Figure 3.12(left). Halflifes of excited states in ^{99}Nb measured in this work are listed in Table 3.3. They agree well with the values given in [77].

An important systematic error in fast timing measurements is caused by the time distribution of the background. The measured centroid has to be corrected for the background contribution, as described in Section 2.1.5. The background contribution to the centroid in the TAC spectrum is determined by gating on one transition and then setting gates in the background around the corresponding coincident transition.

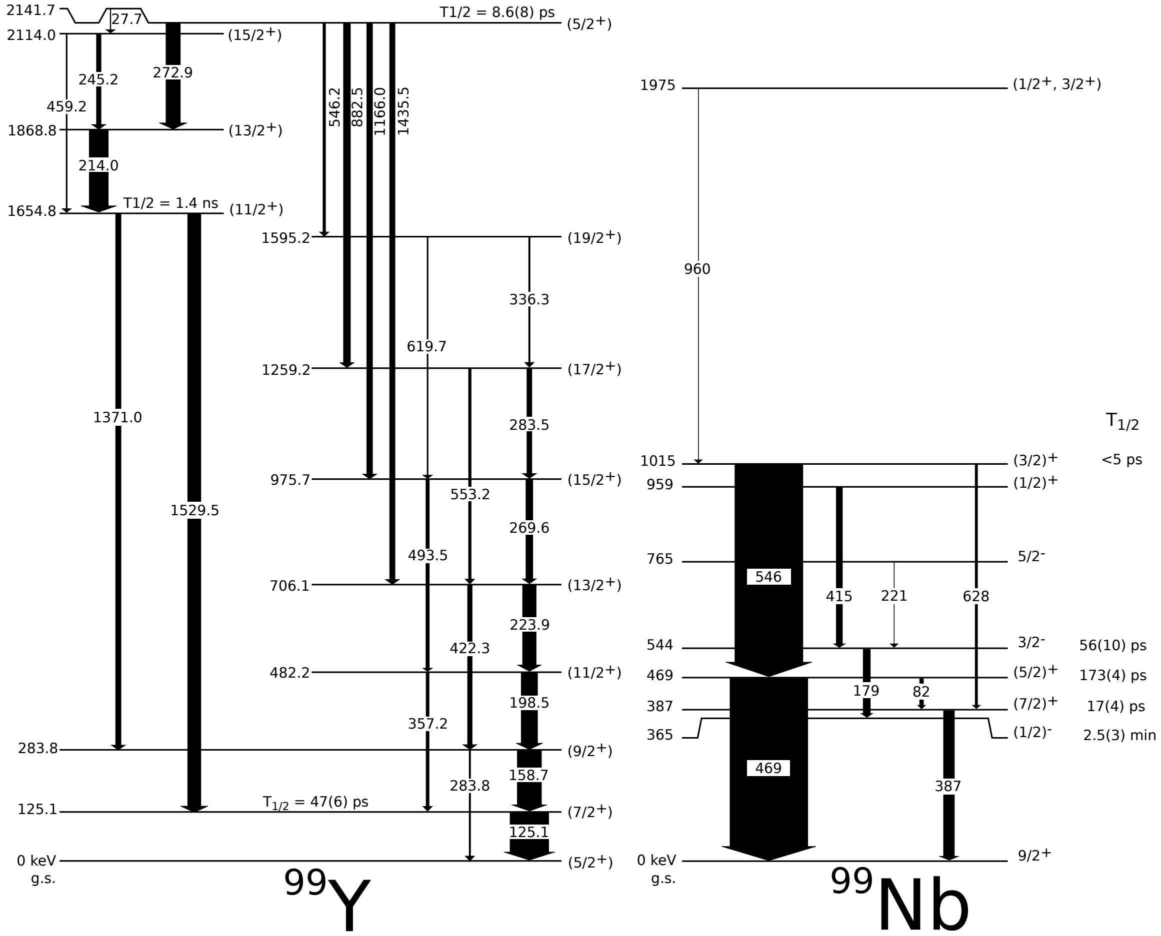

Figure 3.12: (left) Level scheme of the μs isomer decay cascade in ^{99}Y, reproduced from [78]. Known halflives are taken from [77]. (right) Partial β decay level scheme of ^{99}Nb, based on data from [77]. In both level schemes arrow width is proportional to γ intensity.

In this way the background contribution can be interpolated. By determining the peak to background ratio within the gate limits of the coincident transition, the centroid can then be corrected (see equation (2.7)) to obtain the true full energy peak centroid. One such background interpolation is shown in Figure 3.11 for the coincident transitions 82 keV and 387 keV from ^{99}Nb. Note, that the correction procedure given in the appendix of [49] cannot be applied here, because the peak to background ratios of the two full energy peaks is not approximately the same.

Figure 3.13 shows a background subtracted LaBr energy spectrum of delayed γ rays up to 15 μs after the arrival of an ion. The strong transitions from the decay of the 2142 keV μs isomer in ^{99}Y can clearly be seen. An isomer decay scheme, base on the data from [78] is shown in Figure 3.12(right). To confirm the isomer halflife it was measured using the delayed coincidence method. A spectrum of the time difference between ions with mass A = 99 and γ rays from the unresolved doublet of the 273 keV and 269 keV transitions is shown in Figure 3.14. The 273 keV line depopulates the isomer directly. The state of the 269 keV transition is fed directly from the isomer and from states of the ground state band. Assuming the lifetime of these states is

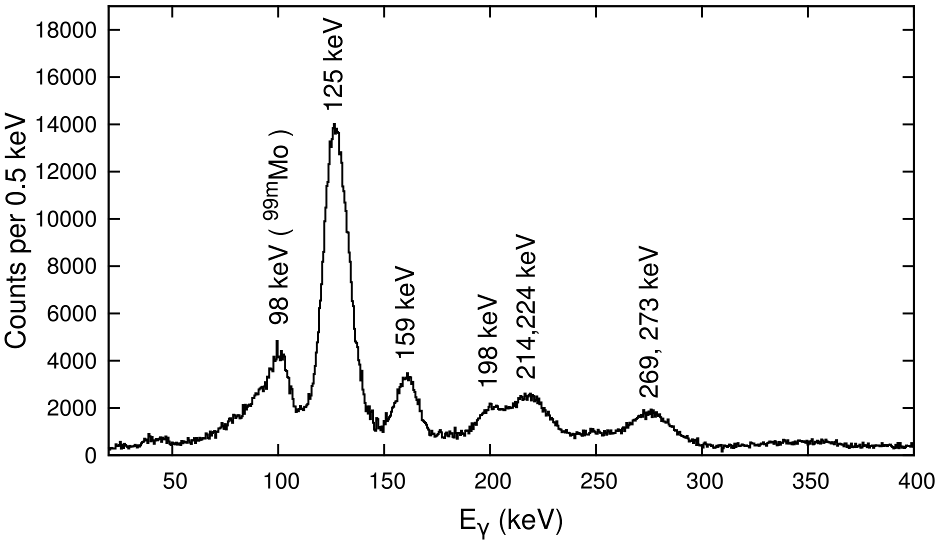

Figure 3.13: Background subtracted LaBr energy spectrum of delayed γ rays in a range until 15 μs after the arrival of an A = 99 ion. Strong transitions from the μs isomer decay in ^{99}Y are indicated with their energy. Another delayed transition from a μs isomer in ^{99}Mo is also visible.

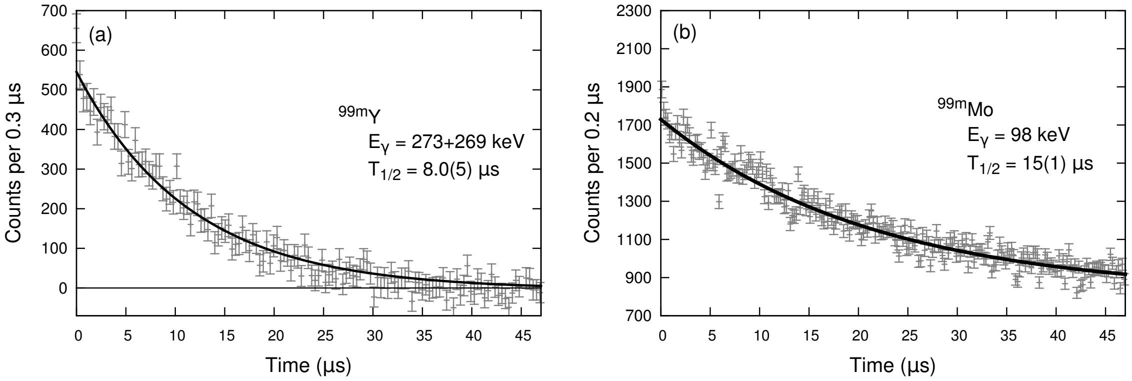

Figure 3.14: Ion γ time difference spectra of the delayed transitions at 273 keV and 269 keV (unresolved doublet) in ^{99m}Y (a) and the delayed 98 keV transition in ^{99}Mo (b).

shorter than 1 ns, the delay of the feeding can be neglected. A fit of the slope yields a halflife of 8.0(5) μs for the isomer at 2142 keV in ^{99}Y. This value is in agreement with a previous measurement at Lohengrin by Genevey *et al.* [66] (11(2) μs) and with the value of $T_{1/2} = 8.6(8)$ μs, published by Meyer *et al.* [78].

Figure 3.16 shows gated spectra with coincidences which were used to determine level lifetimes. The level scheme is crowded, and many transitions overlap in the single spectra. Still level lifetimes can be determined, because the respective coincident transitions can be resolved. An example is the 273 and 269.6 keV doublet. The 273 keV transition feeds the $(13/2^+)$ level at 1869 keV, while the 269.6 keV transition feeds the $(13/2^+)$ ground state band level at 706.1 keV. The two transitions cannot be resolved,

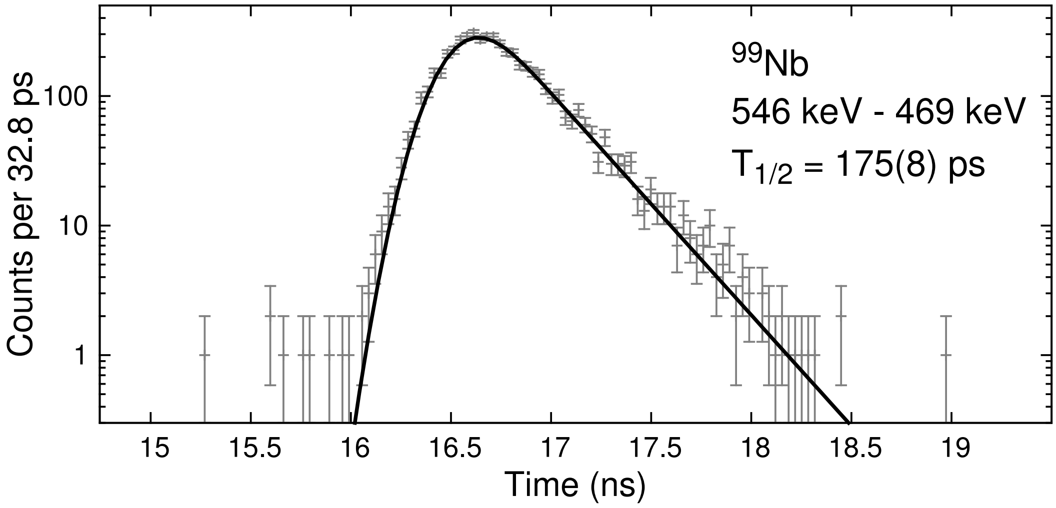

Figure 3.15: Convolution fit to obtain the lifetime of the 469 keV state in ^{99}Nb.

but the 273 keV is stronger, and the coincident transition with energy 214.0 keV can be separated from the 223.9 keV transition with a narrow gate. The $(13/2^+)$ level at 1868.8 keV is also fed by a rather strong transition with 245.2 keV, allowing for a cross check of the result. It was however not possible to determine a lifetime from the 269 keV - 223.9 keV coincidence. The halflife of the $(5/2^+)$ level at 469 keV in ^{99}Nb is long enough to be determined with a fit of the convolution given in equation (2.2) to the delayed time distribution (see Figure 3.15). The halflife of $\mathrm{T}_{1/2} = 175(8)$ ps, measured in this way, confirms the value of 173(4) ps given in [77]. A halflife of $T_{1/2} = 3.8(10)$ ns was measured for the $(11/2^+)$ state at 1655 keV in ^{99}Y, using the slope method with the 214 keV - 1530 keV coincidence. The order of magnitude of this value agrees with the 1.4 ns (no uncertainty stated) measured by Meyer *et al.* [78]. The halflife of the μs isomer at 98 keV in ^{99}Mo was measured using ion γ timing with a gate on the 98 keV ground state transition which directly depopulates the isomer. Note, that the lifetime is so long, that the constant background cannot be determined from the spectrum, but has to be fitted simultaneously. This increases the uncertainty of the fit (see Figure 3.14).

The halflifes of seven excited states in ^{99}Y were measured, four of them for the first time. Furthermore, halflifes of an excited state in ^{99}Nb and ^{99}Mo were measured in this experiment. The results are compiled in Table 3.3. Measured halflifes agree with literature values, as far as they are available.

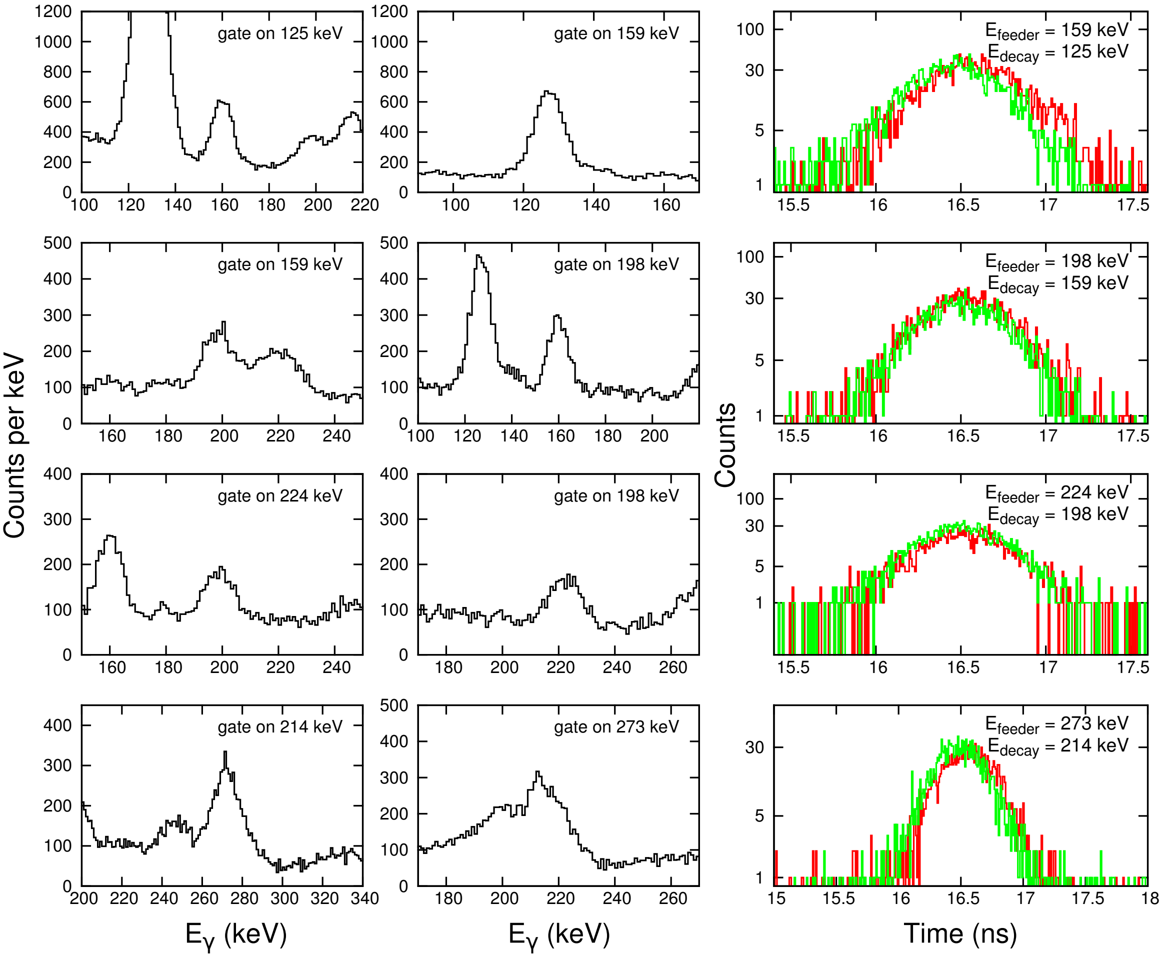

Figure 3.16: Gated LaBr γ spectra of coincident transitions from the isomeric cascade in ^{99m}Y (left). On the right, TAC spectra of the corresponding distributions D_{stop} (red) and D_{start} (green) are shown. It can be clearly seen how width of the distributions is correlated to the energy of decay and feeder.

Table 3.3: Lifetimes of excited states in nuclei with mass A = 99 measured in this work. New lifetimes are set in bold face. Spin, parity and level energy are taken from [77] and [78]. †: convolution fit, ‡: slope fit, *: weighted average.

Nucl.	Spin(parity)	E_{level} (keV)	E_{feeder}	E_{decay}	$T_{1/2}$ (ps)
^{99}Y	$(7/2^+)$	125.1	159	125	60(10)
			1529.5	125	68(50)
					57(10)*
	$(9/2^+)$	283.8	198.5	159	**19(6)**
			422.3	159	**22(8)**
					20(4)*
	$(11/2^+)$	482.2	224	198.5	<**15**
	$(11/2^+)$	1654.8	214	1529.5	1.6(4) ns ‡
	$(13/2^+)$	1868.8	272.9	214	**21(9)**
			245	214	**30(18)**
					23(6)*
	$(15/2^+)$	2141.7	ion	273+269	8.0(5)μs‡
^{99}Nb	$(7/2^+)$	387	82	387	11(6)
			628	387	13(8)
			960	628	12(5)*
	$(5/2)+$	469	546	82	189(25)
			546	469	172(6)
			546	469	175(8)†
			960	628	175(5)*
	$3/2^-$	544	415	179	51(13)
	$(3/2)^+$	1015	960	546	6(8)
			960	628	8(13)
			960	628	<12*
^{99}Mo	$5/2^+$	97.8	ion	98	15(1)μs‡

3.4 ^{100}Nb

The measurement on ^{100}Nb was performed during the same campaign as that on ^{99}Y, described in the previous Section. Setup and conditions were the same. Separation of the desired mass was equally good. Mass A = 100 was run at the beginning of the campaign and towards the very end. The total count rate in the ionization chamber was about 5000 ions/s and about 900 ions/s respectively. Ion rates drop during the experiment due to burn up of the fission target. The measurement time was about five days.

A background subtracted LaBr energy spectrum of delayed γ rays up to 15 μs after the arrival of an ion is shown in Figure 3.17 (b). Transitions from the decay of the x + 421 keV μs isomer in ^{100}Nb can clearly be seen. An isomer decay scheme, based on the data from [66] is shown in Figure 3.17(a). A spectrum of the time difference between ions with mass A = 100 and γ rays from the 185.4 keV transition is shown in Figure 3.19(a). A fit of the slope yields a halflife of 11(2) μs for the isomer at 420 keV in ^{100}Nb, which is in agreement with previously reported values [79]. The halflife, measured with the 185.4 keV transition, is ascribed to the isomer, which is reasonable, considering the data from [66]. It is assumed, that the halflife of the 392.3 keV state is negligible (i.e. < 10 ns), and that the isomeric character of the delayed cascade is solely due to the hindered 28 keV transition. As this transition was not seen in the present data, a direct measurement of the isomer lifetime is not possible. For the same reason no lifetime for the (6-) state at 392.3 keV can be extracted.

The reliability of the PRD calibration curve was ensured by measuring centroid differences of coincident transitions in ^{100}Mo. The first excited 2^+ state in this nucleus is fed by two transitions with an energy of 159 keV and 528 keV, respectively. The depopulating transition has an energy of 535 keV. Several consistent halflife values are available for this state, each with a precision below one picosecond. The value of $T_{1/2} = 12.6(2)$ ps [80] is in good agreements with the value of $T_{1/2} = 16(5)$ ps measured in this work with the GCD method (see Table 3.4).

Figure 3.18 shows gated spectra of coincident γ rays which were used to determine lifetimes with the GCD method. This also includes γ rays emitted after β decay. The halflifes of the excited state at 207 keV above the (5^+) millisecond isomer in, populated in the isomeric cascade in ^{100}Nb, was measured for the first time. The halflife of the first excited 1^+ state in ^{100}Nb, populated after β decay of ^{100}Zr, was also measured for the first time. Before only an upper limit of $T_{1/2} = 0.19(23)$ ns was known [81]. The halflife of the first excited 2^+ state in ^{100}Zr, populated after β decay of ^{100}Y, was measured using the GCD method and with a slope fit (see Figure 3.19(d)). Both results are consistent within the measurement uncertainty. The same was found for the first excited 0^+ state in ^{100}Mo. (see Figure 3.19(d)) All measured lifetimes are shown in Table 3.4.

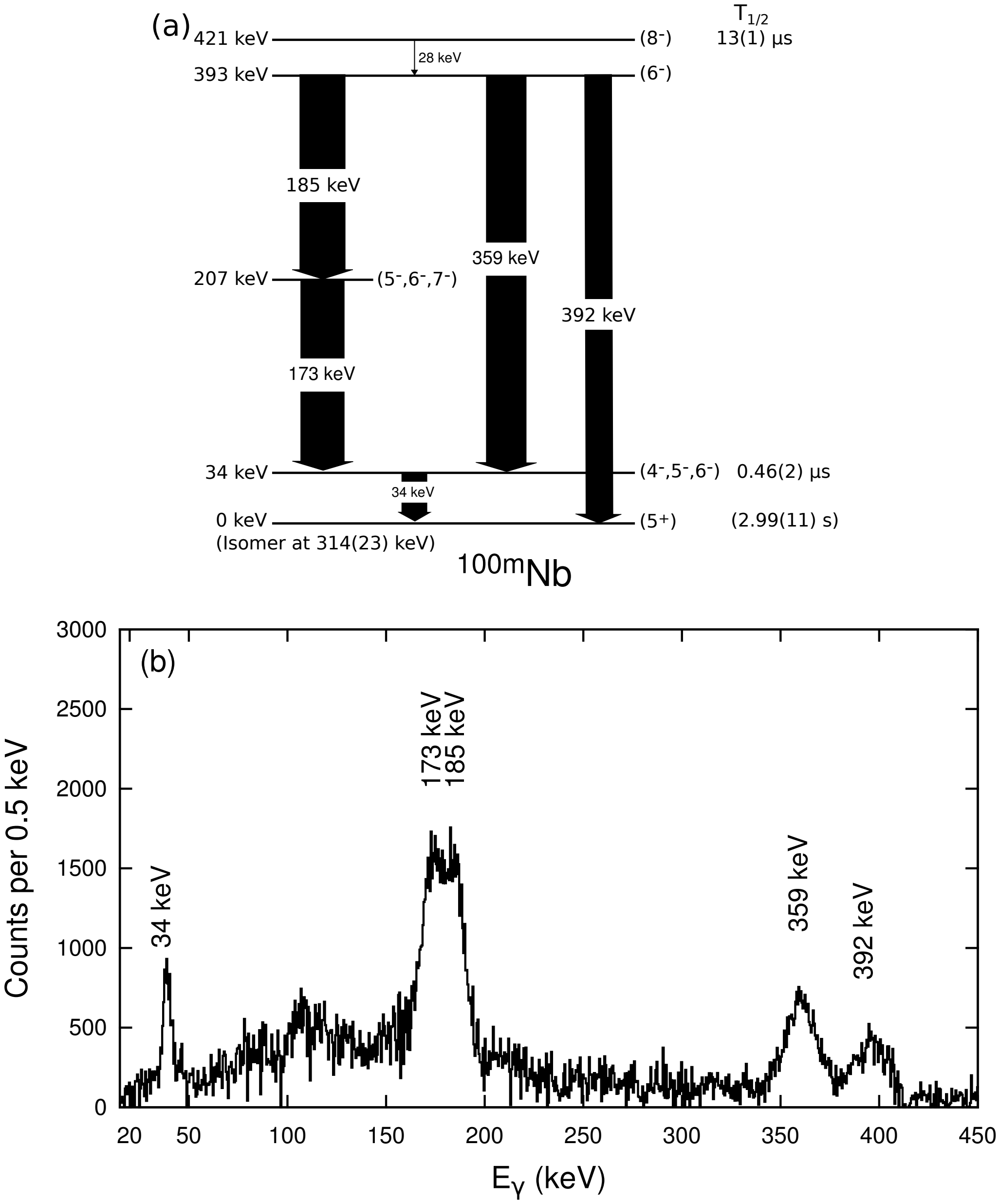

Figure 3.17: (a) Isomer decay scheme of ^{100}Nb [66]. (b) Background subtracted LaBr energy spectrum of delayed γ rays in a range until 15 μs after the arrival of an A = 100 ion. Strong transitions from the μs isomer decay in ^{100}Nb are indicated with their energy.

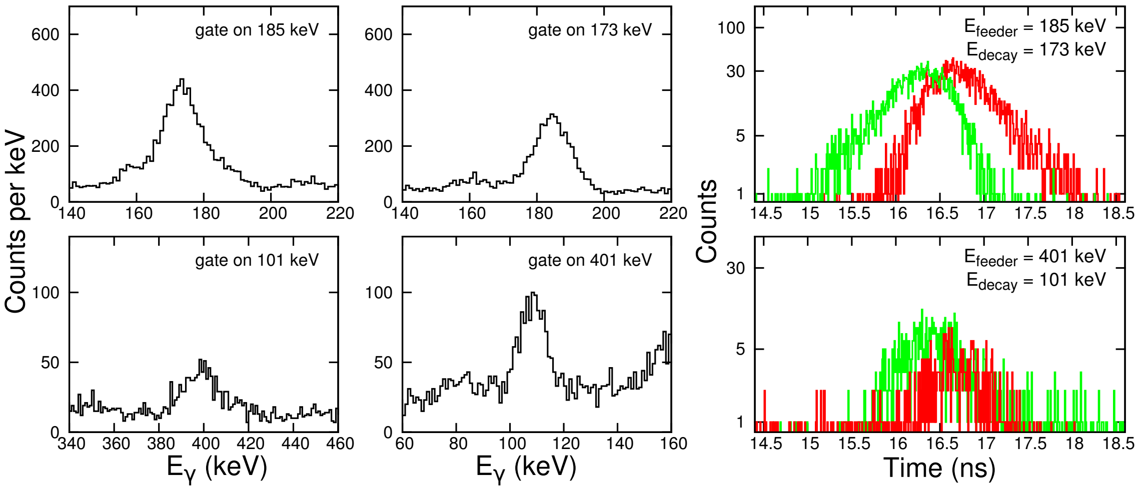

Figure 3.18: Gated LaBr γ spectra of coincident transitions from ^{100}Nb (left). On the right hand side, TAC spectra of the corresponding distributions D_{stop} (red) and D_{start} (green) are shown.

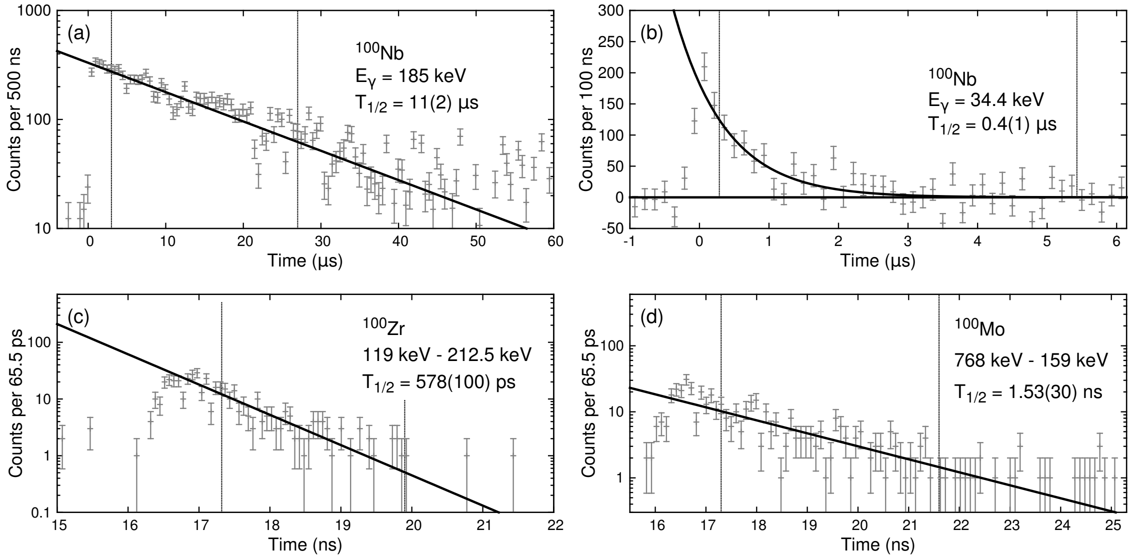

Figure 3.19: The two top panels show ion γ time difference spectra with a LaBr gate on the 185 keV line (a) and the 34 keV line (b) from ^{100}Nb which depopulate long lived isomers. The bottom panels show TAC spectra of coincident transitions populating and depopulating the 2_1^+ state in ^{100}Zr (c), and the 0_1^+ state in ^{100}Mo (d). A slope fit is plotted with a solid line, fit regions are indicated with vertical lines.

Table 3.4: Lifetimes of excited states in nuclei with mass A = 100 measured in this work. New lifetimes are set in bold face. Energies and spin and parity assignments are taken from [79]. Following [66], x corresponds to the excitation energy of the 5+ isomer of ^{100}Nb (see also Fig. 3.17(a)). †: convolution fit, ‡: slope fit, *: weighted average.

Nucl.	Spin(parity)	E_{level} (keV)	E_{feeder}	E_{decay}	$T_{1/2}$ (ps)
^{100}Nb	$(4^-,5^-,6^-)$	34.3+x	ion	34.4	0.4(1)μs‡
	$(5^-,6^-,7^-)$	207.4+x	173.3	185.4	**196(15)**
			173.3	185.4	**232(35)**†
					207(14)*
	(8^-)	420.7+x	ion	185.4	11(2)μs‡
	1^+	400.5	103.7	400.5	**90(30)**
^{100}Zr	2^+	212.5	119	212.5	582(60)
			119	212.5	578(100)‡
					573(50)*
^{100}Mo	2^+	695.1	159	535	18(9)
			528	535	14(6)
					16(5)*
	0^+	695.1	768	159	1.50(6)ns
			768	159	1.53(30)‡
					1.50(5)*

Chapter 4

Excursus: μs isomers in light fission fragments

In this chapter the results of a three week measuring campaign investigating μ-second isomers, performed in October 2009 at the Lohengrin separator (see Section 2.2.2) at the ILL, Grenoble, are presented. Information on the existence and lifetime of μ-second isomers in atomic nuclei is crucial, e.g. to understand their β- and γ-decay schemes. See Section 1.5 for a brief introduction to isomers in nuclear physics. The Lohengrin mass separator at the research reactor of the ILL, provides excellent conditions for lifetime measurements of μ-second isomers in neutron-rich nuclei. The mass region below ^{132}Sn and between mass 91 and 109 has been investigated using this instrument (see e.g. Refs. [66, 73, 64]). However in the region north-east of the doubly-magic nucleus ^{78}Ni, with A<90 and neutron number N>50, no μ-second isomers, besides in ^{88}Br, were identified so far. Isomerism in this region could arise due to the strongly interacting $\pi f_{5/2}$ and $\nu d_{5/2}$ orbitals or from core excitation of $\nu g_{9/2}$ neutrons. The search for previously unobserved μ-second isomers was one of the goals of this measuring campaign. Several μ-second isomers in the mass region $79 \leq A \leq 100$ were observed only once, and with large relative uncertainty of the reported lifetime. In ^{79}As, ^{88}Br, ^{97}Sr and ^{98}Y literature values disagrees. Therefore the second goal was to remeasure the lifetimes of the known isomers in this region.

The nuclei of interest were produced after fission of ^{233}U or ^{235}U (separate targets of both isotopes were used) induced by thermal neutrons in the high neutron flux (10^{14}s^{-1}) near the core of the reactor at the ILL. The fission fragments were selected with the Lohengrin mass separator [60], see also Section 2.2.2 of this work. The selected ions were focused onto an ionization chamber by the RED magnet (reverse energy dispersion dipole magnet [82]). The split anode ionization chamber, divided into two parts by a thin polypropylene window supported by a tungsten grid, was used as a ΔE-E telescope for identification of the fragments. In this experiment, 16 HPGe detectors (one Euroball Cluster, two Clover detectors and one coaxial germanium detector) were placed in a close geometry around the ionization chamber.

4.1 Isomer lifetimes

4.1.1 Analysis

The lifetimes of the isomeric states were determined by measuring the time between incoming ions and coincident γ rays as described in Section 2.2.3. In the nuclei ^{97}Sr and ^{98}Y there is more than one μs isomer in cascade. In these cases the lifetime of the isomer with the lowest level energy was determined using γ-γ fast timing by gating on directly populating and depopulating transitions. The lifetime of an isomer in ^{97}Zr was determined using γ-γ timing after β decay of ^{97}Y. No correlation with an incoming ion was requested in that case.

The data was acquired using digital electronics[1] and then analysed using several coincidence conditions. Over the three weeks of measurement time data was recorded with several settings of the Lohengrin separator (see Section 2.2.2) to investigate different portions of the mass region of interest. For each setting several masses A were identified using the ΔE-E signal of the ionization chamber. Each mass was then analysed separately. Most isomers were seen in more than one data set, allowing, to a certain degree, to cross-check the results. The coincidence window for γ rays following the detection of a fission fragment was set to 50 μs, except where otherwise noted.

4.1.2 Results

In this experiment the haflives of a total of 17 isomers in the neutron-rich nuclei ^{79}As, ^{83,88}Br, ^{85,95}Kr, ^{96}Rb, ^{97}Sr, ^{92,94,95,98}Y, ^{97,98}Zr, and ^{100}Nb were measured. All of these 17 μs isomers have been measured before. The results of this experiment are given in Tabel 4.1. The adopted values are the weighted averages of the results gained from different Lohengrin settings. For all isomers the results from different settings were consistent within the error. A comparison to literature values can be found in Tabel 4.2. The precision of the lifetimes of the isomers in ^{79}As, ^{88}Br, ^{97}Sr and ^{98}Y was considerably improved with respect to earlier measurements. Figure 4.1 shows representative γ ray and ion-γ time-difference spectra. In the following some of the observed isomers are briefly discussed in comparison to results of earlier measurements.

^{79}As

The isomeric $(9/2)^+$ state in this nucleus decays via an M2 transition to a $(5/2)^-$ state. In Ref. [86] it is suggested that the isomerism is due to the configuration of the single proton $(5/2)^-$ state as well as the deformation of the nucleus, manifested in the excitation energy of the $(9/2)^+$ state and the small M2 strength of this transition. Two literature values for the lifetime of this isomer are available [87, 86]. Both were measured applying the same technique as in this work, but with different production methods. The two literature values are contradictory (see Tab. 4.1). The result of this work is in agreement with that of Ref. [87].

---

[1] Xia digital gamma finder (DGF) 4C revision E, www.xia.com/Manuals/

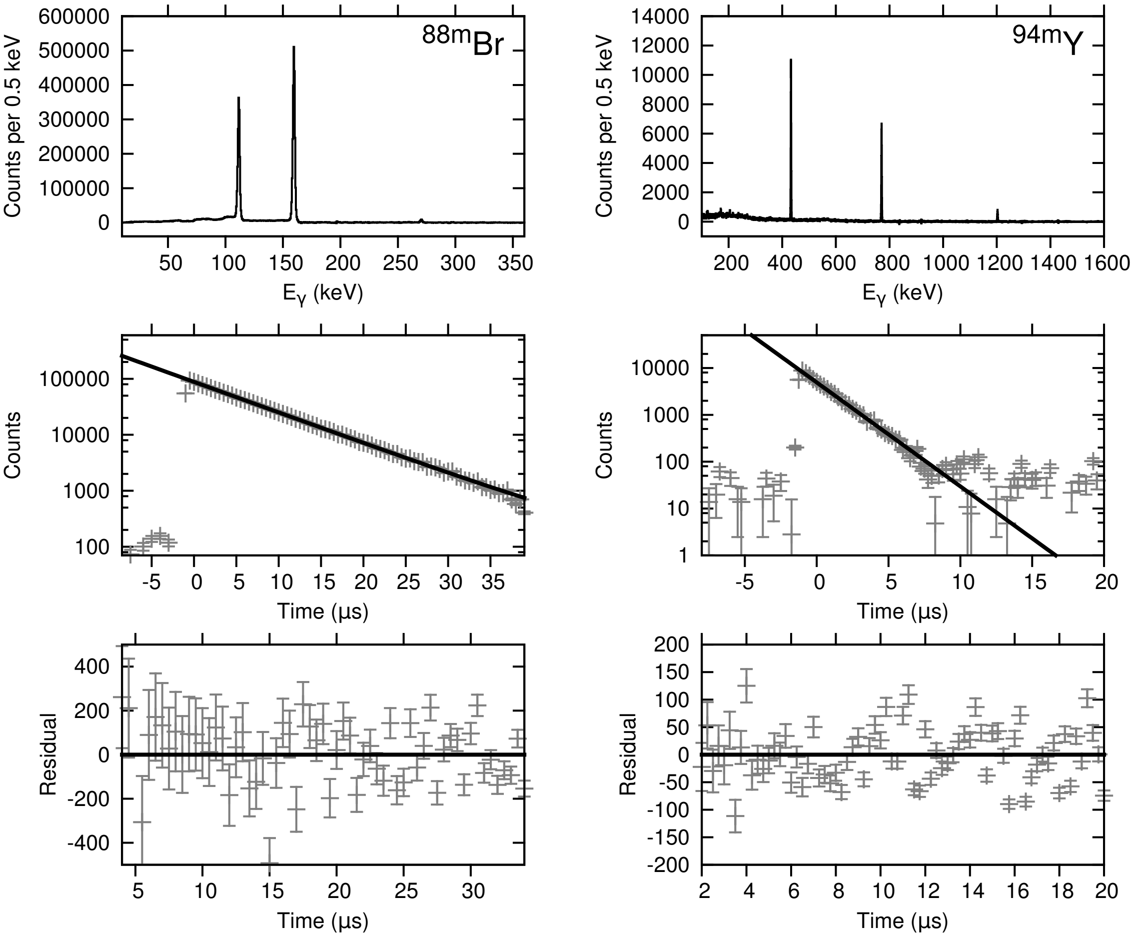

Figure 4.1: Example of data from two Lohengrin settings with delayed transitions from μs isomers in ^{88}Br (left) and ^{94}Y (right). The upper panels show background subtracted γ ray spectra with delayed transitions. The lower panels show the respective ion-γ time-difference spectra with corresponding lifetime fits (solid line) and the fit residual. See text and Section 2.2.3 for more details. Results given in Table 4.1 are weighted averages of results from different Lohengrin settings.

Table 4.1: Adopted isomer lifetimes determined in this work. Spin and parity assignments as well as level and transition energies are taken from the Nuclear Data Sheets [19, 22, 24–28, 47, 83–85]. For reasons of clearness a comparison with literature values can be found in a separate Table (Tab. 4.2) *: discussed in the text, †: γ-γ timing

Nuc.	I^{π}_{iso}	$E^{\mathrm{level}}_{\mathrm{iso}}$(keV)	E_{γ}(keV)	$\mathrm{T}_{1/2}$(μs)
^{79}As*	$(9/2)^{+}$	773	231/542	1.18(4)
^{83}Br	$(19/2^{-})$	3069	255/303/357/510/609	0.8(2)
^{88}Br*	$(4,5^{-})$	270	111/159	5.51(4)
^{85}Kr*	$(17/2^{+})$	1992	1931	1.82(6)
^{95}Kr	$(7/2^{+})$	196	114	1.82(5)
^{96}Rb	(10^{-})	1135	300	1.77(6)
^{97}Sr*	$(9/2^{+})$	831	522	0.52(1)
		308	141/167	0.181(4)†
^{92}Y	unknown	unknown	315/492	3.3(6)
^{94}Y	(5^{+})	1202	432/769/1202	1.10(1)
^{95}Y	$9/2^{+}$	1087	261/826	48.6(5)
^{98}Y	(8^{-})	1181	101/111/130/158/186	0.80(2)
	(2^{-})	496	121/204/275	6.87(5)
	(2^{-})	171	170/51	0.61(1)†
^{97}Zr	$7/2^{+}$	1264	1103	0.106(2)†
^{98}Zr	(17^{-})	6603	1223	1.4(5)
^{100}Nb	8^{-}	420+x	173/185/359	12.4(3)

^{88}Br

The configuration of the isomer in ^{88}Br is identified as $\{\nu(d_{5/2})\pi(p_{3/2})\}4^{-}$ by Genevey *et al.* [66], based on calculations of the hindrance factor for a single proton transition to the lower lying 2^{-} state. For this nucleus we were able to gather good statistics with several settings of Lohengrin (see Fig. 4.1 as an example for the data analysis of one setting). The weighted average of the individual measurements is given in Tab. 4.1. The uncertainty is one order of magnitude smaller than that of the literature values. The result of the present measurement is in agreement with earlier measurements by Genevey *et al.* [66] and Sellam [91], but 15% smaller than the value reported by Grüter *et al.* [90]. It should be pointed out that the lifetime of this isomer was also measured by Folden *et al.* [94]. However the lifetime is shown only in a Figure, with a value lower than the one adopted in the Nuclear Data Sheets [22], supporting the result of the present work.

^{85}Kr

The μ-second isomer at E = 1992 keV in ^{85}Kr decays to the ground state via a cascade of two γ rays with energies of 60 keV and 1931 keV. The 60 keV transition

Table 4.2: Adopted isomer lifetimes determined in this work. Literature values are given in the rightmost column. In the case of strongly disagreeing literature values, the extreme values are cited, along with the weighted average from the Evaluated Nuclear Structure Data File labelled with ‡. Individual citation of sources is given along with the literature value. Spin and parity assignments as well as level and transition energies are taken from the Nuclear Data Sheets [19, 22, 24–28, 47, 83–85]. *: discussed in the text,

Nuc.	I^{π}_{iso}	$E^{\text{level}}_{\text{iso}}$ (keV)	$T_{1/2}$ (μs)	$T_{1/2}$(lit.) (μs)	
^{79}As*	$(9/2)^+$	773	1.18(4)	0.87(6)	[86]
				1.21(1)	[87]
^{83}Br	$(19/2^-)$	3069	0.8(2)	0.7(1)	[88]
				0.6(2)	[89]
^{88}Br*	$(4,5^-)$	270	5.51(4)	6.3(5)	[90]
				5.1(4)	[66]
				4.9(4)	[91]
				5.3(4)‡	[22]
^{85}Kr*	$(17/2^+)$	1992	1.82(6)	$1.2(^{+10}_{-4})$	[89]
^{95}Kr	$(7/2^+)$	196	1.28(5)	1.4(2)	[63]
^{93}Rb*	(10^-)	257	not observed	57.0(150)	[90]
^{96}Rb	(10^-)	1135	1.77(6)	1.65(15)	[66]
				2.0(1)	[92]
^{97}Sr*	$(9/2^+)$	831	0.52(1)	0.526(13)	[72]
				0.263(24)	[93]
				0.395(20)‡	[19]
		308	0.181(4)	0.244(132)‡	[19]
^{92}Y	unknown	unknown	3.3(6)	$4.2(^{+8}_{-6})$	[94]
^{94}Y	(5^+)	1202	1.30(1)	1.35(2)	[66]
^{95}Y	$9/2^+$	1087	48.6(5)	52.6(12)	[64]
^{98}Y	(8^-)	1181	0.80(2)	0.83(10)	[95]
	(2^-)	496	6.87(5)	7.2(1)	[66]
				8.0(2)	[95]
				7.6(4)‡	[27]
	(2^-)	171	0.61(1)	0.62(8)	[95]
^{97}Zr	$7/2^+$	1264	0.106(2)	0.103(2)‡	[19]
^{98}Zr	(17^-)	6603	1.4(5)	1.9(2)	[65]
^{100}Nb	8^-	420+x	12.4(3)	13.1(10)	[66]

was observed in this experiment, but statistics and peak-to-background ratio made it difficult to determine the lifetime via this transition (a time correlation with incoming ions was obvious though). Spin and parity of the isomeric ($17/2^+$) level were assigned based on the relative excitation function in (α,nγ) of the 60 keV γ ray and its total conversion coefficient by Winter *et al.* [89]. The half life for the 1992 keV isomeric level determined in this work (1.82(6)μs) is based on the 1931 keV γ ray analysis. The lifetime of the populated level at 1931 keV was measured to be shorter than 1 ps in [96]. This contribution is thus negligible when measuring the 1992 keV level lifetime using ion-γ fast timing with the 1921 keV transition. The value measured in this work is larger than the result reported in Ref. [89] ($1.2(^{+10}_{-4})\mu$s), which is the only previously published value. Due to the large uncertainty of the earlier measurement both values are in agreement.

^{93}Rb

Grüter *et al.* [90] proposed an isomeric state in ^{93}Rb at 257 keV with a half life of $T_{1/2} = 57(15)$ μs. This isomer was also observed by Ressler *et al.* [97] (using the same technique as in [90]) but not in this experiment. The respective γ ray was observed, yet no time correlation with incoming ions was found, using a 109 μs coincidence window. The data does not support isomeric character of this state.

^{97}Sr

The literature values for the lifetime of the 831 keV isomer in this nucleus are strongly discrepant as can be seen in Tab. 4.1. In this work only the 522 keV transition was used to deduce the lifetime of the 831 keV isomer, as it directly depopulates this state. The 141 and 167 keV transitions were used for γ-γ timing with the 522 keV line to deduce the lifetime of the intermediate 308 keV state (see Tab. 4.1). Our result of $\tau = 0.52(1)$ μs (see Fig. 4.1) is in agreement with an earlier measurement performed at Lohengrin by Zlomaniec *et al.* [72]. On the other hand, two values, reported by Hwang *et al.* [93, 98], from measurements at GAMMASPHERE, yielded $\tau = 0.263(24)$ μs and $\tau = 0.255(56)$ μs respectively, i.e. only half of our value. The reason for this large discrepancy is not clear to us. The lifetime was also measured by Monnad *et al.* [99] to be $\tau = 0.515(15)$ μs, in perfect agreement with our measurement. But in Ref. [93] it is stated that this value is wrong due to an analysis error, which is not discussed in more detail. After applying a correction which is not specified, given by one of the authors of Ref. [99], a new value of $\tau = 0.255(10)\mu$s is reported in Ref. [93] for the value measured by Monnad *et al.* [99], which is consistent with the lifetime values measured by Hwang *et al.* [93, 98]. Measurements of the isomer ratio of this state, presented in Section 4.2, seem to indicate a lifetime longer than $\tau = 0.26(3)$ μs. Some more details are given in the conclusion of that Section.

4.1.3 Conclusion

In this Section results of an investigation of the search for μ-second isomers in neutron rich fission fragments with mass $79 \leq A \leq 100$ were reported. The measured lifetimes of 17 isomeric levels in 14 nuclei are presented in Tab. 4.1. In this work, many of the isomeric halflifes were determined with considerably higher precision than before. Concerning previously unknown isomers, we found indications for a new μ-second isomer with mass A = 97 in this data. In a dedicated experiment, which was performed within the scope of this thesis and is reported on in chapter 3.1, it was possible to clearly shown this isomer belongs to ^{97}Rb.

4.2 Isomer population ratios

Fission of a nucleus results in the production of two new nuclei[2], and typically several neutrons. In Section 2.2.1 the process of fission is described in more detail. After fission, the product nuclei are in an excited energy state. If there are isomers present in the fragment, they will be populated to a certain degree after the fission process. Those fission products, that are not trapped in an isomeric state, de-excite to the ground state after a short time. The probability of populating an isomer depends on the nuclear structure and the energy of the product. This fact makes isomer fission yields a direct observable of the fission process which can be used to test models. There are, for example, statistical models that link this probability to the isomer's spin and the mean spin of the excited fragment after fission (see e.g. [100]). Information on fission yields of isomers with lifetimes in the millisecond region and above is abundant, e.g. [59, 101], while data on fission yields of μs isomers is scarce. This work attempts to start to fill these gaps. The method of analysis is described in Section 4.2.1, the results are presented in 4.2.2.

4.2.1 Analysis

A possible way to specify an isomer fission yield is the isomer ratio. The isomer ratio R_{isomer} is defined as the number of nuclei of an isotope ${}^{A}_{Z}\text{X}$ being in the respective isomeric state relative to the total number of nuclei of this isotope, produced after fission.

$$R_{\text{isomer}} = \frac{N^{{}^{A}_{Z}X}(\text{isomer})}{N^{{}^{A}_{Z}X}(\text{total})}$$

By this definition the value R_{isomer} cannot be larger than one. In addition to isomeric lifetimes, presented in the previous Section, isomer ratios, as defined above, were extracted from the data. This was also done with the data sets of the experiments presented in chapter 3. Some details on the procedure how these values were extracted from the data are presented in the following.

Determination of $N^{{}^{A}_{Z}X}$(isomer)

In order to extract the isomer ratio, first the number of ions which arrive at the implantation point in the isomeric state (N_{ip}) has to be determined. This was done using an absolute efficiency calibration of the HPGe detectors. This calibration was done using the method of sum-peak statistics (see Section 3.1, calibrations). From this value, the corresponding number of ions in the isomeric state at target position $N^{{}^{A}_{Z}X}_{\text{target}}$(isomer), i.e., directly after fission, can be extrapolated by taking into account the time of flight t_{ToF} and the lifetime τ of the isomer applying the exponential decay law. For a single isomer the following equation holds for the number of isomers in

---

[2] Note, that ternary and higher order fission also occurs. It is several orders of magnitude less likely than binary fission.

target and implantation position, N_{target} and N_{ip}:

$$N_{\mathrm{target}} = N_{\mathrm{ip}} \exp\left(\frac{t_{ToF}}{\tau}\right).$$

The time of flight was determined using the kinetic energy of the fission fragments, which is selected by the Lohengrin setting, and the length of the flight path, which is 23.15 m.

If the considered isomer is populated by another μs isomer, this feeding has to be taken into account when calculating the population directly after fission. The solutions to the problem of multiple population and decay channels are called the Bateman equations ([52]). For the frequently encountered case of two isomers $E_{\mathrm{a}} > E_{\mathrm{b}}$ with lifetimes $\tau_{\mathrm{a}} = 1/\lambda_{\mathrm{a}}$ and $\tau_{\mathrm{b}} = 1/\lambda_{\mathrm{b}}$ the original population of isomer b can be calculated from the equation

$$N^{\mathrm{b}}_{\mathrm{target}} = \left(N^{\mathrm{b}}_{\mathrm{ip}} - \frac{\lambda_{\mathrm{a}}}{\lambda_{\mathrm{b}} - \lambda_{\mathrm{a}}} N^{\mathrm{a}}_{\mathrm{target}} \left(e^{-\lambda_{\mathrm{a}} t_{\mathrm{ToF}}} - e^{-\lambda_{\mathrm{b}} t_{\mathrm{ToF}}}\right)\right) e^{\lambda_{\mathrm{b}} t_{\mathrm{ToF}}}.$$

Note, that the original population $N^{\mathrm{a}}_{\mathrm{target}}$ of the higher lying isomer has to be determined first.

The largest contribution to the experimental uncertainty of $N^{^A_ZX}$(isomer) comes from the absolute efficiency calibration and amounts to about 15% in the worst case.

Determination of $N^{^A_ZX}$(total)

The total number $N^{^A_ZX}$(total) cannot be obtained in this direct way with the Lohengrin spectrometer. The different isomers can only be distinguished by mass A using the ΔE-E analysis, but not by atomic charge Z since the respective distributions overlap too much (see Fig. 3.5). Two procedures were applied to extract $N^{^A_ZX}$(total).

Fission yield database method:

The first one can be called fission-yield-database-method. The total number of implanted ions was determined by measuring the volume of the respective mass distribution. This also includes the isotopes in isomeric states. Then the number of one specific isotope was obtained by using fission yields from a database. In this work the two databases ENDF/B-VII [59] and JEFF-3.1 [101] were used. The fission yields from these two databases were mostly consistent for the isotopes investigated here, exceptions are ^{79}As, ^{85}Kr. In the calculation it is assumed that the relative fission yield values for one mass A do not depend on the fragment energy.

In the Tables 4.3-4.5 the isomer ratios obtained using this method are given in the column titled with the name of the database used. The main contribution to the uncertainty of $N^{^A_ZX}$(total) comes from the fission yield Tables. These uncertainties range from 10% to 30%.

β decay method:

As a second method, independent of the database fission yields, $N^{^A_ZX}$(total) was extracted from measured γ-intensities of transitions after β decay. The principle idea is

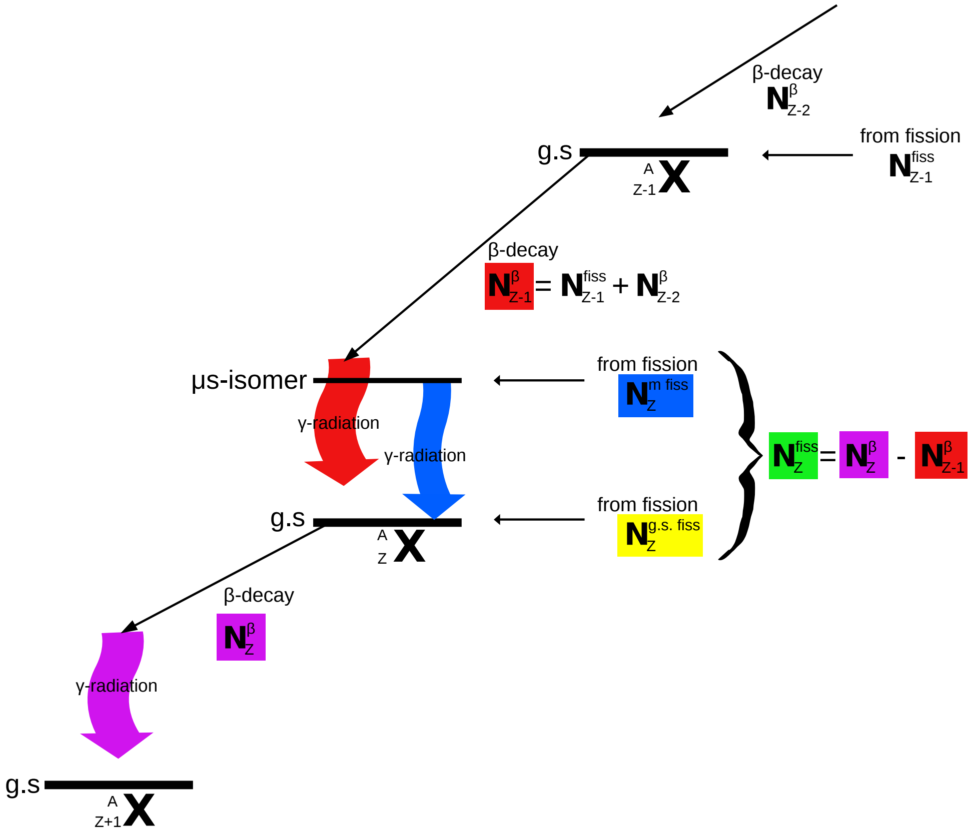

Figure 4.2: Schematic depiction of the β decay method. N^{β} is obtained by measuring the γ-radiation after β decay. By doing this for the populating (red) and depopulating (purple) β decay, N^{fiss}_{Z} can be determined. It is assumed, that not all β decay goes to the ground state (that would mean no γ rays) and that the β decay lifetimes of $^{A}_{Z}X$ and $_{Z-1}^{A}X$ are short compared to the total measuring time. See text for more details.

illustrated in Fig. 4.2. The Figure shows the population and depopulation channels of a given isotope $^{A}_{Z}X$. Fission fragments are neutron rich and undergo β decay along a mass chain until a stable isotope is reached. The number of a certain isotope $^{A}_{Z}X$ at the implantation point is increased by $^{A}_{Z}X$-ions from the beam of fragments and by β decay of the isotope $^{A}_{Z-1}X$. It is decreased by β decay of the isotope $^{A}_{Z}X$ itself. Assuming only β decay lifetimes that are negligible compared to the measuring time the following relation is valid for a given mass chain:

$$N_{Z}^{\text{fission}} = N_{Z+1}^{\beta\text{decay}} - N_{Z-1}^{\beta\text{decay}}.$$

The number of β decays of a certain isotope can be measured by measuring γ radiation after β decay. This changes the problem of counting ions with a specific atomic charge Z to measurement of γ ray intensities. The absolute γ ray transition intensities per β decay are experimentally known for most of the isotopes investigated here. For the calculations they were taken from the Nuclear Data Sheets [19, 22, 24–28, 47, 83–85].

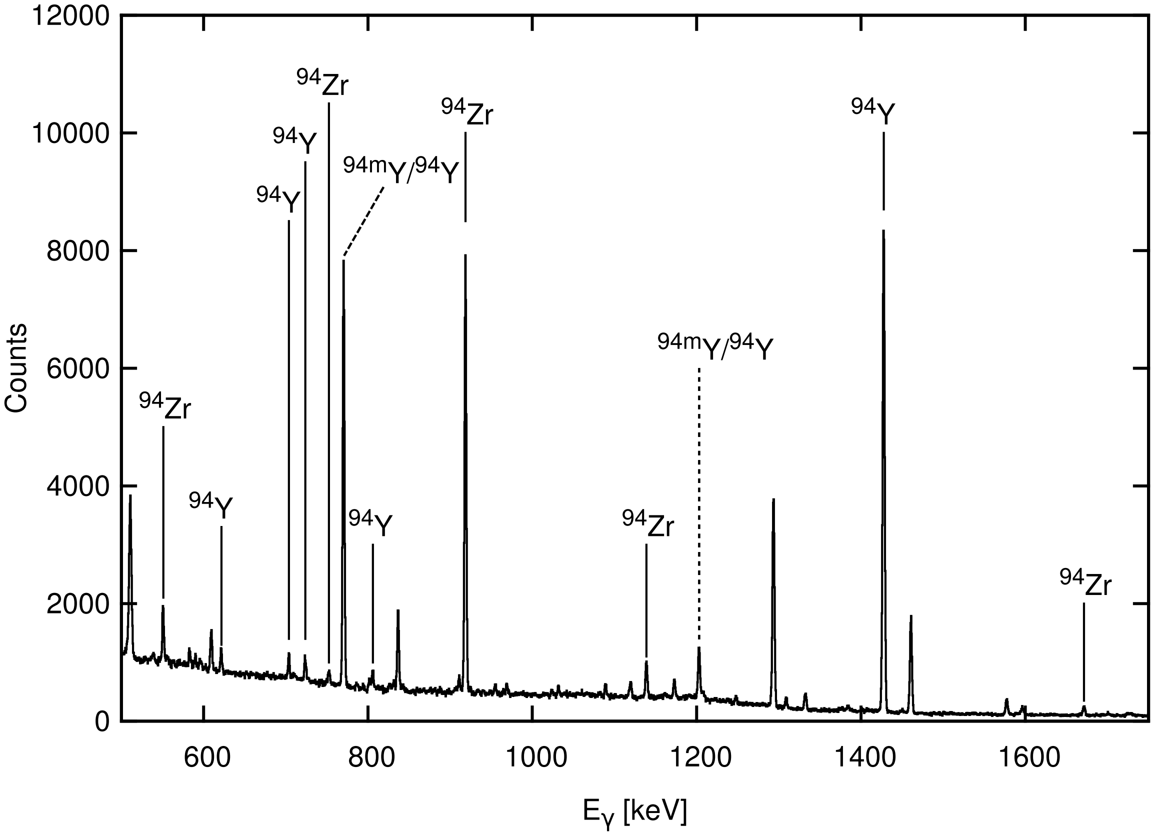

Figure 4.3: γ decay spectrum of the mass-chain A = 94. Transitions after β decay of ^{94}Sr to ^{94}Y and ^{94}Y to ^{94}Zr are labelled. These were used to determine the number of incoming ions of mass A = 94 as described in the text. Transitions which also occur after the decay of the 1202 keV μs isomer in ^{94}Y are shown with dashed lines.

So principally $N^{\beta\mathrm{decay}}$ can be obtained using the absolute efficiency calibration for the HPGe-detectors. The acquisition system uses a global first level trigger. It only records γ-radiation within a preset time-window after the detection of an ion. Because this time window is in the μs range but the β decay lifetimes are of the order of ms or longer, β decay radiation is recorded as random coincidence. The number that is measured in this way, has to be corrected by the factor $(I_{\mathrm{ions}} \cdot t_{\mathrm{timegate}})^{-1}$, where I_{ions} is the ion rate and t_{timegate} the length of the time gate. A HPGe γ ray spectrum of isotopes with mass A = 94 showing transitions after β decay and transitions from the isomeric cascade in ^{94}Y can be seen in Figure 4.3. Note, that due to the ion trigger condition no γ rays were measured if there were no incoming ions. For this reason the acquisition was always stopped when the beam was stopped. This is important if the β lifetimes in the decay chain are not negligible with respect to the measurement time. Then the number of ions is underestimated, because acquisition is stopped together with the beam, and as a consequence a substantial amount of decay radiation is not counted. For this case the equilibrium activity of the long lived isotopes can be determined from the data, and the number of nuclei in this state at the moment of stopping the acquisition can be determined and added to the uncorrected result to obtain the true $N_Z^{\beta\mathrm{decay}}$. Care must also be taken if an isotope has two β decaying levels. Then the number of β decays must be determined for each level separately.

The main contributions to the experimental uncertainty of $N^{^A_ZX}$(total) come from the absolute efficiency calibration and the absolute γ intensities per β decay taken from the Evaluated Nuclear Data Files. The latter is typically of the order of several percent, but can be as large as 30% in the case of ^{83}Kr.

4.2.2 Results

The measured isomer ratios are presented in the Tables 4.3, 4.4 and 4.5. The lifetime values as they were measured in this work were used in all cases for the time of flight correction. Only in the case of ^{97}Sr the ratio was also calculated using the lifetime reported by Hwang *et al.* [93].

Note that for some isomers one or both of the methods to obtain $N^{^A_ZX}$(total) were not applicable. These cases are discussed in the following. No significant population of the lower 308 keV isomer in ^{97}Sr after fission could be measured. All population at the implantation point could be accounted for by in-flight decay of the 830 keV isomer within the measuring uncertainty. Therefore no isomer ratio is given for this isomer. $N^{^A_ZX}$(isomer) has a large uncertainty in the case of ^{92}Y due to low statistics. Therefore only an upper limit of the isomer ratio is given for this isotope. For the μs isomer in ^{97}Zr, no isomer ratio can be determined, as it was only observed after β decay. The ground state of ^{85}Kr has a β decay halflife of several years. In this nucleus there also exists an isomer with a halflife of several hours that undergoes β decay. The ground state decays almost exclusively (>99%) into the ground state of the daughter nucleus ^{85}Rb. The next largest decay branch goes to a level at 514 keV but this decay could not be observed in the data. The transition is weak as it is, and, as a result of the long lifetime of the ^{85}Rb ground state, only few decays, compared to the actual number of nuclei, can be observed during the 44 hours the measurement lasted. As a result $N_Z^{\beta\mathrm{decay}}$ cannot be measured. In this case it was not possible to extract $N^{^A_ZX}$(total) from the data, and no isomer ratio can be given for the μs isomer in ^{85}Kr using the β decay method. In ^{98}Zr there is β decay exclusively to the ground state. Of course, without decay radiation, the β decay method is not applicable, and no isomer ratio could be determined. In the case of the very exotic nucleus ^{95}Kr no β decay data is available, which also renders the method inapplicable. In the case of ^{96}Rb the β decay measurement gave very inconsistent results, also the β decay scheme of the mother nucleus is not known. Due to these circumstances no isomer ratio based on the β decay method is given for this isotope. For ^{97}Rb no data on the β decay of the mother nucleus, ^{97}Kr, is available. That means only a lower limit for the isomer ratio can be given in this case. Fission yield databases state that ^{97}Kr and all higher Z isotopes of this mass chain are produced at a rate at least 2 order of magnitude smaller than rubidium. Considering this, the isomer ratio given is probably a good approximation. Finally, for the nuclei ^{79}As, ^{92}Y and ^{100}Nb (only for ^{233}U) there was not enough statistics to get a reasonable result.

Table 4.3: Isomeric ratios after fission of ^{233}U. The ratio given is the number of isotopes in the isomeric state over the total number of that specific isotope, produced after fission, $\mathrm{N}^{\mathrm{isotope}}_{\mathrm{isomer}}/\mathrm{N}^{\mathrm{isotope}}_{\mathrm{total}}$. The isomer ratios were calculated using fission yields from the ENDF/B-VII [59] and JEFF-3.1 [101] databases or by using beta decay intensities. For some of the observed isotopes, listed in Tab. 4.1, one or both methods were not applicable. See text for more details. Energy levels and spin and parity of the isomers are taken from the Nuclear Data Sheets [19, 22, 24–28, 47, 83–85] except in the case of ^{97}Rb, in which they are taken from this work.

				Isomeric ratio (%)		
Nucl.	I^{π}_{iso}	$E^{\mathrm{level}}_{\mathrm{iso}}$/keV	$\mathrm{E_{kin}}$ (MeV)	ENDF	JEFF	β decay
^{79}As	$(9/2)^+$	773	94	26(9)	10(3)	-
^{83}Br	$(19/2^-)$	3069	96	0.6(2)	0.5(2)	0.04(2)
^{88}Br	$(4,5^-)$	270	100	37(13)	31(11)	53(14)
^{85}Kr	$(17/2^+)$	1992	92	16(5)	23(8)	-
^{92}Y	unknown	unknown	106	<3	<6	-
^{94}Y	(5^+)	1202	106	25(8)	31(7)	18(4)
^{95}Y	$9/2^+$	1087	102	2.8(9)	2.8(8)	3.5(19)
^{98}Y	(8^-)	1181	92	2.5(9)	2.3(6)	2.4(4)
	(2^-)	496	92	12(4)	11(3)	12(1)
^{98}Zr	(17^-)	6603	92	14(4)	9(2)	-
^{100}Nb	8^-	420+x	106.5	4.7(17)	3.2(9)	-

Table 4.4: Isomeric ratios after fission of ^{235}U. See caption of Tab. 4.3 and text for more details. *: In this line the half life for the flight time correction was not taken from this work, but from [93].

				Isomeric ratio (%)		
Nucl.	I^{π}_{iso}	$E^{\mathrm{level}}_{\mathrm{iso}}$/keV	E_{kin} (MeV)	ENDF	JEFF	β decay
^{88}Br	(4,5$^-$)	270	86	26(8)	24(6)	26(4)
			101	24(11)	23(12)	40(20)
^{85}Kr	(17/2$^+$)	1992	88	1.3(6)	6.8(28)	-
^{95}Kr	(7/2$^+$)	196	97	76(26)	54(20)	-
^{96}Rb	(10$^-$)	1135	97	4.3(25)	5.7(16)	-
^{97}Rb		<90	87	4.7(20)	6.3(25)	>3
^{97}Sr	(9/2$^+$)	831	78	6.8(23)	6.9(20)	10.9(19)
			95	13.2(45)	13.3(39)	12.9(22)
			95	117(42)	118(35)	114(23)*
^{94}Y	(5$^+$)	1202	106	25(8)	33(13)	27(9)
^{95}Y	9/2$^+$	1087	97	30(10)	29(10)	13(2)
^{100}Nb	8$^-$	420+x	102	1.2(4)	1.0(2)	0.9(8)

Table 4.5: Isomeric ratios after fission of ^{241}Pu. See caption of Tab. 4.3 and text for more details.

				Isomeric ratio (%)		
Nucl.	I^{π}_{iso}	$E^{\mathrm{level}}_{\mathrm{iso}}$/keV	E_{kin} (MeV)	ENDF	JEFF	β decay
^{97}Rb		<90	94	5(2)	7(3)	>7
^{97}Sr	(9/2$^+$)	831	94	16(5)	16(4)	27(5)

4.2.3 Conclusion

Production ratios of μs isomers after fission induced by thermal neutrons were measured in 13 light fission fragments for the first time. Results were obtained for three different fission targets, ^{233}U, ^{235}U and ^{241}Pu, and for different kinetic energies of the products. Two methods have been used to determine the total number of registered fission products. One based on existing databases for independent fission yields, and one based on the analysis of β decay radiation. In the cases where both methods were applicable they gave consistent results. Exceptions are ^{83}Br (^{233}U), ^{95}Y (^{235}U) and ^{97}Sr (^{241}Pu). There are cases where the β decay method seems to be more consistent with one of the two databases used to retrieve the relative fission yields than with the other. But in all of these cases the experimental uncertainty is too large to give conclusive results concerning this matter.

As mentioned in the discussion of the 831 keV isomer in ^{97}Sr (see Section 4.1) there are conflicting values for the lifetime of this state. Table 4.4 shows the isomer ratio of this isomer, once calculated using the half life value from this work, $T_{1/2} = 0.52(1)$ μs, and once using that reported by Hwang *et al.*, $T_{1/2} = 0.26(3)$ μs [93]. The shorter lifetime value results in an isomer ratio larger than 100%, which is impossible. This fact supports the longer lifetime value. Yet an isomer ratio close to, but below 100 % still lies within the experimental uncertainty for the shorter lifetime, so the conflict cannot be dissolved concludingly with this data. By demanding an isomer ratio $R_{\text{isomer}} < 1$ within the measurement uncertainty, an upper limit of $T_{1/2} > 0.26$ μs can be obtained for the 831 keV isomer in ^{97}Sr. It should be remarked that the 830 keV isomer is the yrast $9/2^{+}$ state. The band on top is the positive parity yrast rotational band up to its highest lying assigned state at 2849.5 keV with spin $23/2^{+}$ [19]. Considering this, a high population after fission of several 10% is possible, as yrast states are predominantly fed after fission. Still a population so close to 100% seems unlikely.

Chapter 5

Nuclear structure model calculations and discussion

5.1 A μs isomer in ^{97}Rb

In section 3.1 the first experimental information on excited states in ^{97}Rb are reported. A delayed E1 transition with an energy of 76.8(2) keV was unambiguously assigned to originate from the isotope. Energy and lifetime were later confirmed in a measurement at RIKEN [102]. The only other published information concerns the ground state. A spectroscopic quadrupole moment $Q = +0.58(4)$ eb and a spin of $J = 3/2$ was determined in a laser spectroscopy experiment [103]. The parity $\pi = +$ was assigned on basis of a measured magnetic moment of $\mu = +1.841(2)\mu_N$ [103], which allows for an identification of the ground state with the $\pi 3/2^+[431]$ Nilsson state. Recently the nucleus was also investigated in a Coulex experiment at REX ISOLDE [104]. The preliminary result of this measurement is observation of a rotation like ground-state band, along with several other rotational bands. The experiment was not sensitive to μs isomers and so it is not surprising that the 76.8 keV transition was not observed. There is however a 68 keV transition to the ground state. In the data of this work, there are hints for a transition at this energy, but it could not be established with reasonable statistical significance. This section will first discuss some nuclear structure features of the mass region. Then some possible origins of a low-lying μs isomer in ^{97}Rb will be discussed.

As reviewed in Section 1.6, neutron-rich nuclei in the mass region $A \approx 100$ exhibit a sudden shape transition at neutron number $N = 60$ (see e.g. Figure). This structural change can also be observed in the rubidium isotopic chain. Data on static quadrupole ground state deformation (Figure 1.6) and two neutron separation energy, and also experimental evidence for rotational bands [104], show clear signs for a sudden transition from a spherical configuration with low collectivity and dominantly low-lying single quasi particle states to a strongly deformed one, exhibiting collective excitation patterns at low energy. Shape coexistence is reported for ^{99}Y, where a state at 599 keV is proposed to have spherical structure, opposed to all other low-lying excited states. Another feature of the rapid shape transition is the prediction of prolate-oblate shape coexistence by theoretical calculations [44].

The question is of course, what kind of mechanism is responsible for a low-lying isomer in ^{97}Rb. If the 76.8 keV transition is a ground-state transition, a K isomer character can instantly be ruled out due to the measured E1 multipolarity. In this case a reduced transition strength of B(E1) = $1.2(1) \times 10^{-7}$ W.u. can be deduced.

This reduced transition strength can be compared to results from calculations made in the quasi particle rotor model, which is described in Section 1.3. These calculations were performed by G. Simpson and published in the same article as the results from Section 3.1 [69]. The ground state is assumed to have a $3/2^+[431]$ configuration [103]. A ground state quadrupole deformation of $\epsilon_2 = 0.29^{+2}_{-4}$ was extracted from the measured spectroscopic quadrupole moment [103]. As there is no evidence for pronounced higher order deformation in nuclei close to ^{97}Rb, these were fixed to be zero. Coriolis mixing was taken into account, and an attenuation factor of 0.5 was used. A standard BCS approximation was employed to account for pairing correlations. The moment of inertia was taken as 80% of the rigid-body for given deformation. More details on the calculation can be found in [69].

Table 5.1: Composition of low-lying one quasi particle states with negative parity in terms of spherical oscillator shells. States with amplitudes smaller than 5% are not shown. The composition values are the result of a QPRM calculation and taken from [69].

QP state	ϵ_2	$1f_{5/2}$	$2p_{3/2}$
$3/2^-[321]$	−0.20	98.5	
$1/2^-[321]$	−0.20	12.4	85.2
$3/2^-[312]$	0.29	85.3	9.9

Low lying negative-parity states appear for both prolate and oblate deformations. The reduced strengths for transitions to the $3/2^+$ ground state were calculated for these states. For a prolate deformation of $\epsilon_2 = 0.29$ one finds $3/2^-[312]$ with B(E1) = 2.5×10^{-7} W.u., $3/2^-[301]$ with B(E1) = 5.8×10^{-6} W.u., and $1/2^-[310]$ with B(E1) = 3.1×10^{-5} W.u. For an oblate deformation of $\epsilon_2 = -0.20$ one finds $1/2^-[321]$ with B(E1) = 2.2×10^{-7} W.u., $3/2^-[321]$ with B(E1) = 1.8×10^{-6} W.u., and $1/2^-[310]$ with B(E1) = 4.1×10^{-3} W.u. Based on these transition strength estimates, the prolate $3/2^-[312]$ and the oblate $1/2^-[321]$ and $3/2^-[321]$ quasi particle states can be considered the most likely candidates for a low-lying negative parity isomer in ^{97}Rb with a 76.8 keV ground-state transition. Note, that the transition strengths in the oblate case assume an oblate ground state. The present code was not able to calculate transition strengths between states with different deformations. Table 5.1 shows the oscillator shell composition of these three quasi particle states as they result from the calculation. The ground state is dominated by $g_{9/2}$. This can explain the strong retardation in B(E1) shown above, as E1 transitions between the two oscillator orbitals $f_{5/2}$ and $p_{3/2}$ and the $g_{9/2}$ orbital are j forbidden.

It is worth noticing that no $5/2^-$ states appear at low energies in these calculations. The same is the case in recent Hartree-Fock-Bogoliubov (HFB) + microscopic collective Bohr Hamiltonian calculations, performed by J. M. Daugas *et al.*, also published in [69].

Based on this result spin and parity of the isomer can be restricted to $(1/2, 3/2)^-$ in this scenario. Beyond mean field calculations, also presented in [69], which reproduce the general results of HFB calculations mentioned above, predict very low-lying oblate $1/2^-$ and $3/2^-$ states in ^{97}Rb, comparable also to the results in [44]. So in this scenario the isomer is possibly a shape isomer.

The level energy of the isomer can be restricted to $E_{\mathrm{iso}} < 90$ keV based on the data from this work. That means, next to the scenario of a single ground-state transition, the possibility of a cascade including one or more very low energy transitions cannot be excluded. Two scenarios are possible. One, where an unobserved low energy transition (or several) populates a state at 76.5 keV which then decays to the ground state. In this case the 76.5 keV state is not necessarily a μs isomer. Spin and parity are restricted to $(1/2, 3/2, 5/2)^-$ due to the E1 character of the 76.5 keV γ. The scenario in which a state at 76.5 keV is fed by a low energy transition is unlikely. Based on the observed halflife, such a transition should have a multipolarity E1, M1 or E2, otherwise a much longer half life would occur. The possible spin parity assignements of such a state would favor decay directly to the ground state. However, the 76.5 keV line does not show any asymmetries, and no other transitions are observed. The other scenario, in which the 76.5 keV transition feeds a low lying state, can be excluded by comparison to the QPRM model calculations and the available low-energy states. No states at low enery are predicted, for which feeding with an E1 transition is more likely than for the ground state.

5.2 Structure of the 522 keV state in ^{97}Sr

A new decay transition from the 830 keV μs isomer of ^{97}Sr with an energy of 308.3(2) keV was observed in this work (see Section 3.2). From coincidence data it could be concluded that it populates a state at 522 keV. This state was previously observed in measurements of the ^{97}Rb β decay. There the 522 keV level is populated by an M1 transition from a $5/2^+$ state at 687 keV. The strongest decay is a 355 keV M1 transition to the first excited state at 167 keV, which has a measured spin, parity of $3/2^+$. This restricts the possible spin and parity of this state to be $3/2^+$ or $5/2^+$. This is in accordance with the measured $\log ft$ value for the population of this state from the $3/2^+$ ground state of ^{97}Rb. The new feeding transition from the $9/2^+$ isomeric state now allows to exclude $3/2^+$ and to assign $(5/2)^+$ as the spin and parity value for the 522 keV state. A partial halflife $T_{1/2}^{\mathrm{part.}} = 17(8)\mu$s for the 308 keV transition is calculated from branching ratios and the lifetime measured for the 830 keV isomer in this work. This corresponds to a reduced transition probability B(E2) of 0.00045 W.u. for an E2 and 29236 W.u. for an M3 transition. There is no reason for such an enormous enhancement of M3 strength, especially considering the isomeric character of the transition. This possibility can therefore be discarded, which on the other hand excludes $J = 3/2$ for the 522 keV level.

The ground state and first excited state of ^{97}Sr are spherical or merely very weakly deformed [75]. The ground state is assigned a dominant neutron $s_{1/2}$ character based on laser spectroscopy measurements [105]. Deformed excited states, along with rotational bands on top of them, have been established for this nucleus [106, 107]. The band head of the lowest lying one at $E = 585$ keV is interpreted as a state with a Nilsson configuration $3/2^+[411]$ [75]. The isomeric state at 830 keV is also deformed, with a proposed $\nu 9/2^+[404]$ quasi particle configuration [93, 43]. It is worth noting, that this state was first observed in ^{99}Zr at an energy of 1038.5 keV [108]. The up sloping $9/2^+[404]$ orbital slows down the increase of ground state deformation at N=58 and N=59, but leads to highly deformed excited neutron hole states similar to the $11/2^-[505]$ orbital in the A=140 mass region [43].

The spin assignment of $(5/2)^+$ to the 522 keV state makes it the yrast state with this spin in ^{97}Sr. The closest other $5/2^+$ states are a deformed state at 687 keV and a state at 601 keV, which is interpreted as a quadrupole phonon coupled to the ground state $(1/2^+ \otimes 2^+_{\text{phonon}})$ [109]. If the 522 keV state was deformed, the band on top of it would also be yrast. The experiments in which deformed band members were observed all used fission to produce ^{97}Sr, which strongly populates yrast states. It seems therefore unlikely that a rotational band on the lowest lying deformed state should have gone unobserved in these measurements. By rejecting a pronounced collective nature of the 522 keV state, the first assumption should be that it is a quasi particle excitation. It is possibly a high seniority shell model state, as already suggested in [69]. In an IBFM calculation Lhearsonneau *et al.* found the ground state and second excited state, $1/2^+$ and $7/2^+$, to have rather pure 1-QP configurations, while the first excited state, a $3/2^+$ state at 167 keV, is more complex [75]. A similar structure is possible for the $5/2^+$ state. In this article the level at 522 keV was identified as a $3/2^+$ spherical state that appeared at 540 keV in the IBFM calculation. This interpretation has to be questioned with the new spin assignment.

Table 5.2: Parameters of the IBM calculation of ^{96}Sr, shown in Figure 5.1. These parameters are used for the boson core in the IBFM calculation for ^{97}Sr.

N_B	ϵ_d	PAIR	ELL	QQ	χ_B
9	0.82	0.005	0.023	-0.014	-0.7

In order to find out more about the structure of the 522 keV state, a new IBFM calculation was performed. The IBM calculation for the boson core was performed using the program *phint* [12]. The Hamiltonian is that of equation (1.15). The parameters were adjusted to fit the low energy states of the neighbouring ^{96}Sr. Note that the 0^+_2

state at $E = 1229.3$ keV is interpreted as an intruder state [106] and was not included in the fit. Figure 5.1(left) shows a comparison of the calculated values with data from the nuclear data sheets [19]. The parameters are shown in Table 5.2. ^{96}Sr has a spherical ground state. The excitation spectrum shows signs of vibrational character ($R_{4/2} = 1.8$). It should therefore most closely exhibit the U(5) dynamical symmetry of the IBM-1, which describes vibrational nuclei. For this reason an IBFM fit with the core in the U(5) limit ($\epsilon_d = 0.815$, all other parameters turned off) was also attempted. However it was not possible to reproduce the low energy of the $3/2^+_1$ in ^{97}Sr with a value of $\chi_{BF} = 0$. It can be concluded, that this limit is no good description for ^{97}Sr while it still gives a reasonable description of ^{96}Sr. This is not really surprising, as the nuclei with N = 59 in this region are known to have a transitional structure (see also Section 1.6). In the IBFM fit presented here, $\hat{\mathrm{n}}_d$ still dominates the collective excitations of the core, due to a rather high ϵ_d. Therefore the word phonon will be used in the discussion, even though the IBM wave functions are more complex. The program *oddA* [110] was used to perform the IBFM calculation, as described in Section 1.4. Single particle energies were adjusted based on [14] and are given in Table 5.3. The single particle energy $\epsilon(\mathrm{g}_{7/2})$ was set below $\epsilon(\mathrm{d}_{3/2})$. Pairing was accounted for by using a BCS approximation [10] to calculate the population probability in the $\mathrm{d}_{5/2}$, $\mathrm{g}_{7/2}$, $\mathrm{s}_{1/2}$, $\mathrm{h}_{11/2}$, $\mathrm{d}_{3/2}$ neutron shell. The occupancy for the nine valence neutrons of ^{97}Sr are shown in Table 5.3 along with the resulting gap and Fermi energy (caption). The single particle energy differences of $\epsilon(s_{1/2})$, $\epsilon(g_{7/2})$, and $\epsilon(d_{3/2})$ are close to those used for the IBFM calculation in [75] ($\epsilon(g_{7/2}) - \epsilon(s_{1/2}) = 0.9$ MeV, $\epsilon(d_{3/2}) - \epsilon(s_{1/2}) = 1.2$ MeV). Note that in [75] the $\nu\mathrm{d}_{5/2}$ orbital was considered fully occupied and therefore not included. It was however included in the present calculation, which of course has a huge influence on the result, especially the $5/2^+$ states. The three parameters for the quasi particle part and the boson-fermion coupling part (see Section 1.4) were adjusted to the first four states of ^{97}Sr. A best fit was achieved with the parameter set $A_0 = 0.50$, $\Lambda_0 = 0.11$, and $\Gamma = 0.31$. The value of χ_{BF} in V_{BF} was set to the same value as $\chi_B = -0.7$. The results of the calculation for states with an excitation energy E< 1.2 MeV are shown in Figure 5.1, along with the experimentally known states. All states higher than the $5/2^+_1$ are predicted at too high an excitation energy. In the present calculation the $7/2^+_1$ state is a rather pure $\mathrm{g}_{7/2}$ 1-QP excitation coupled to the

Table 5.3: Single particle energies used in the BCS approximation for the IBFM calculation. The resulting Fermi energy is $\epsilon_{\mathrm{Fermi}} = 1.191$ MeV, the gap is $\Delta = 1.343$ MeV. The resulting occupancy for the single oscillator shells are also shown.

	$\mathrm{d}_{5/2}$	$\mathrm{g}_{7/2}$	$\mathrm{s}_{1/2}$	$\mathrm{h}_{11/2}$	$\mathrm{d}_{3/2}$
ϵ(MeV)	0.0	2.71	1.4	2.55	2.9
ν^2	0.832	0.125	0.423	0.144	0.107

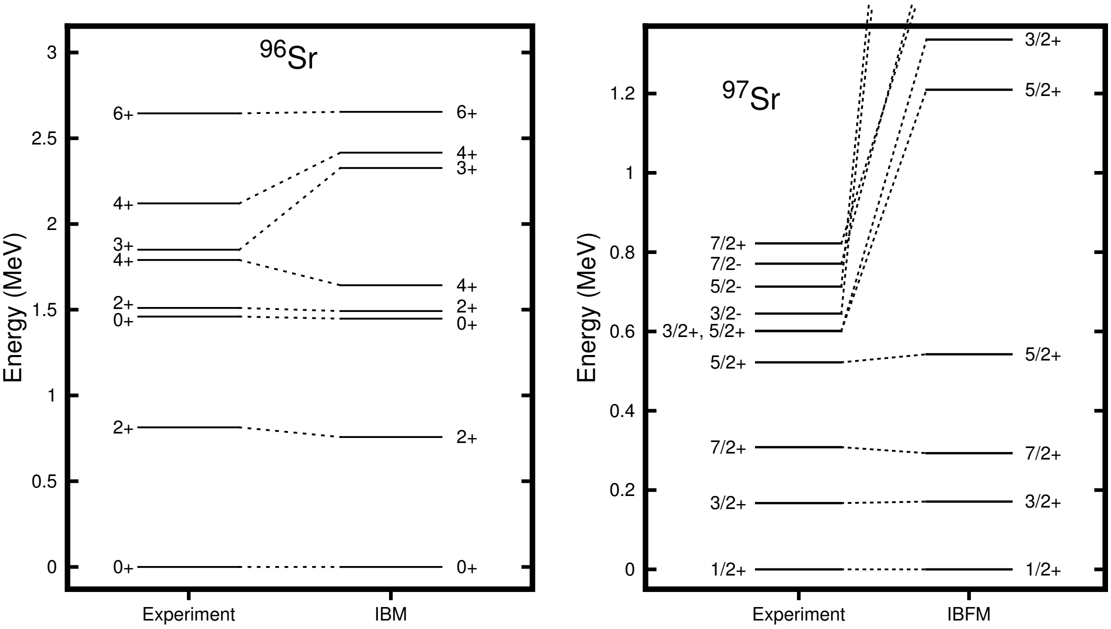

Figure 5.1: (left) Comparison of experimental data with calculations for ^{96}Sr in the IBM. The same set of parameters (see Table 5.2) is used for the IBM core of the IBFM calculation of ^{97}Sr, shown on the right. Note the different energy scales. See text for more details.

IBM ground state. The lowest $5/2^+$ state is predicted at 543 keV, with a dominant $\mathrm{d}_{5/2}$ neutron quasi particle configuration coupled to the IBM ground state. This simple 1-QP configuration relies on an inclusion of the $\nu\mathrm{d}_{5/2}$ shell model orbital in the model space.

The lowest $3/2^+$ state is predicted with a much more simple quasi particle configuration than in [81], but still with a large $\mathrm{g}_{7/2}$ component of about 23%. The main contribution to the wave function comes from a $\mathrm{d}_{3/2}$ QP coupling to the IBM ground state, the amplitude of the QP-phonon configuration $(\mathrm{g}^+_{7/2} \otimes 2^+_{\mathrm{phonon}})$ is about half of that. As mentioned in [75], the low energy of the first $3/2^+$ is possibly due to the "I=j-1, j-2 anomaly" (see Chapter 6 in [1]) for quasi particles coupling to a quadrupole phonon. This reduces the energy of the coupling to the $\mathrm{g}_{7/2}$ QP. In [109], the state at 601 keV, with a spin of $3/2^+$ or $5/2^+$, was identified as a 2^+ phonon coupled to the $1/2^+$ ground state, forming a state with spin $J = 5/2^+$. This is principally verified in the present calculation, where the second excited $5/2^+$ state is dominated by such a configuration. But the state appears at 1.2 MeV, which is double the value of the experimentally found energy. The next lowest state with predominant $(\text{g.s.} \otimes 2^+_{\mathrm{phonon}})$ configuration is the second excited $3/2^+$ state at 1.34 MeV (see also Figure 5.1).

It was not possible in the calculation to reproduce the four lowest energy states and the higher lying states, shown in Figure 5.1, simultaneously. This can be interpreted as a boson core character of ^{97}Sr that is significantly different to that of ^{96}Sr. The predicted phonon excitations of the ground state, the $5/2^+_2$ and the $3/2^+_2$, lie at an energy that approximately corresponds to the sum phonon energy ϵ_d and the quasi particle energy, as expected for a vibrational nucleus. This can be interpreted as a sign for the transitional character of ^{97}Sr with neutron number N = 59. It could also hint to a different intrinsic core structure of these two sets of states. Recalling the existence of a deformed 0^+ intruder state in ^{96}Sr, these excitations are possibly QP excitations in a deformed minimum. A configuration mixing calculation including transition rates for this nucleus would be very insightful. If the states lie this close together it can be estimated, that mixing is weak.

Concludingly it can be said that, on basis of this calculation, the $5/2_1^+$ state at 522 keV can be interpreted as a QP excitation if the $d_{5/2}$ orbital is incorporated. It then has a structure similar to that of the $7/2_1^+$ state. The branching ratios for the 522 keV level are consistent with this interpretation.

5.3 Transitions in the K=5/2 and K=11/2 bands in ^{99}Y

The structure of ^{99}Y was already studied by many groups. Rotational bands have been identified and characterised [111]. The ground state is a $5/2^+$ state with a Nilsson configuration $5/2^+[422]$ and a K=5/2 rotational band is built on top of it [78]. It has a spectroscopic quadrupole moment $Q = 1.55(17)$ [112], which corresponds to a quadrupole deformation $\beta_2 = 0.4$. This value is close to the maximum deformation found in this region, e.g. in ^{98}Sr $\beta_2 = 0.41$. The first excited state belongs to the ground state rotational band and has spin parity $7/2^+$. Its lifetime was measured to be $T_{1/2} = 57(10)$ ps in this work, which agrees well with the previously measured value of $T_{1/2} = 47(6)$ ps [113]. The lifetimes of the second and an upper limit for the third excited state were measured in this work for the first time (see Table 3.3). Table 5.4 shows the transition quadrupole moments Q_t for these states, calculated with the formula

$$Q_t^2 = \frac{16\pi}{5} \begin{pmatrix} J & 2 & (J-2) \\ K & 0 & K \end{pmatrix}^{-2} B(\mathrm{E2}),$$

where the bracket is the Wigner 3j-symbol. Q_t for the $7/2_1^+$ state was determined using the measured multipole mixing ratio $\delta = 0.53$ [77]. The other two were calculated from the pure E2 transitions from the $9/2_1^+$ to the ground state and from the $11/2_1^+$ to the $7/2_1^+$ state. The branching for these transitions was taken from [77]. The deduced Q_t values agree well with the prediction of the geometric model of a constant transition quadrupole moment in rotational bands at low spins [1].

No B(E2) or Q_t value can be deduced for the $13/2_2^+$ state, because the mixing ratio is unknown. The μs isomer at 2142 keV is assigned a spin parity of $17/2^+$ and a three-quasi-particle configuration $(\pi 5/2[422] \otimes \nu 3/2[4ll] \otimes \nu 9/2[404])$.

A calculation of excited states and transition strengths for ^{99}Y was performed using the quasi particle rotor model (see Section 1.3) with the computer codes *gampn*, *asyrmo*, and *probamo* [9]. Standard parameters were for the $l \cdot s$ and $l \cdot l$ coupling strength, μ and κ [114]. Pairing correlations were taken into account by a standard BCS approximation. The Fermi surface and paring gap Δ are then calculated by the program. A deformation

Table 5.4: Transition quadrupole moments of excited states in the K=5/2$^+$ ground-state band of ^{99}Y calculated from measured halflives.

	E_γ (keV)	τ (ps)	B(E2) (e^2b^2)	Q_t (eb)
$7/2_1^+$	125	82(14)	4.89	1.57(27)
$9/2_1^+$	284	29(6)	0.24	1.2(4)
$11/2_1^+$	357	<22	>0.19	>0.96

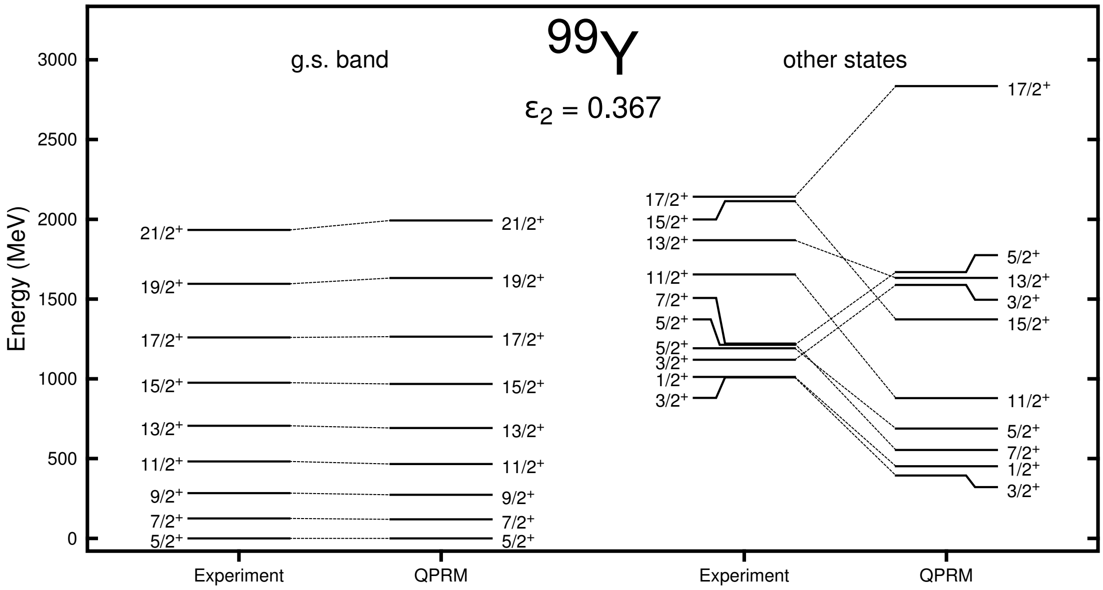

Figure 5.2: Experimental excitation energies of positive parity states in ^{99}Y. Comparison with a calculation in the quasi particle rotor model. In this calculation $\epsilon_2 = 0.367$ and E2PLUS = 0.14 MeV. See text for more details.

of $\epsilon_2 = 0.37$ was extracted[1] from a measured ground state spectroscopic quadrupole moment of $Q = 1.55(17)$ [112] and used as the parameter for the deformed core. All higher order deformations were set to zero. γ was set to zero as well. Previous studies showed that, in contrast to rhodium and technetium isotones, ^{99}Y exhibits axially symmetric deformation. Eleven quasi particle states around the Fermi surface were used in the coupling to the rotor core. The moment of inertia parameter, an effective core 2_1^+ energy E_{2^+}, is the only parameter that was adjusted to fit the data. This value is essentially a scaling factor. A good agreement with the experimental ground-state band energies was achieved using $E_{2^+} = 0.14$ MeV. No Coriolis attenuation was applied. With these settings a good reproduction of the ground-state band was achieved, as can

---

[1] The quadrupole deformation parameter ϵ_2 is used as input for the computer code, not β_2. The two are related via $\epsilon_2 \approx 0.944\beta_2 - 0.122\beta_2^2$ for $\beta_4 = 0$.

be seen in Figure 5.2. All other states, however, are not reproduced well. This is true for the excitation energy, as well as for the level ordering. The result for the ground-state band is very similar to that found in [78] with the same parameters, except $\epsilon_2 = 0.41$. Unlike in the present calculation the deformation was also used as a fit parameter. The ground state is a $5/2^+$ state with the Nilsson configuration $5/2^+[422]$. The main objective of the calculation was the determination of transition strength, in order to compare them to the newly measured values. For magnetic dipole matrix elements, standard effective g factors were chosen: effective spin g factor $g_s = 0.6 g_{\text{free}}$, core g factor g_R = Z/A. The ground state magnetic moment is calculated to be $\mu = 2.9\ \mu_0$, which is in fair agreement with the measured value of $\mu = 3.18(2)\ \mu_0$ [112]. A comparison of the predicted lifetimes with the ones extracted from the data measured in this work is shown in Table 5.5 (QPRM1). These values show reasonable agreement within the ground-state band and for the $13/2^+_2$ state.

Table 5.5: Comparison of lifetimes of states in the K=$5/2^+$ ground-state band in ^{99}Y measured in this work with values from a quasi particle rotor calculation. Theoretical lifetimes include a correction for internal conversion.

	E_{level} (keV)	τ_{exp} (ps)	τ_{QPRM} (ps)
$7/2^+_1$	125	82(14)	144
$9/2^+_1$	284	29(6)	31
$11/2^+_1$	482	<22	7
$13/2^+_2$	1869	23(6)	15

Another calculation was attempted with a smaller deformation and higher E_{2^+} energy ($\epsilon_2 = 0.307$, $E_{2^+} = 0.18$ MeV). This led to a better reproduction of the K=11/2 band in terms of level energy and ordering. However, the predicted intra-band transition rates were almost an order of magnitude too low in comparison to experimental data.

5.4 Deformation in ^{100}Nb

It was suggested in [115] that a rotational band based on the 1^+ ground state exists in the odd odd nucleus ^{100}Nb. The nucleus has neutron number N = 59. In neighboring isotopic chains, the nuclei at N = 59 have spherical ground states with single particle excitations up to about 500 keV. Only above this energy, rotational bands are observed. This is for example the case in ^{97}Sr, as discussed in Section 5.2. A deformed ground state with well developed rotational bands, as proposed in [115] would call for an obliteration of the N = 56 subshell closure already at N = 59, in contrast to the direct neighbors zirconium and molybdenum.

In this context the lifetimes of states populated after the decay of the (8^-) μs isomer situated 421 keV above the (5^+) ms isomer were measured (see Section 3.4). These states are not identified with any of the states assigned to the ground-state band in [115]. The state at 207 keV above the (5^+) isomer decays via a pure M1 transition [79]. The measured lifetime of $\tau = 299(20)$ ps allowed to determine the reduced transition strength B(M1) $= 0.0349\ \mu_N^2 = 0.0195$ W.u. This hints at a non-collective nature of the states in the isomeric decay.

5.5 Conclusion

In this thesis, new experimental data on excited states in the neutron-rich nuclei ^{97}Rb, ^{97}Sr, ^{99}Y, and ^{100}Nb were gathered. A new μs isomer at low excitation energy $E < 90$ keV was observed in ^{97}Rb. The halflife was measured to be 5.1(4) μs. Its decay cascade involves a transition with energy $E_\gamma = 76.8$ keV. The multipolarity of this transition was determined to be E1 based on the measured K-conversion coefficient. If the transition is a ground-state transition, the spin and parity of the state can be restricted to $(1/2,\ 3/2,\ 5/2)^-$. A comparison to calculations in various models hints at a spin of $1/2^-$ or $3/2^-$. The hindrance of the transition can be explained by the quasi particle Nilsson configurations of the ground state and possible low-lying negative-parity states. Some models also predict low-lying oblate negative-parity states. The isomer is possibly an oblate shape isomer.

A new decay branch in the K=$9/2^+$[404] isomer in ^{97}Sr, populating the level at 522 keV, was established. This allows a spin assignment of $J^+ = 5/2^+$ for this state. Calculations in the interacting boson fermion model indicate a simple one-quasi-particle structure of this state.

Lifetime measurements in the neutron-rich nuclei ^{99}Y and ^{100}Nb were performed using the γ-γ delayed coincidence method. The data were analyzed using the generalized centroid shift method. Three new lifetimes of deformed states in ^{99}Y were measured. These give further evidence for the regular rotational structure of the ground-state band in this nucleus. Transition quadrupole moments, derived for the ground-state band, show the expected constant behavior. A calculation in the quasi particle rotor model, assuming axially symmetric deformation, yielded good agreement for the ground-state band using a deformation of $\epsilon_2 = 0.37$. The lifetime measurements in the decay cascade of the μs isomer in ^{100}Nb indicate non-collective nature of these excitations.

5.6 Outlook

The measurements performed within the scope of this thesis delivered new data on nuclei in the interesting region of the shape transition of neutron-rich nuclei at neutron number N = 60. For the first time, the $\gamma\ \gamma$ delayed coincidence technique was used to measure lifetimes in the picosecond region of very neutron-rich fission fragments. The results show that precise results can be obtained with the generalised centroid difference (GCD) method from a small array of four LaBr detectors. Even though background contributions were not negligible, and the source was not point-like, it was possible to extract lifetimes in the order of 10 ps in ^{100}Mo and ^{99}Nb, which agree with literature values. This shows the power of the GCD method and gives a positive signal for the application of this technique under even tougher experimental circumstances, like, e.g., with radioactive ion beams.

It would certainly be interesting to investigate closer the isomer in ^{97}Rb. It appears at a very low excitation energy and possibly has an oblate deformation. Theoretical calculations predict prolate-oblate shape coexistence in rubidium isotopes. A verification of this is possible by observing the rotational band on top of the isomer. This might be possible from the (n,fission) data collected in the EXILL campaign earlier this year (2013). The isomer is quite strongly populated in fission and the knowledge about the 76.5 keV transition gives a hint where to look for transitions in this possible band in $\gamma\ \gamma$ coincidence data.

The indications for the non-collective nature of a state with excitation energy of about 500 keV, populated in the isomer decay in the transitional nucleus ^{100}Nb with neutron number N = 59, agree with a comparison of neighbouring nuclei at this neutron number. The assignment of a rotational band based on the ground state of this nucleus should be investigated further, because it seems to contradict the present understanding of this transitional region.

List of Figures

List of Tables

References

[1] A. Bohr and B.R. Mottelson. *Nuclear Structure, Volume 2*. W.A. Benjamin, Inc., 1975.

[2] R.F. Casten. *Nuclear Structure from a Simple Perspective*. Oxford University Press, 1990. ISBN 0 19 850724 0.

[3] A. Bohr and B.R. Mottelson. *Nuclear Structure, Volume 1*. W.A. Benjamin, Inc., 1969.

[4] J.M. Blatt and V.F. Weisskopf. *Theoretical Nuclear Physics*. John Wiley and Sons, 1952. ISBN 0-387-90382-8.

[5] K.S. Krane. *Introductory Nuclear Physics*. John Wiley and Sons, 1988. ISBN 047180553X.

[6] T. Kibédi and T.W. Burrows and M.B. Trzhaskovskaya and P.M. Davidson and C.W. Nestor Jr. Evaluation of theoretical conversion coefficients using BrIcc. *Nuclear Instruments and Methods in Physics Research Section A: Accelerators, Spectrometers, Detectors and Associated Equipment*, 589(2):202 – 229, 2008.

[7] K. Heyde. *The Nuclear Shell Model*. Springer Verlag, Berlin, 1990.

[8] R.B. Firestone, S.Y.F. Chu, and C.M. Baglin. *Table of Isotopes, 8th Edition*. John Wiley & Sons, Inc., 1998.

[9] P. Semmes and I. Ragnarsson. *The particle + triaxial rotor model: A user's guide*. 1992.

[10] P. Möller and J.R. Nix. The Nuclear Pairing Models. *Nucl. Phys. A*, 536:20, 1992.

[11] A. Arima and F. Iachello. Collective Nuclear States as Representations of a SU(6) Group. *Phys. Rev. Lett.*, 35(16):1069–1072, 1975.

[12] O. Scholten. *The interacting boson approxiamtion model and applications*. Phd thesis, University of Groningen, 1980.

[13] F. Iachello and P. Van Isacker. *The Interacting Boson Fermion Model*. Cambridge University Press, Cambridge, England, 1991.

[14] L. S. Kisslinger and R. A. Sorensen. *Reviews of modern physics*, 35(4):853 – 915, 1963.

[15] P.J. Nolan and J.F. Sharpey-Schafer. The measurement of the lifetime of excited nuclear states. *Reports on Progress in Physics*, 42:1–86, 1979.

[16] Otto Hahn. Über ein neues radioaktives Zerfallsprodukt im Uran. *Naturwissenschaften*, 9(5):84–84, 1921. ISSN 0028-1042.

[17] C.F. Weizsäcker. Metastabile Zustände der Atomkerne. *Naturwissenschaften*, 24 (51):813–814, 1936. ISSN 0028-1042.

[18] Philip Walker and George Dracoulis. Energy traps in atomic nuclei. *Nature*, 399: 35–40, 1999.

[19] N. Nica. Nuclear Data Sheets for A = 97. *Nuclear Data Sheets*, 111:525 – 716, 2010.

[20] S.-C. WU and H. NIU. Nuclear Data Sheets for A = 180. *Nuclear Data Sheets*, 100(4):483 – 705, 2003. ISSN 0090-3752.

[21] J. B. Cumming and D. E. Alburger. Search for the decay of $^{180}\mathrm{Ta}^{\mathrm{m}}$. *Phys. Rev. C*, 31:1494–1498, Apr 1985.

[22] G. Mukherjee and A.A. Sonzogni. Nuclear Data Sheets for A = 88. *Nuclear Data Sheets*, 105:419 – 556, 2005.

[23] L.P. Ekström and J. Lyttkens-Linden. Nuclear data sheets for A = 90 . *Nuclear Data Sheets* , 67(4):579 – 691, 1992.

[24] Coral M. Baglin. Nuclear Data Sheets for A = 92 . *Nuclear Data Sheets* , 113 (10):2187 – 2389, 2012.

[25] D. Abriola and A.A. Sonzogni. Nuclear Data Sheets for A = 94 . *Nuclear Data Sheets* , 107(9):2423 – 2578, 2006.

[26] D. Abriola and A.A. Sonzogni. Nuclear Data Sheets for A = 96 . *Nuclear Data Sheets* , 109(11):2501 – 2655, 2008.

[27] Balraj Singh and Zhiqiang Hu. Nuclear Data Sheets for A = 98. *Nuclear Data Sheets*, 98:335 – 513, 2003.

[28] Balraj Singh. Nuclear Data Sheets for A = 100 . *Nuclear Data Sheets* , 109(2): 297 – 516, 2008.

[29] D. De Frenne. Nuclear Data Sheets for A = 102 . *Nuclear Data Sheets* , 110(8): 1745 – 1915, 2009.

[30] AA Sonzogni. Experimental data on ground- and excited-state properties for all nuclei with mass number A=144 have been compiled and evaluated. States populated in radioactive decay as well as in nuclear reactions have been considered. For these nuclei, level and decay schemes have been built, as well as tables of nuclear properties. This work supersedes the 1989 evaluation by J.K. Tuli (1989Tu02). Manuscripts published before December 2000 have been included in this work . *Nuclear Data Sheets* , 93(3):599 – 762, 2001.

[31] L.K. Peker and J.K. Tuli. Nuclear Data Sheets for A = 146 . *Nuclear Data Sheets* , 82(2):187 – 378, 1997.

[32] M.R. Bhat. Nuclear Data Sheets for A = 148 . *Nuclear Data Sheets* , 89(4):797 – 984, 2000.

[33] S.K. Basu and A.A. Sonzogni. Nuclear Data Sheets for A = 150 . *Nuclear Data Sheets* , 114(4–5):435 – 660, 2013.

[34] M.J. Martin. Nuclear Data Sheets for A = 152 . *Nuclear Data Sheets* , 114(11): 1497 – 1847, 2013.

[35] C.W. Reich. Nuclear Data Sheets for A = 154 . *Nuclear Data Sheets* , 110(10): 2257 – 2532, 2009.

[36] C.W. Reich. Nuclear Data Sheets for A = 156 . *Nuclear Data Sheets* , 113(11): 2537 – 2840, 2012.

[37] R.G. Helmer. Nuclear Data Sheets for A=158 . *Nuclear Data Sheets* , 101(3): 325 – 519, 2004.

[38] T. Thomas, K. Nomura, *et al.* Evidence for shape coexistence in ^{98}Mo. *Phys. Rev. C*, 88:044305, 2013.

[39] L. Bettermann *et al.* Lifetime measurement of excited states in the shape-phase-transitional nucleus ^{98}Zr. *Phys. Rev. C*, 82:044310, 2010.

[40] P. Federman and S. Pittel. Unified shell-model description of nuclear deformation. *Phys. Rev. C*, 20:820–829, 1979.

[41] M. Albers *et al.* Evidence for a Smooth Onset of Deformation in the Neutron-Rich Kr Isotopes. *Phys. Rev. Lett.*, 108:062701, 2012.

[42] Kris Heyde and John L. Wood. Shape coexistence in atomic nuclei. *Rev. Mod. Phys.*, 83:1467–1521, 2011.

[43] W. Urban *et al.* The $\nu 9/2[404]$ orbital and the deformation in the a - 100 region. *Eur. Phys. J. A*, 22:241, 2004.

[44] R. Rodriguez-Guzman, P. Sarriguren, and L. M. Robledo. Signatures of shape transitions in odd-A neutron-rich rubidium isotopes. *Phys. Rev. C*, 82:061302, 2010.

[45] Coral M. Baglin. Nuclear data sheets for a = 91. *Nuclear Data Sheets*, 114(10): 1293 – 1495, 2013.

[46] Coral M. Baglin. Nuclear data sheets for a = 93. *Nuclear Data Sheets*, 112(5): 1163 – 1389, 2011.

[47] S.K. Basu and G. Mukherjee and A.A. Sonzogni. Nuclear Data Sheets for A = 95 . *Nuclear Data Sheets* , 111(10–11):2555 – 2737, 2010.

[48] Pavel Cejnar, Jan Jolie, and Richard F. Casten. Quantum phase transitions in the shapes of atomic nuclei. *Rev. Mod. Phys.*, 82:2155–2212, 2010.

[49] Jean-Marc Régis. Fast Timing with $\mathrm{LaBr_3}$(Ce) Scintillators and the Mirror Symmetric Centroid Difference Method. *Doctoral thesis, Institut für Kernphysik, Universität zu Köln*, 2011.

[50] H. Mach, R.L. Gill, and M. Moszynski. A method for picosecond lifetime measurements for neutron-rich nuclei, (1) Outline of the method. *Nuclear Instruments and Methods in Physics Research A*, 280:49 – 72, 1989.

[51] Z. Bay. Calculation of Decay Times from Coincidence Experiments. *Phys. Rev.*, 77:419–419, 1950.

[52] J. Cetnar. General solution of bateman equations for nuclear transmutation. *Annals of Nuclear Energy*, 33:640–645, 2006.

[53] J.-M. Régis *et al.* The generalized centroid difference method for picosecond sensitive determination of lifetimes of nuclear excited states using large fast-timing arrays. *Nuclear Instruments and Methods in Physics Research Section A: Accelerators, Spectrometers, Detectors and Associated Equipment*, 726(0):191 – 202, 2013.

[54] M. Moszyński and H. Mach. A method for picosecond lifetime measurements for neutron-rich nuclei: (2) timing study with scintillation counters. *Nuclear Instruments and Methods in Physics Research Section A: Accelerators, Spectrometers, Detectors and Associated Equipment*, 277(2–3):407 – 417, 1989.

[55] J.-M. Régis, G. Pascovici, J. Jolie, and M. Rudigier. The mirror symmetric centroid difference method for picosecond lifetime measurements via coincidences using very fast labr3(ce) scintillator detectors. *Nuclear Instruments and Methods in Physics Research Section A: Accelerators, Spectrometers, Detectors and Associated Equipment*, 622(1):83 – 92, 2010.

[56] O. Hahn and F. Strassmann. Über den Nachweis und das Verhalten der bei der Bestrahlung des Urans mittels Neutronen entstehenden Erdalkalimetalle. *Naturwissenschaften*, 27(1):11–15, 1939. ISSN 0028-1042.

[57] Lise Meitner and R. Frisch. Disintegration of Uranium by Neutrons: a New Type of Nuclear Reaction. *Nature*, 143:239–240, 1939.

[58] S. Bjørnholm and J. E. Lynn. The double-humped fission barrier. *Rev. Mod. Phys.*, 52:725–931, 1980.

[59] T. R. England and B. F. Rider. Evaluation and compilation of fission-product yields. *ENDF/B-VII.1*, 2011.

[60] P. Armbruster *et al.* The recoil separator lohengrin: Performance and special features for experiments. *Nuclear Instruments and Methods*, 139(0):213 – 222, 1976.

[61] ILL website. Lohengrin. *http://www.ill.eu/instruments-support/instruments-groups/instruments/pn1/description/instrument-layout/*, 2013.

[62] A. Scherillo. *Study of μs isomers in neutron rich indium and cadmium isotopes.* Doctoral thesis, Universität zu Köln, 2005.

[63] J. Genevey *et al.* First observation of low-lying excited states in the very neutron-rich ^{95}Kr. *Phys. Rev. C*, 73:037308, Mar 2006.

[64] W. Urban *et al.* *Phys. Rev. C*, 79:044304, 2009.

[65] G. S. Simpson *et al.* *Phys. Rev. C*, 74:064308, 2006.

[66] J. Genevey *et al.* Identification of μs isomers in the fission products of ^{241}Pu(n_{th}, f). *Phys. Rev. C*, 59:82–89, Jan 1999.

[67] J.-M. Régis *et al.* Sub-nanosecond lifetime measurements using the Double Orange Spectrometer at the cologne 10 MV Tandem accelerator. *Nuclear Instruments and Methods in Physics Research A*, 606(3):466 – 474, 2009.

[68] M. Rudigier, J.-M. Régis, J. Jolie, K.O. Zell, and C. Fransen. "Lifetime of the first excited state in 172W and 178W ". *Nuclear Physics A*, 847(1-2):89 – 100, 2010.

[69] M. Rudigier *et al.* Delayed γ-ray and conversion-electron spectroscopy of $A = 97$ fission fragments. *Phys. Rev. C*, 87:064317, Jun 2013.

[70] M. S. Basunia. *Nuclear Data Sheets for A = 237*, 107(2323), 2006.

[71] G.F. Knoll. *Radiation Detection and Measurement.* John Wiley and Sons, 1979. ISBN 0-471-49545-X.

[72] A. Zlomaniec *et al.* Half-life of the 830.2 keV isomer in Sr97. *Phys. Rev. C*, 72: 067302, 2005.

[73] G. Simpson *et al.* Excitation energy and deformation of the $1/2^+[431]$ intruder band in ^{107}Tc. *Phys. Rev. C*, 75:027301, 2007.

[74] C. Thibault *et al.* Hyperfine structure and isotope shift of the D_2 line of $^{76-98}$Rb and some of their isomers. *Phys. Rev. C*, 23:2720–2729, Jun 1981.

[75] G. Lhersonneau *et al.* Structure of the N = 59 Nucleus ^{97}Sr: Coexistence of spherical and deformed states. *Z.Phys.*, A337:149, 1990.

[76] K.-L. Kratz *et al.* The beta-decay of ^{95}Rb and ^{97}Rb. *Zeitschrift für Physik A Atoms and Nuclei*, 312(1-2):43–57, 1983. ISSN 0939-7922.

[77] E. Browne and J.K. Tuli. Nuclear Data Sheets for A = 99. *Nuclear Data Sheets*, 112(2):275 – 446, 2011. ISSN 0090-3752.

[78] R.A. Meyer *et al.* Deformation in odd-mass nuclei near A $\sim$ 100: one- and three-quasiparticle nilsson states in 99Y. *Nuclear Physics A*, 439(3):510 – 534, 1985. ISSN 0375-9474.

[79] Balraj Singh. Nuclear Data Sheets for A = 100 . *Nuclear Data Sheets*, 109(2): 297 – 516, 2008. ISSN 0090-3752.

[80] P. Paradis, G. Lamoureux, R. Lecomte, and S. Monaro. Measurement of the static quadrupole moments of the first 2^+ states in ^{94}Mo, ^{96}Mo, ^{98}Mo, and ^{100}Mo. *Phys. Rev. C*, 14:835–841, Sep 1976.

[81] G. Lhersonneau, H. Gabelmann, N. Kaffrell, K.-L. Kratz, and B. Pfeiffer. Lifetime measurements in 99Sr and 100Zr. *Zeitschrift für Physik A Atomic Nuclei*, 332(2):243–244, 1989. ISSN 0939-7922.

[82] G. Fioni *et al.* Reduction of energy dispersion on a parabola mass spectrometer. *Nucl. Inst. and Meth. in Phys. Res. A*, 332(1-2):175 – 180, 1993.

[83] Balraj Singh. Nuclear Data Sheets for A = 79 . *Nuclear Data Sheets* , 96(1):1 – 176, 2002.

[84] E. Browne. Nuclear Data Sheets update for A = 83 . *Nuclear Data Sheets* , 66 (2):281 – 346, 1992.

[85] H. Sievers. Nuclear data sheets update for A = 85 . *Nuclear Data Sheets* , 62(0): 271 – 325, 1991.

[86] I. Hossain *et al.* Lifetime measurement of the πg9/2 isomer in ^{79}As. *Phys. Rev. C*, 58:1318, 1998.

[87] R. Grzywacz *et al.* *Phys. Rev. Lett.*, 81:766–769, 1998.

[88] T. Ishii *et al.* *NIM A*, 395:210 – 216, 1997.

[89] G. Winter *et al.* *Z. Phys. A*, 332:33–43, 1989.

[90] J. W. Gruter, K. Sistemich, P. Armbruster, J. Eidens, and H. Lawin. *Physics Letters B*, 33(7):474, 1970.

[91] R. Sellam. *Thesis, Univ. Grenoble*, 1976.

[92] J. A. Pinston *et al.* *Phys. Rev. C*, 71:064327, 2005.

[93] J. K. Hwang *et al.* *Phys. Rev. C*, 67:054304, May 2003.

[94] C. M. Folden *et al.* *Phys. Rev. C*, 79:064318, 2009.

[95] J. W. Gruter. *JUL-879-NP*, 1972.

[96] A. E. Zobov *et al.* Decay Scheme of the Nucleus ^{85}Kr. In *Program and Theses*, 1986.

[97] J. J. Ressler *et al.* Fission fragment isomers populated via ^{6}Li $+^{232}$ Th. *Phys. Rev. C*, 81:014301, 2010.

[98] J. K. Hwang *et al.* *Phys. Rev. C*, 73:044316, 2006.

[99] E. Monnand *et al.* *CEA-N-2176,P20*, 1980.

[100] O.T. Grudzevich. Emission properties of fission fragments and their isomeric ratios. *Physics of Atomic Nuclei*, 64(9):1564–1580, 2001. ISSN 1063-7788.

[101] R. W. Mills. Neutron-induced fission product yields. *JEFF-31*, 2005.

[102] D. Kameda *et al.* Observation of new microsecond isomers among fission products from in-flight fission of 345 MeV/nucleon ^{238}U. *Phys. Rev. C*, 86:054319, Nov 2012.

[103] C. Thibault *et al.* Hyperfine structure and isotope shift of the D_2 line of $^{76-98}$Rb and some of their isomers. *Phys. Rev. C*, 23:2720, 1981.

[104] G. Georgiev. *private communication.*

[105] F. Buchinger *et al.* Systematics of nuclear ground state properties in $^{78\check{}100}$Sr by laser spectroscopy. *Phys. Rev. C*, 41:2883–2897, 1990.

[106] "W. Urban and others". Medium-spin structure of 96,97Sr and 98,99Zr nuclei and the onset of deformation in the A-100 region. *"Nuclear Physics A "*, 689 (3-4):605 – 630, 2001.

[107] C. Y. Wu, H. Hua, D. Cline, A. B. Hayes, R. Teng, R. M. Clark, P. Fallon, A. Goergen, A. O. Macchiavelli, and K. Vetter. Multifaceted yrast structure and the onset of deformation in ^{96,97}Sr and ^{98,99}Zr. *Phys. Rev. C*, 70:064312, Dec 2004.

[108] W.Urban *et al.* First observation of the $\nu 9/2[404]$ orbital in the A - 100 mass region. *Eur.Phys.J. A*, 16:11, 2003.

[109] H. Mach and other. Deformation and shape coexistence of 0+ states in 98Sr and 100Zr. *Physics Letters B*, 230(1–2):21 – 26, 1989.

[110] *User's manual for the computer code odda.*

[111] M.A.C. Hotchkins *et al.* Rotational bands in the mass 100 region. *Nuclear Physics A*, 530(1):111 – 134, 1991.

[112] B. Cheal *et al.* The shape transition in the neutron-rich yttrium isotopes and isomers. *Physics Letters B*, 645(2-3):133 – 137, 2007.

[113] H. Mach, F. K. Wohn, M. Moszyn'ski, R. L. Gill, and R. F. Casten. Subnanosecond lifetime measurements in Y and Sr nuclei and the saturation of deformation near A =100. *Phys. Rev. C*, 41:1141–1146, 1990.

[114] Tord Bengtsson and Ingemar Ragnarsson. Rotational bands and particle-hole excitations at very high spin. *Nuclear Physics A*, 436(1):14 – 82, 1985.

[115] Y.X. Luo, J.O. Rasmussen, J.H. Hamilton, *et al.* The first observation of a deformed ground-state band in 100Nb and the high-spin level scheme of its 4n fission partner 148La. *Nuclear Physics A*, 825(1-2):1–15, 2009.

List of Publications

- M. Rudigier, G. S. Simpson, J. M. Daugas, A. Blazhev, C. Fransen, G. Gey, M. Hackstein, J. Jolie, U. Köster, T. Malkiewicz, T. Materna, M. Pfeiffer, M. Ramdhane, J.-M. Régis, W. Rother, T. Thomas, N. Warr, D. Wilmsen, J. Le Bloas, and N. Pillet, *Delayed* γ*-ray and conversion-electron spectroscopy of* $A = 97$ *fission fragments*, Phys. Rev. C; 87, 064317 (2013)

- M.Rudigier, J.-M.Regis, J.Jolie, K.O.Zell, C.Fransen, *Lifetime of the first excited 2+ state in 172W and 178W*, Nucl.Phys. A847, 89 (2010)

- J.-M. Régis, H. Mach, G.S. Simpson, J. Jolie, G. Pascovici, N. Saed-Samii, N. Warr, A. Bruce, J. Degenkolb, L.M. Fraile, C. Fransen, D.G. Ghita, S. Kisyov, U. Koester, A. Korgul, S. Lalkovski, N. Mărginean, P. Mutti, B. Olaizola, Z. Podolyak, P.H. Regan, O.J. Roberts, M. Rudigier, L. Stroe, W. Urban, D. Wilmsen, *The generalized centroid difference method for picosecond sensitive determination of lifetimes of nuclear excited states using large fast-timing arrays*, Nucl.Instrum.Methods Phys.Res. A 726, 191 (2013)

- M. Albers, K. Nomura, N. Warr, A. Blazhev, J. Jolie, D. Mücher, B. Bastin, C. Bauer, C. Bernards, L. Bettermann, V. Bildstein, J. Butterworth, M. Cappellazzo, J. Cederkall, D. Cline, I. Darby, S. Das Gupta, J.M. Daugas, T. Davinson, H. De Witte, J. Diriken, D. Filipescu, E. Fiori, C. Fransen, L.P. Gaffney, G. Georgiev, R. Gernhauser, M. Hackstein, S. Heinze, H. Hess, M. Huyse, D. Jenkins, J. Konki, M. Kowalczyk, T. Kroll, R. Krücken, J. Litzinger, R. Lutter, N. Marginean, C. Mihai, K. Moschner, P. Napiorkowski, B.S. Nara Singh, K. Nowak, J. Pakarinen, M. Pfeiffer, D. Radeck, P. Reiter, S. Rigby, L.M. Robledo, R. Rodriguez-Guzman, M. Rudigier, M. Scheck, M. Seidlitz, B. Siebeck, G.S. Simpson, P. Thöle, T. Thomas, J. Van de Walle, P. Van Duppen, M. Vermeulen, D. Voulot, R. Wadsworth, F. Wenander, K. Wimmer, K.O. Zell, M. Zielinska, *Shape dynamics in neutron-rich Kr isotopes: Coulomb excitation of 92Kr, 94Kr and 96Kr*, Nucl. Phys. A899, 1 (2013)

- L.P. Gaffney, P.A. Butler, M. Scheck, A.B. Hayes, F. Wenander, M. Albers, B. Bastin, C. Bauer, A. Blazhev, S. Bonig, N. Bree, J. Cederkall, T. Chupp, D. Cline, T.E. Cocolios, T. Davinson, H. De Witte, J. Diriken, T. Grahn, A. Herzan, M. Huyse, D.G. Jenkins, D.T. Joss, N. Kesteloot, J. Konki, M. Kowalczyk, Th. Kroll, E. Kwan, R. Lutter, K. Moschner, P. Napiorkowski, J. Pakarinen, M. Pfeiffer, D. Radeck, P. Reiter, K. Reynders, S.V. Rigby, L.M. Robledo, M. Rudigier, S. Sambi, M. Seidlitz, B. Siebeck, T. Stora, P. Thoele, P. Van Duppen, M.J. Vermeulen, M. von Schmid, D. Voulot, N. Warr, K. Wimmer, K. Wrzosek-Lipska, C.Y. Wu, M. Zielinska, *Studies of pear-shaped nuclei using accelerated radioactive beams*, Nature 497, 199 (2013)

- M. Albers, N. Warr, K. Nomura, A. Blazhev, J. Jolie, D. Mucher, B. Bastin, C. Bauer, C. Bernards, L. Bettermann, V. Bildstein, J. Butterworth, M. Cappellazzo, J. Cederkall, D. Cline, I. Darby, S. Das Gupta, J.M. Daugas, T. Davinson, H. De Witte, J. Diriken, D. Filipescu, E. Fiori, C. Fransen, L.P. Gaffney, G. Georgiev, R. Gernhauser, M. Hackstein, S. Heinze, H. Hess, M. Huyse, D. Jenkins, J. Konki, M. Kowalczyk, T. Kroll, R. Krucken, J. Litzinger, R. Lutter, N. Marginean, C. Mihai, K. Moschner, P. Napiorkowski, B.S. Nara Singh, K. Nowak, T. Otsuka, J. Pakarinen, M. Pfeiffer, D. Radeck, P. Reiter, S. Rigby, L.M. Robledo, R. Rodriguez-Guzman, M. Rudigier, P. Sarriguren, M. Scheck, M. Seidlitz, B. Siebeck, G. Simpson, P. Thole, T. Thomas, J. Van de Walle, P. Van Duppen, M. Vermeulen, D. Voulot, R. Wadsworth, F. Wenander, K. Wimmer, K.O. Zell, M. Zielinska, *Evidence for a Smooth Onset of Deformation in the Neutron-Rich Kr Isotopes*, Phys. Rev. Lett. 108, 062701 (2012)

- J.-M. Régis, M. Rudigier, J. Jolie, A. Blazhev, C. Fransen, G. Pascovici, N. Warr *The time-walk of analog constant fraction discriminators using very fast scintillator detectors with linear and non-linear energy response*, Nucl. Instrum. Methods Phys. Res. Section A 684, 36 (2012)

- S. Kisyov, S. Lalkovski, N. Marginean, D. Bucurescu, L. Atanasova, D.L. Balabanski, Gh. Cata-Danil, I. Cata-Danil, J.-M. Daugas, D. Deleanu, P. Detistov, D. Filipescu, G. Georgiev, D. Ghita, T. Glodariu, J. Jolie, D.S. Judson, R. Lozeva, R. Marginean, C. Mihai, A. Negret, S. Pascu, D. Radulov, J.-M. Regis, M. Rudigier, T. Sava, L. Stroe, G. Suliman, N.V. Zamfir, K.O. Zell, M. Zhekova, *In-beam fast-timing measurements in 103, 105, 107Cd*, Phys. Rev. C 84, 014324 (2011)

- J.-M. Régis, G. Pascovici, J. Jolie, M. Rudigier, *The mirror symmetric centroid difference method for picosecond lifetime measurements via* γ*–*γ *coincidences using very fast LaBr3(Ce) scintillator detectors*, Nucl. Instrum. Methods Phys. Res. A 622, 83 (2010)

- J.-M. Regis, Th. Materna, S. Christen, C. Bernards, N. Braun, G. Breuer, Ch. Fransen, S. Heinze, J. Jolie, T. Meersschaut, G. Pascovici, M. Rudigier, L. Steinert, S. Thiel, N. Warr, K.O. Zell, *Sub-nanosecond lifetime measurements using the Double Orange Spectrometer at the cologne 10 MV Tandem accelerator*, Nucl. Instrum. Methods Phys. Res. A 606, 466 (2009)

Conference Proceedings

- E. Williams, N. Cooper, M. Bonett-Matiz, V. Werner, J.-M. Régis, M. Rudigier, T. Ahn, V. Anagnostatou, Z. Berant, M. Bunce, M. Elvers, A. Heinz, G. Ilie,

J. Jolie, D. Radeck, D. Savran and M. Smith, *High-precision excited state lifetime measurements in rare earth nuclei using LaBr3(Ce) detectors*, EPJ Web of Conferences, Vol. 35, 06006 (2012)

- V. Werner, N. Cooper, M. Bonett-Matiz, E. Williams, J.-M. Regis, M. Rudigier, T. Ahn, V. Anagnostatou, Z. Berant, M. Bunce, M. Elvers, A. Heinz, G. Ilie, J. Jolie, D. Radeck, D. Savran, M. Smith, *Excited State Lifetime Measurements in Rare Earth Nuclei with Fast Electronics*, J.Phys.:Conf.Ser. 312, 092062 (2011)

Acknowledgements / Danksagung

Ich möchte allen meinen Dank aussprechen die mich während der Entstehung dieser Arbeit begleitet haben.

Besonders danke ich Prof. Dr. Jan Jolie für die Vergabe des Themas dieser Arbeit, die Unterstützung und Betreuung, und nicht zuletzt für die Ermöglichung der interessanten und erfahrungsreichen Zeit am Institut für Kernphysik.

Mein besonderer Dank gilt auch den anderen Mitgliedern der Prüfungskommission, Prof. Dr. Peter Reiter, Prof. Dr. Andreas Schadschneider und Dr. Stefan Heinze, für ihre Zeit.

I sincerely thank Dr. Gary Simpson for collaboration during the experiments and many valuable discussions. His enthusiasm, not only for nuclear physics, is truly inspiring.

Ein besonderer Dank geht an Dr. Jean-Marc Régis. Seit meiner Diplomarbeit hat die Zusammenarbeit mit ihm einen prägenden Einfluss auf mich. Ich danke ihm für die Erfahrungen mit dem Orange Spektrometer und für die schöne Zeit in der - zu Anfang sehr kleinen - fast-timing Gruppe am IKP in Köln. Ich danke ihm vor allem auch für die Kollaboration bei den Experimenten am Lohengrin und das sorgfältige Korrekturlesen eines Teils dieser Arbeit.

I want to thank Pavel Petkov for helpful discussions concerning the quasiparticle rotor model.

Ich danke Dr. Ulli Köster, und auch Dr. Herbert Faust und Dr. Waldemar Urban, für die fruchtbare Zusammenarbeit bei den Experimenten am Lohengrin und einige wertvolle Diskussionen während meiner Zeit in Grenoble.

Ich möchte besonders Dr. Désirée Radeck danken, für das sorgfältige Korrekturlesen dieser Arbeit, viele Diskussionen und vor allem die großartige Unterstützung und Motivation bis zur letzten Minute.

Vielen Dank an alle Mitglieder des Instituts für Kernphysik der Universität zu Köln, für die schöne und prägende Zeit. Ich danke Dr. Nigel Warr und Dr. Andrey Blazhev für viele erhellende Diskussionen und dafür, dass ihre Bürotür immer offenstand. Ich danke Tim Thomas für das Korrekturlesen

eines Teils dieser Arbeit, für viele Diskussionen über Kernphysik, Kernmodelle im Allgemeinen und die Programme *odda* und *phint* im Besonderen. In diesem Zusammenhang möchte ich auch Dr. Stefan Heinze danken. Ich danke Kevin Moschner für das Korrekturlesen dieser Arbeit, fruchtbare Diskussionen über ihren Gegenstand und viele ermutigende Worte. Ich danke Dr. Michael Pfeiffer, Guillaume Gey, Dennis Wilmsen und Nima Saed-Samii für die Kooperation bei den Experimenten am Lohengrin. Letzterem danke ich besonders für die Stunden die wir mit dem xia_sort Code verbracht haben - sie waren sehr Lehrreich für mich. Ich danke Hanna Duckwitz, Moritz Dannhoff, Matthias Dewald, Pierre Thoele, Julia Litzinger, Claus Müller-Gattermann und allen anderen Mitgliedern des IKP, auch den ehemaligen die ich kennenlernen durfte, für viele schöne Stunden, nicht nur während der Arbeitszeit.

Ich danke meinen guten Freunden Peter Beule, Karen Bresser und Gerrit Wilken dafür, dass sie während der Zeit meiner Doktorarbeit immer für mich da waren.

Ich danke meinen Eltern Helga und Lothar für die uneingeschränkte Unterstützung und dafür, dass sie mir das Gefühl geben im Schwarzwald immer einen Ort zu haben an den ich zurückkehren kann. Ich danke meinen Schwestern Nicole und Vanessa sowieso für alles.

Erklärung

Ich versichere, dass ich die von mir vorgelegte Dissertation selbständig angefertigt, die benutzten Quellen und Hilfsmittel vollständig angegeben und die Stellen der Arbeit - einschließlich Tabellen, Karten und Abbildungen -, die anderen Werken im Wortlaut oder dem Sinn nach entnommen sind, in jedem Einzelfall als Entlehnung kenntlich gemacht habe; dass diese Dissertation noch keiner anderen Fakultät oder Universität zur Prüfung vorgelegen hat; dass sie - abgesehen von unten angegebenen Teilpublikationen - noch nicht veröffentlicht worden ist sowie, dass ich eine solche Veröffentlichung vor Abschluss des Promotionsverfahrens nicht vornehmen werde. Die Bestimmungen der Promotionsordnung sind mir bekannt. Die von mir vorgelegte Dissertation ist von Prof. Dr. Jan Jolie betreut worden.

Matthias Rudigier

Teilpublikationen

Teile der Kapitel 3 und 5 wurden veröffentlicht in:

M. Rudigier, G. S. Simpson, J. M. Daugas, A. Blazhev, C. Fransen, G. Gey, M. Hackstein, J. Jolie, U. Köster, T. Malkiewicz, T. Materna, M. Pfeiffer, M. Ramdhane, J.-M. Régis, W. Rother, T. Thomas, N. Warr, D. Wilmsen, J. Le Bloas, and N. Pillet, *Delayed* γ*-ray and conversion-electron spectroscopy of* $A = 97$ *fission fragments*, Physics Review C; 87, 064317 (2013)